

DEVELOPMENT OF A PROTON INDUCED X-RAY EMISSION (PIXE)
MATERIAL ANALYSIS SYSTEM

By

James William Eisenmann III

November 2018

Director of Thesis: Jefferson L. Shinpaugh, PhD

Major Department: Physics

A material analysis system using particle-induced x-ray emission (PIXE) analysis has been developed to measure trace element composition in a wide range of samples. The system was constructed in the particle accelerator laboratory in the Department of Physics at East Carolina University, and includes a new high-vacuum beamline on the 2-million-volt tandem Pelletron ion accelerator, which includes a modified multi-sample target chamber.

PIXE analysis can provide sensitivities to the parts-per-million level or better for many elements. In this method, a sample is irradiated with protons in the energy range of 1 – 3 MeV from the particle accelerator. Characteristic x-rays emitted from the sample are detected with an x-ray spectrometer, and the emission spectrum is fit using

known spectral line energies to determine elemental composition of the sample.

Capabilities of the new PIXE analysis system, including a new state-of-the-art x-ray spectrometer and multi-sample target system, will be presented, and proposed multidisciplinary applications, such as in geology, will be discussed.

LIST OF FIGURES

1. Energy Level Diagram and X-Ray Emission Nomenclature.....	11
2. XRF K shell vacancy.....	12
3. XRF K_{α} transition.....	13
4. XRF L_{α} transition.....	14
5. XRF L_{γ} transition.....	15
6. Auger emission.....	16
7. FWHM noise vs. peaking time of SDD.....	31
8. General illustration of PIXE analysis.....	33
9. Diagram of cesium sputter source.....	39
10. Proton energy attenuation in air and vacuum.....	48
11. Motor and optical interrupter switch control.....	54
12. LEMO connector to electrical feedthrough diagram.....	55
13. LabView motor control interface.....	56
14. View from PIXE CCD camera.....	58
15. SDD detector.....	63
16. Operation and construction of the XR-100 Fast SDD.....	65
17. SDD detector core.....	65
18. FWHM vs. count rate frequency.....	66
19. $Fe - 55$ FWHM resolution vs. peaking time and temperature.....	68
20. Model of detector efficiency.....	71
21. Efficiency vs. energy for Fast SDD.....	72
22. Block Diagram: Detector, Preamp, Digital pulse processor.....	74
23. Fast SDD dimensions.....	86
24. XR-100 Fast SDD.....	86
25. $Fe - 55$, $Cs - 137$ calibration data.....	95
26. Gain vs. full scale energy range.....	97
27. Energy scale, Gain:5.....	98
28. Energy scale, Gain:10.....	98
29. Energy scale, Gain:15.....	99
30. Energy scale, Gain:20.....	99
31. Energy scale, Gain:25.....	100
32. Energy scale, Gain:30.....	100
33. Energy scale, Gain:35.....	101
34. Energy scale, Gain:45.....	101
35. Electronic noise vs. peaking time.....	103
36. $Fe - 55$ spectra @ $1 \mu A$	104
37. $Fe - 55$ spectra @ $4 \mu A$	104
38. $Fe - 55$ spectra @ $11.2 \mu A$	105
39. $Fe - 55$ spectra @ $25.6 \mu A$	105
40. Count rate vs. dead time.....	106
41. Au spectra @ $2 MeV$, $2.5 nA$	107
42. Au spectra @ $3 MeV$, $1 nA$	107
43. GaP spectra @ $3 MeV$, $1 nA$	109
44. GaP spectra @ $3 MeV$, $1 nA$ (linear scale).....	109

45. Superconductor material spectra, 2 <i>MeV</i> , 2.1 <i>nA</i>	110
46. Superconductor material spectra, 2 <i>MeV</i> , 2.1 <i>nA</i> (linear scale).....	110
47. Superconductor material spectra, 3 <i>MeV</i> , 1 <i>nA</i>	111
48. <i>FeO₃</i> on <i>Al</i> Mylar, 2 <i>MeV</i> , 2.6 <i>nA</i>	112
49. <i>FeO₃</i> on <i>Al</i> Mylar, 2 <i>MeV</i> , 12 <i>nA</i>	112

LIST OF TABLES

1. K shell fluorescent yields (Z= 6-92)	20
2. L shell fluorescent yields (experimental).....	21
3. K shell ionization cross sections.....	23
4. L shell ionization cross sections.....	24
5. Gamma ray yields for select targets.....	28
6. Gain adjustment parameters.....	89
7. Gain eV/Channel.....	102

DEVELOPMENT OF A PROTON INDUCED X-RAY EMISSION (PIXE)
MATERIAL ANALYSIS SYSTEM

A Thesis

Presented to the Faculty of the Department of Physics

East Carolina University

In Partial Fulfillment of the Requirements for the Degree

Master of Science in Applied Physics

By

James William Eisenmann III

November 2018

TABLE OF CONTENTS

LIST OF TABLES.....	<i>iii</i>
LIST OF FIGURES.....	<i>v</i>
1. Introduction.....	2
1.1 XRF and an Introduction to PIXE.....	2
1.2 History.....	4
1.3 PIXE.....	8
1.3.1 Quantum Numbers.....	8
1.3.2 Transitions.....	10
1.3.3 Detection Limits.....	18
1.3.4 Fluorescent Yields.....	18
1.3.5 Ionization Cross Sections.....	23
1.3.6 Spectral Background.....	26
1.3.7 Mechanical, Electrical, and Thermal Noise.....	30
1.3.8 Sample Composition and Attenuation.....	33
2. Experimental Methods.....	38
2.1 Proton Beam Creation.....	38
2.1.1 Cesium Sputter Source.....	38
2.1.2 Pelletron Tandem Particle Accelerator.....	43
2.1.3 PIXE Beam Requirements.....	50
2.2 Target Chamber.....	51

2.2.1 Chamber Specifications.....	49
2.2.2 Chamber Monitoring.....	57
2.2.3 Collimators.....	59
2.2.4 Detector Positioning.....	60
2.3 XR-100 Fast Silicon Drift Diode Detector.....	60
2.3.6 SDD Detector Theory and Operation.....	60
2.3.1 Temperature Control.....	64
2.3.2 Resolution.....	64
2.3.3 Efficiency.....	66
2.3.4 Multi-Layer Collimator.....	71
2.3.5 PX5 Digital Pulse Processor.....	71
2.3.5.1 Energy Calibration.....	73
2.3.5.2 Pulse Shaping.....	79
2.3.5.3 PX5 Electronics.....	81
2.3.7 Detector Specifications and Construction.....	85
2.3.8 Data Display and Analysis.....	88
2.3.9 Electrical and Software Interfaces.....	89

2.3.10 System Gain.....	89
2.3.11 Standard Operating Procedure.....	90
3.3.11.1 Energy/Channel Calibration.....	93
3. Results/Discussion.....	94
3.1 Target Chamber Results.....	94
3.2 Fe-55 Spectral Data.....	95
3.3 PIXE Spectral Data.....	107
4. Conclusion.....	114

1. Introduction

1.1 XRF and an Introduction to PIXE

X-ray fluorescence, or XRF, is a common analytical technique used to assess the elemental makeup of matter. High energy electron beams, x-rays, alpha particles, and protons can all be used to induce XRF. XRF is a preferred method for analysis because of its expeditious and non-destructive nature in determining the origin, dating, purity, or authenticity of a given sample. Many disciplines such as archaeology, metallurgy, chemistry, biology, geology, and even art conservation have an interest in using XRF for analysis.

Particle, or proton, induced x-ray emission (PIXE) is an XRF process that occurs when a material is exposed to a 1-3 MeV ion beam. The procedure begins when an accelerator sends charged particles, typically protons, into an evacuated analysis chamber containing the material impending evaluation. Electrons found in the innermost shells of the target atoms are expelled and vacancies are created, but outer shell electrons “jump in” to replace these vacancies. Consequently, electromagnetic radiation is emitted that possesses frequencies found in the x-ray region of the EM spectrum; this radiation is unique to certain elements found in the material. The x-rays are analyzed through a detection system, usually a Si(Li) detector, then the pulses from the detector are interpreted. As there are numerous and overlapping data peaks, many are indistinguishable from one another, the presence of certain elements in the sample are specified and quantified by means of computer software used to deconvolute the data.

There are several procedures that involve the use of ion beam for the examination of individual chemical elements that make up a given substance. All these

techniques rely on the same two fundamentals. High energy charged particles bombard a material, and they subsequently lose energy at precise and recognizable rates while passing through the sample. As ions traverse a material there is a probability for nuclear interaction. The results of these atomic collisions include the emission of different forms of energy that are dependent on the probability of interaction specific to the individual characteristics of the targeted atom, or cross section. These energy emissions can be released by means of charged particles or as a quantum of distinct electromagnetic radiation – each emission can be used to identify the chemical makeup of a given study sample.

PIXE, or Particle-Induced X-Ray Emission spectroscopy, is a highly practical method used in the determination of the chemical composition of a substance. PIXE is achievable when charged particles are given energy with a particle accelerator, the ions are focused, collimated, and then forced to irradiate a specimen. As the target material is bombarded, the protons, or other heavy ions, interact with target atoms in a series of inelastic collisions and Coulomb interactions. According to the specific energy loss, or stopping power of the target material, an incoming ion will encounter a steady decrease in velocity as its energy is transferred to the target. With a probability dictated by the interaction cross-section, some of these ionized atoms will emit characteristic x-rays upon their return to ground state. With the help of a suitable x-ray spectrometer, analysis of photons generated by the de-excitation of ionized atoms is performed, and accurate elemental identification is accomplished.

1.2 History

James Chadwick proved in 1912 that electrons and alpha particles produced from a radioactive source could induce x-ray emission. The x-ray intensity generated from alpha particle collisions was so low, however, that the specifics of the emission spectra could not be distinguished; therefore, it could not yet be used for purposes of material analysis [1].

In 1914, using a demountable x-ray tube and flat crystal spectrometer, Henry Mosely laid the groundwork for PIXE when he bombarded a variety of elements and observed the emission of distinctive x-ray frequencies [2]. He also found that there was a mathematical relationship between the wavelengths of x-rays and the atomic numbers of the metals that emitted the photons.

During 1922, Hadding, a Swedish geologist with the University of Lund, detected 10-12 differing elements through an x-ray spectral analysis of an assortment of minerals [3]. When a positive reconciliation between x-ray emission data and a chemical analysis of these minerals occurred, the scientific community quickly saw that x-ray spectroscopy would allow for effective multielemental analysis.

In 1950, Raimond Castaing, at the University of Paris, made a breakthrough in x-ray emission spectrometry when he demonstrated that a specimen being analyzed with an electron microscope emitted x-rays that could be appropriated for multielemental analysis [4]. Castaing used mostly metallurgical samples that were positioned to study spatial composition, he used an electron beam that had a 1 μ m diameter, and a focusing crystal spectrometer with a Geiger counter for detection. This method evolved when a

scanning electron microscope was outfitted with an x-ray spectrometer. The brightness of a CRT was modulated by incoming x-rays as a function of energy, and the intensity of the created image gave a visual indication of the distribution of a given element as the electron probe scanned the sample [5].

Nuclear physics research greatly expanded during the 1950s, and, therefore, the use of particle accelerators increased as well. X-rays were prevalent as background in many nuclear and atomic physics experiments, so it was logical for physicists to gravitate toward theoretical and experimental research surrounding this phenomenon. With theoretical knowledge that bremsstrahlung radiation is produced in greater amounts with electrons in lieu of protons, and with information concerning cross sections regarding x-ray production as a function of particle energy and atomic number, the prospect of utilizing heavy charged particles for analysis started to become of interest [PIXE book]. With respect to MeV protons and 10 keV electrons, the cross section for x-ray production is roughly the same. This means that bremsstrahlung background is the main determinant in the sensitivity of x-ray analysis. It is found experimentally that background induced by protons is negligible; rather, the main source of background is from the bremsstrahlung given off by the secondary electrons created by the proton beam. This fact caused physicists to be inclined to use protons as the preferred projectile in x-ray emission analysis.

In the early 1960s, at the Lawrence Radiation Laboratory in Livermore California, Khan, Potter, and Worley attempted to utilize proton induced x-ray emission as an elemental analysis technique. They used a proportional counter and a low energy proton beam that ranged 100 to 500 keV in efforts to measure the thickness of thin films

[6]. The resolution was inadequate in determining contiguous elements though, and reliable multi-elemental analysis could not be implemented. Khan did find that the peak to background ratio for Aluminum was 10,000/1 with protons whereas electrons were known to give a 1000/1 peak to background. In the late 1960s, Poole and Shaw verified this at the Harwell Atomic Energy Research Establishment, after they analyzed the x-rays emitted by pure metals and alloys with a crystal spectrometer induced by a proton-probe with a beam collimated to a diameter of 100 μm [7].

During this same period, Ge(Li) Lithium doped Germanium, and Si(Li) solid state surface barrier detectors were being developed. The Ge(Li) detector became the benchmark for gamma ray detection, while the Lithium Drifted Silicon detector was the standard for energy-dispersive x-ray detection. For 5.9 keV x-rays, the Si(Li) detector has an average energy resolution of ≈ 150 eV; this made distinguishing *K* x-rays from adjacent elements feasible. The Si(Li) detector design allowed for mounting the detector very close to the source of x-ray emission, thus permitting the detector to span a larger solid angle. The close positioning offered superior detection efficiency compared to that provided by a crystal spectrometer.

During 1970, at the Lund institute of Technology, Johansson et al. [8] equipped with a Si(Li) detector and a 2 MeV proton beam, demonstrated the groundbreaking analytical technique that allowed for the multi-elemental analysis of trace elements. This system of analysis became known as PIXE, or proton induced x-ray emission.

PIXE developed rapidly in many nuclear physics laboratories after Johansson showed its usefulness. During the 1970s there was great concern about environmental

problems, and the sensitivity of PIXE prompted many laboratories to study air pollution and the measurement of toxic elements in humans and their surroundings.

High energy nuclear physics was becoming of more interest at this time, and the small accelerators were being rendered obsolete. These machines were perfect for PIXE analysis though, so rather than disposing of them they were used in PIXE research applications. Electronics, detectors, and computers that could be used in conjunction with PIXE were already available in these nuclear physics labs – this made the transition to this particular analysis technique an obvious choice.

Today many organizations, such as the CSIRO lab in Australia and the Louvre Museum in France, have invested large sums of money in setting up dedicated PIXE laboratories committed to specialized applications. This is a testament to PIXE's ability to compete with differing analytical methods, and it will likely be a favored analysis technique far into the future.

1.3 PIXE

Particle induced x-ray emission occurs as fast ions enter a specimen. Target atoms undergo inelastic collisions with charged projectiles, then, relative to the stopping power and distinctive attenuation properties of the sample, characteristic x-rays are emitted.

1.3.1 Quantum Numbers

To realize the actions of an electron, the Schrödinger equation can be solved to calculate equations that reveal their position coordinates. The coordinate expressions are then used develop quantum numbers representative of the atom's electron shell.

These numbers consist of the principle quantum number n which is representative of the primary electron shell, l which characterizes the shape of the orbital and number of subshells, m_l is the magnetic quantum number, and it specifies the number of energy levels within a subshell thus showing the electron's position in space, and finally s the quantum number that tells us an electrons half spin orientation – up or down. The possibilities for quantum numbers are as follows:

$$n = 1,2,3,4 \dots \quad (1)$$

$$l = 0,1,2, \dots, (n - 1) \quad (2)$$

$$m_l = l, (-l + 1), (-l + 2), \dots, -2, -1, 0, 1, 2, \dots, (l - 1), (l - 2), +l \quad (3)$$

$$s = +1/2, -1/2 \quad (4)$$

The four quantum numbers completely describe the state of an electron orbiting an atom. The first shell of an atom ($n = 1$) is referred to as the K shell, and a maximum of two electrons can be found there. A maximum of eight electrons can be found in the L shell ($n = 2$), and the M shell, $n = 3$, can house a maximum of 18 electrons. The maximum number of electrons that can be found in a given atomic shell is given by:

$$\text{max}\#_{e^-} = 2n^2 \quad (5)$$

l , m_l , and s states take effect in atoms with electron shells higher than $n = 1$ as they have more than two permissible electron conditions.

To accurately describe the angular distribution and shape of an orbital, there are several values of the orbital angular momentum quantum number l , and they are all

dependent on the principle quantum number n . When $l = 0, 1, 2, 3, 4, 5, 6$ the states are conventionally referred to as $s, p, d, f, g, h,$ and i subshells respectively, each subshell has a distinguishing shape. The number of orbitals and their position inside a subshell is given by the magnetic quantum number m_l . This value is dependent on the angular momentum quantum number and can be a negative integer, a positive integer, or zero. Sub-states indicating the fine electron structure within an atom are designated by electron spin orientation. These are important to know because the electrons in an atom are subject to the Pauli exclusion principle. This principle forbids certain electron transitions within the atom; the same quantum numbers cannot exist for any two electrons within an atom.

1.3.2 Transitions

The principal physics of PIXE happens during the transition process. A proton with sufficient energy (typically MeV) and an inner shell electron found within a sample atom experience a Coulomb interaction. As a result, the inner shell electron is attracted to, and thus, pulled out of the atom by, the impinging proton. A vacancy is produced within the inner shell causing the atom to be in an excited and unstable state. Electrons from outer shells transition to the inner shells causing the atom to return to its ground state. As the atom becomes stable through the transition process, excess energy—the difference between the binding energy of the inner and outer shells—is released as an XRF quantum. The fluorescence yield, or the probability of emission of an x-ray quantum, for heavy elements is close to 100%, but just a few percent for light elements [9].

There is a certain nomenclature to these transitions. Energy levels of the electrons within an atom determine the x-ray spectra. To indicate the shells they came from, characteristic x-rays are given the designation of K , L , M , N , and so on. The transitions that end in the K shell are designated K x-rays, those going to the L shell are called L x-rays, etc. An additional classification is the subscript alpha, beta, or gamma (α , β , or γ). These indicate electron transitions originating from higher energy shells. For example, if an electron fills a K-shell vacancy, but it came from the L-shell, the transition is classified as K_α . An electron jump from the M-shell to the K-shell would be called a K_β transition, and a transition from the N-shell to the L-shell is denoted by L_γ . Again, the Pauli Exclusion Principle cannot be violated. There is a fine structure and electrons have half spin designations. These Doublets have approximately the same energy since the shells have multiple orbits of higher and lower binding electrons, and they appear as a single peak in the spectrum, so they are assigned further designations of α_1 , α_2 , or β_1 , β_2 indicating a transition from one of the orbits in a higher shell to the same lower shell. In a PIXE spectrum light and medium-heavy elements give only two specific peaks K_α and K_β , while in the L x-ray spectrum of heavy elements there are four predominant resolved peaks and four weaker peaks [PIXE]. Therefore, depending on the element undergoing a transition to ground state, an assortment of x-ray energies may emanate from a target while under proton bombardment. Therefore, a multitude of elements composing a sample can be identified as they all have differing, or characteristic, x-ray energies.

Once ionized, excited atoms have the probability of depositing energy directly into an outer shell electron instead of emitting a photon. The excited electron can

deexcite by returning to a state of lower binding energy by emitting an electron from a more loosely bound state; in turn, excess energy is carried off with the ejected electron. This nonradiative transition is known as the “Auger effect” – the ejected electrons are known as “Auger” electrons [11]. If an atom was originally excited when the proton carried away an inner shell electron, and the atom rid itself of excess energy through an Auger emission, the atom has lost a total of two electrons, and is now found in a doubly charged state. The doubly charged atom can return to its steady state by emitting a third Auger electron from the M shell, or by single- or double-electron transitions that emit weaker satellite lines. Auger emission tends to increase as elements become lower in atomic number, since the effect increases as the difference in corresponding energy states become smaller.

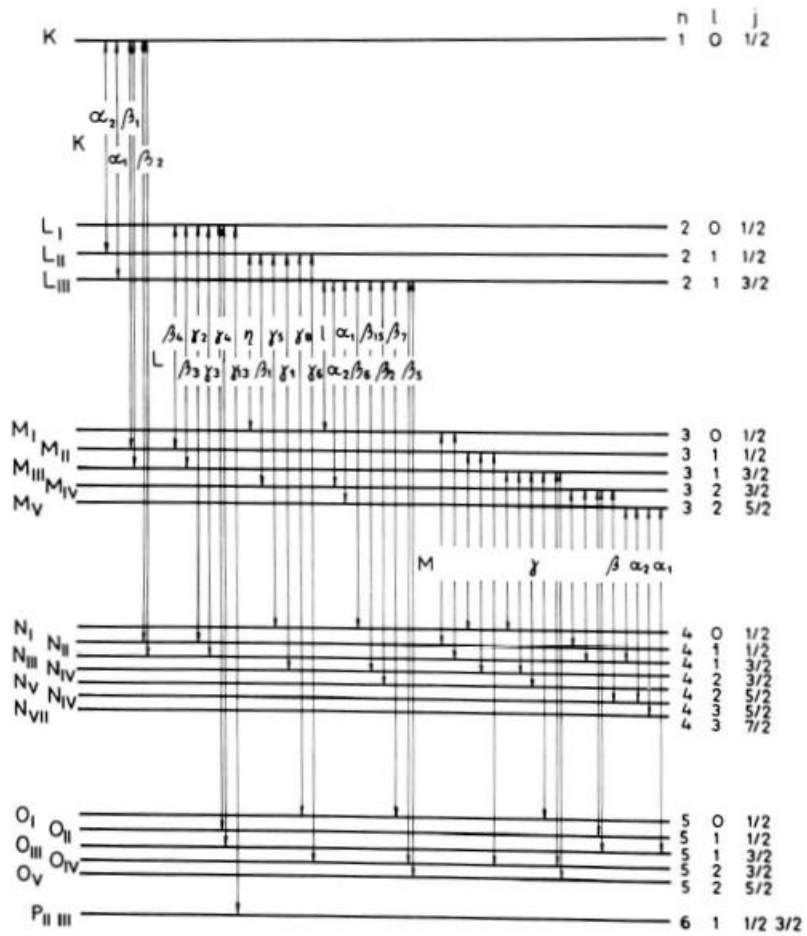
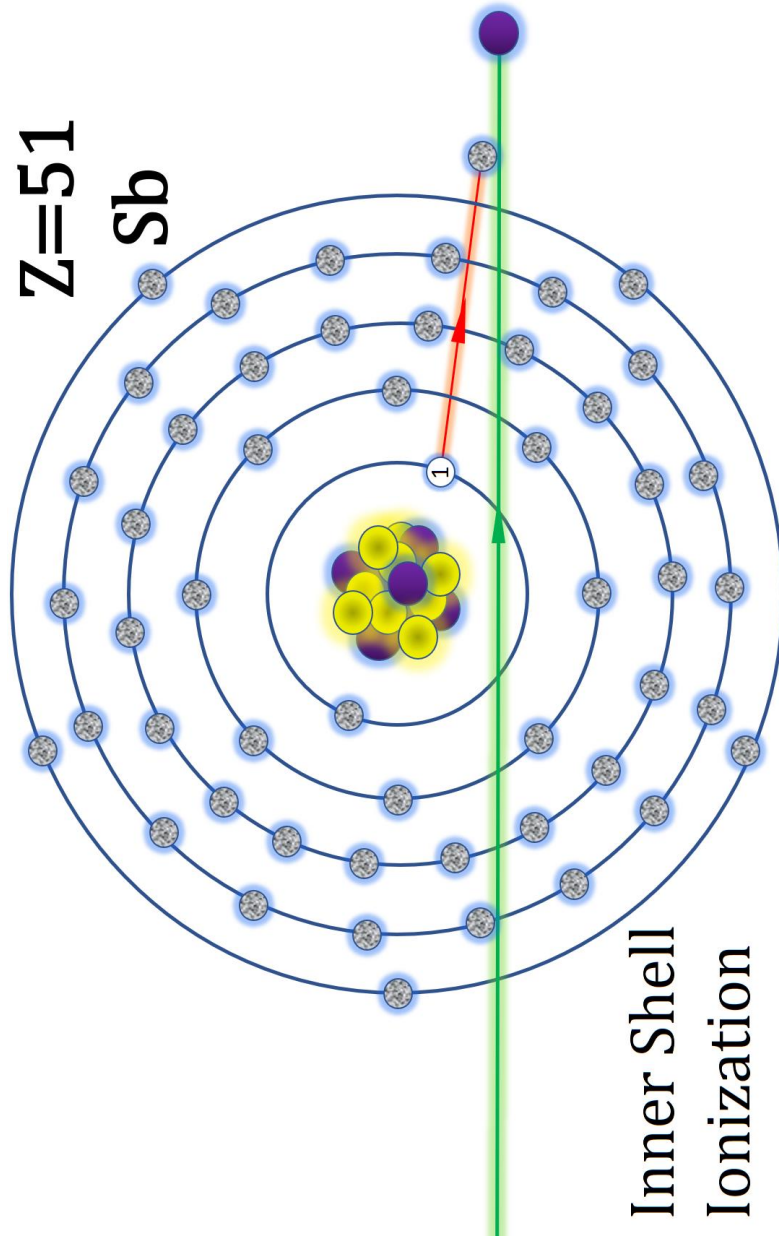


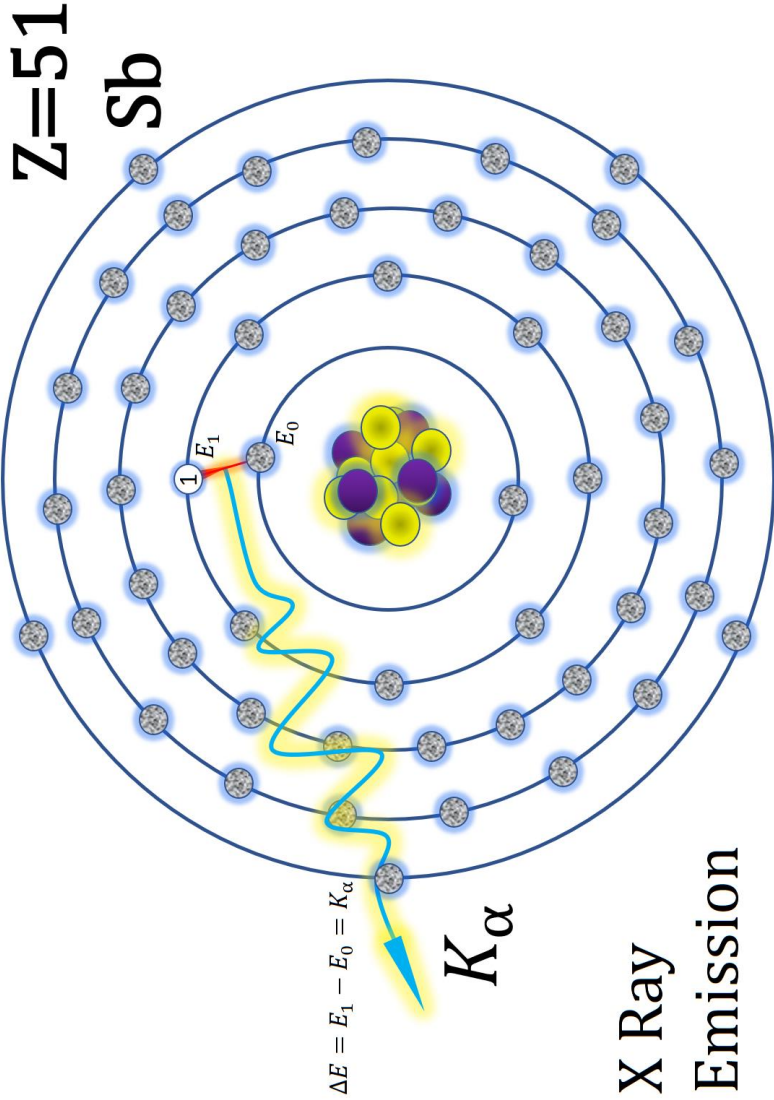
Figure (1). Nomenclature for x-ray lines and energy levels [10]

Figure (2) XRF



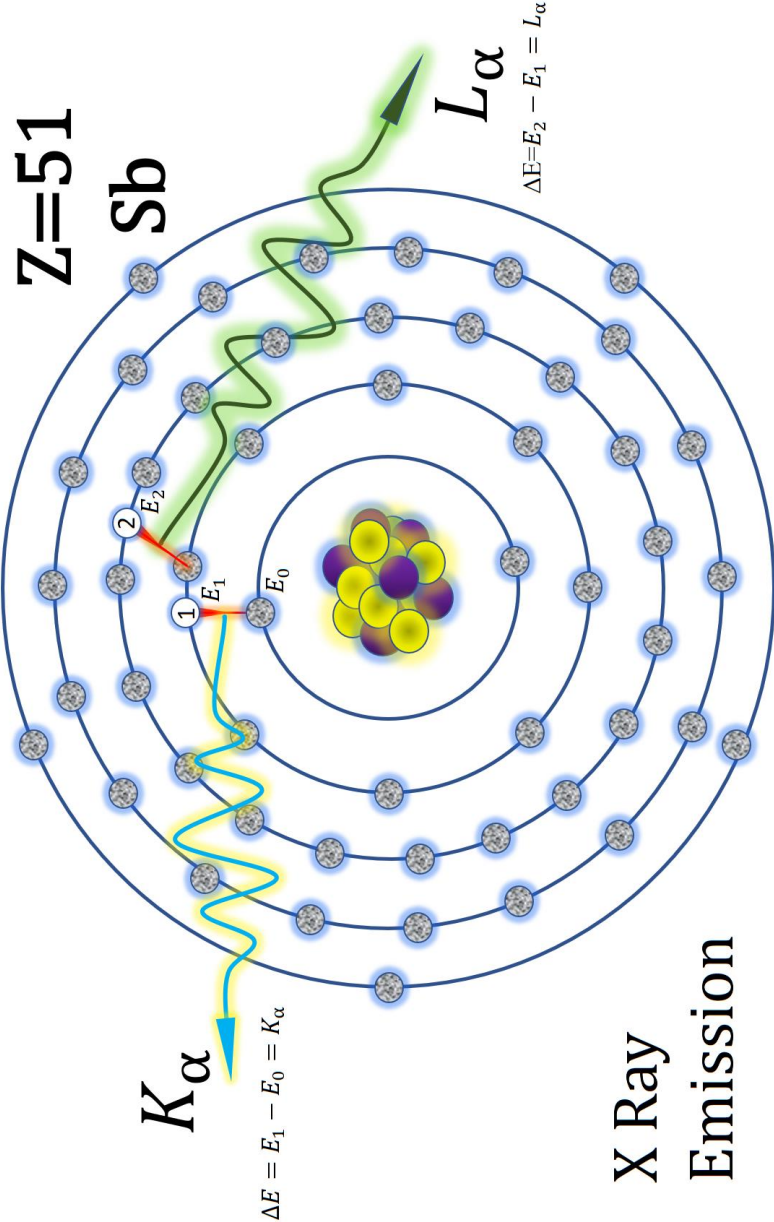
- 1) A K-shell electron is dislodged from an Antimony atom through Coulomb interaction with a proton, and a vacancy is created.

Figure (3) XRF



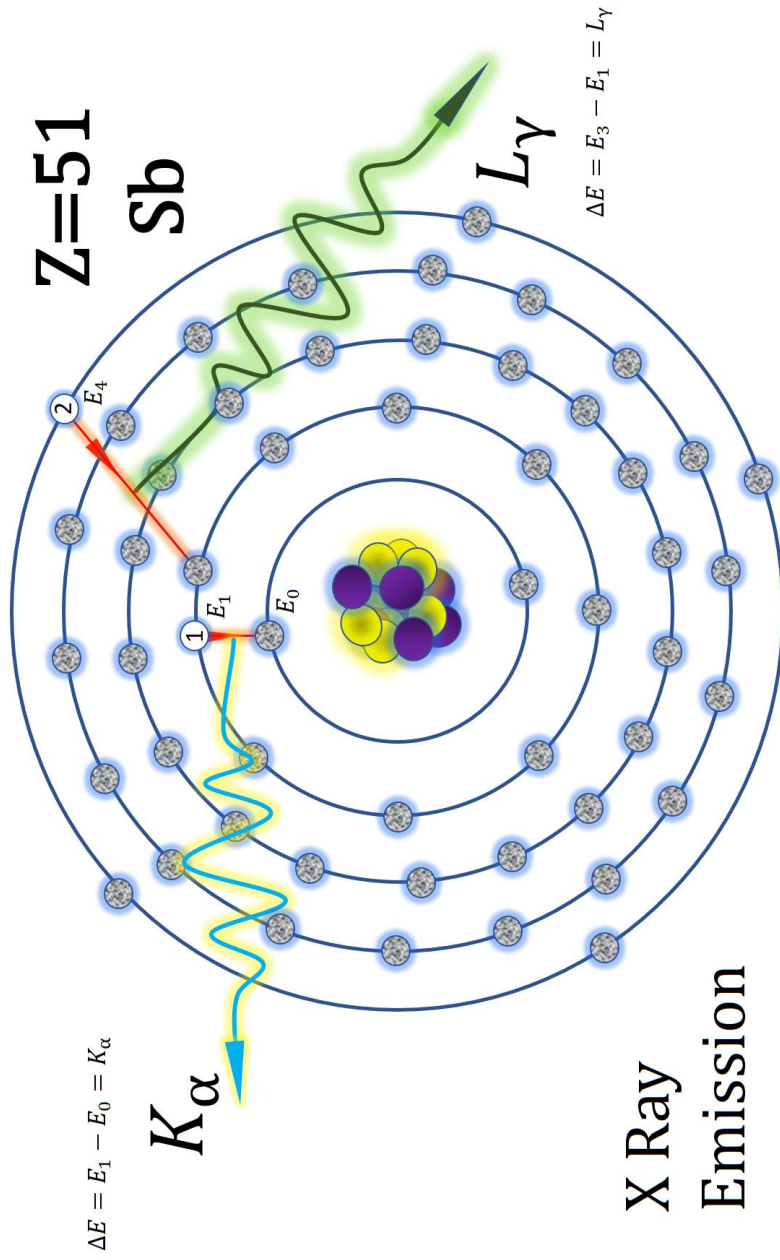
- 2) An L-shell electron transitions into the vacant K-shell, and it emits a characteristic $K\alpha$ x-ray unique to this element; a vacancy is created in the L-shell.

Figure (4) XRF



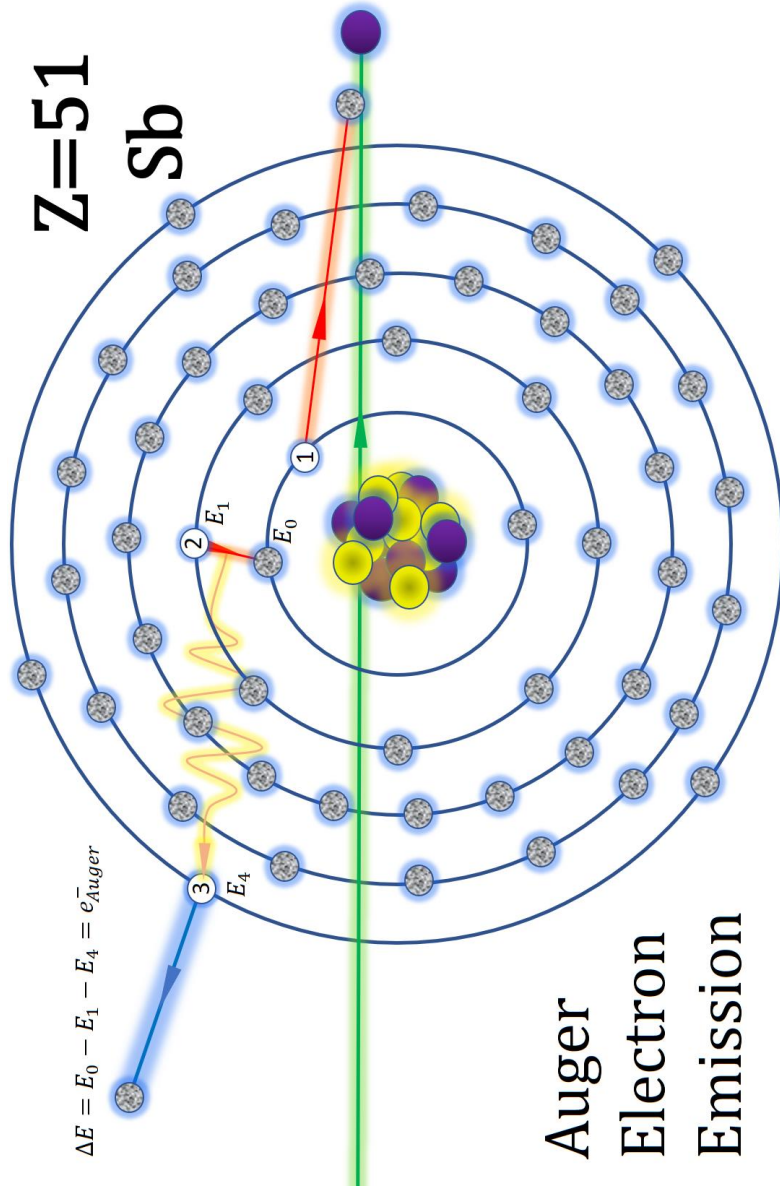
3) The vacancy created in the L-shell is filled by an M-shell electron inducing an $L\alpha$ x-ray

Figure (5) XRF



4) It is also probable that an N-shell electron transitions into the vacant L-shell of Antimony; a characteristic L_{γ} x-ray is produced.

Figure (6) Auger Emission



5) Energy from the atom's inner shell is transmitted to an outer shell electron causing its expulsion from the atom in the "Auger" electron emission process.

1.3.3 Detection Limits

Most detectors have a very thin Beryllium window, this dictates the lower detection limit for any XRF analysis system. Fluorine ($Z=9$) and below are not detectable, since x-rays emitted by these elements are attenuated by the beryllium detector window. The ionization cross section of an element is the determinant in the upper detection limit. The elements within the interval of $20 < Z < 50$ allow for successful detection of K x-rays with a SiLi detector (ECU's SDD detector has successfully shown $Z=11$ spectral data). Typically, K x-rays of lower Z elements are buried in the background spectra, but with the advent of superior detector technology, low Z element x-ray emission energies can be detected. L x-rays are detected as four distinct peaks in elements above $Z=50$. Heavy elements are detected by their L x-rays, and the medium-heavy to light elements can be identified by their characteristic K x-rays. Beam current, run time, and detector efficiency all influence effective x-ray detection. [12].

1.3.4 Fluorescence yields

As an electron is torn from the inner shell of an atom by fast proton interaction, it would be intuitive to assume that the XRF would equal the amount of inner shell vacancies being filled by stabilizing transitions. The probability of a vacant atomic shell or subshell receiving an electron transitioning from a higher energy shell and producing radiative emission is termed fluorescence yield, but it is not found to be unity. The Auger emission process competes with XRF when it facilitates energy being carried off as electrons are ejected from their outer shells. This lowers the probability of a photon

emission by the same probability of an Auger emission. The expression for ω_K , the fluorescence yield of the K shell, is

$$\omega_K = \frac{I_K}{n_K} \quad (6)$$

Where the total number of K x-rays emitted from a target are given by I_K , while n_K denotes the number of primary K shell vacancies. The Auger emission and fluorescence yields for vacancies produced in the K shell add to one.

The fluorescence yield brought about by higher shell transitions is more intricate though, because, unlike the K shell, the L and M shells possess more than one subshell, and depending on how the shells are ionized, the average fluorescence yield will change. Additionally, nonradiative, Coster-Kronig transitions take place within the subshells of atomic shells of identical principal quantum numbers [13,14].

By neglecting Coster-Kronig transitions, the fluorescence yield would be of the i^{th} subshell of a principal quantum shell of $X = L, M, \dots$, etc. and it is shown by:

$$\omega_i^X = \frac{I_i^X}{n_i^X} \quad (7)$$

However, primary vacancy distributions are altered by Coster-Kronig transitions, since the ionization from one subshell of a higher energy transitions to a subshell of lower energy. A more accurate expression for transition probabilities is as follows:

$$\omega_i^X + \alpha_i^X + \sum_{j=1}^k f_{ij}^X = 1 \quad (8)$$

Where Auger emission probability of the i^{th} subshell in shell X is expressed by α_i^X , when a nonradiative electron transition occurs. k represents the number of

subshells and f_{ij}^X stands for Coster-Kronig transition probability for a shift from a lower to higher subshell, specifically X_i to X_j . The last variables to note are the fluorescence yields found in the L shell: ω_{L1} , ω_{L2} , ω_{L3} . K, L, and M shell fluorescence yields and Coster-Kronig transition probabilities are given in tables 1 and 2.

Fluorescence yields and Coster-Kronig transition probabilities.

Atomic number	Element	ω_K	Atomic number	Element	ω_K
6	C	0.0009	45	Rh	0.81
7	N	0.0015	46	Pd	0.82
8	O	0.0022	47	Ag	0.83
10	Ne	0.0100	48	Cd	0.84
11	Na	0.020	49	In	0.85
12	Mg	0.030	50	Sn	0.86
13	Al	0.040	51	Sb	0.87
14	Si	0.055	52	Te	0.875
15	P	0.070	53	I	0.88
16	S	0.090	54	Xe	0.89
17	Cl	0.105	55	Cs	0.895
18	Ar	0.125	56	Ba	0.90
19	K	0.140	57	La	0.905
20	Sc	0.165	58	Ce	0.91
21	Ca	0.190	59	Pr	0.915
22	Ti	0.220	60	Nd	0.92
23	V	0.240	61	Pm	0.925
24	Cr	0.26	62	Sm	0.93
25	Mn	0.285	63	Eu	0.93
26	Fe	0.32	64	Gd	0.935
27	Co	0.345	65	Tb	0.94
28	Ni	0.375	66	Dy	0.94
29	Cu	0.41	67	Ho	0.945
30	Zn	0.435	68	Er	0.945
31	Ga	0.47	69	Tm	0.95
32	Ge	0.50	70	Yb	0.95
33	As	0.53	71	In	0.95
34	Se	0.565	72	Hf	0.955
35	Br	0.60	73	Ta	0.955
36	Kr	0.635	74	W	0.96
37	Rb	0.665	75	Re	0.96
38	Sr	0.685	76	Os	0.96
39	Y	0.71	77	Ir	0.96
40	Zr	0.72	78	Pd	0.965
41	Nb	0.755	79	Au	0.965
42	Mo	0.77	80	Hg	0.965
43	Tc	0.785	82	Pb	0.97
44	Ru	0.80	92	U	0.97

Table (1). K shell fluorescence yields ω_K for Z=6 through Z=92.

Fluorescence yields and Coster-Kronig transition probabilities.

Atomic number	Element	ω_1	ω_2	ω_3
54	Xe			0.10 ± 0.01
56	Ba	0.06		0.05 ± 0.01
65	Tb	0.18	0.165 ± 0.018	0.188 ± 0.016
67	Ho			0.22 ± 0.03
			0.170 ± 0.055	0.169 ± 0.030
68	Er			0.21 ± 0.03
			0.185 ± 0.060	0.172 ± 0.032
70	Yb			0.20 ± 0.02
			0.188 ± 0.011	0.183 ± 0.011
71	Lu			0.22 ± 0.03
				0.251 ± 0.035
72	Hf			0.22 ± 0.03
				0.228 ± 0.025
73	Ta		0.25 ± 0.02	0.27 ± 0.01
			0.257 ± 0.013	0.25 ± 0.03
				0.191
				0.228 ± 0.013
				0.254 ± 0.025
74	W			0.207
				0.272 ± 0.037
75	Re			0.284 ± 0.043
76	Os			0.290 ± 0.030
77	Ir			0.244
				0.262 ± 0.036
78	Pt		0.331 ± 0.021	0.262
				0.31 ± 0.04
				0.317 ± 0.029
				0.291 ± 0.018
79	Au			0.276
				0.31 ± 0.04
				0.317 ± 0.025
80	Hg		0.39 ± 0.03	0.40 ± 0.02
			0.319 ± 0.010	0.32 ± 0.05
				0.367 ± 0.050
81	Tl	0.07 ± 0.02	0.319 ± 0.010	0.300 ± 0.010
			0.373 ± 0.025	0.37 ± 0.07
				0.386 ± 0.053
				0.306 ± 0.010
				0.330 ± 0.021
82	Pb	0.07 ± 0.02	0.363 ± 0.015	0.337
		0.09 ± 0.02		0.315 ± 0.013
				0.32
				0.35 ± 0.05
				0.354 ± 0.028
83	Bi	0.12 ± 0.01	0.32 ± 0.04	0.367
		0.095 ± 0.005	0.38 ± 0.02	0.36
				0.37 ± 0.05
				0.362 ± 0.029
				0.40 ± 0.05
				0.340 ± 0.018

Table (2). Experimental L shell fluorescence yields ω_i [15]

1.3.5 Ionization Cross Sections

To express the probability that a particle induced K or L shell ionization occurs, we refer to nuclear cross sections. A larger cross section is representative of a larger probability for nuclear interaction. Cross section can be conceptualized as a two-dimensional area that represents the probability of fast ion interaction with a target atom. Nuclear cross sections are measured in “barn” (σ). One barn equals $10^{-28}m^2$. The atomic cross section decreases as atomic number increases, and a higher proton energy will cause a decrease in the cross section of a given target.

The physical geometry, or geometric cross section, is not of much concern as it can be either smaller or larger than the nuclear (interaction) cross section of the target atom. Originally, the Plane Wave Born Approximation (PWBA) model was used to estimate inner shell ionization cross sections. However, Brandt and Lapiki laid the groundwork for the Energy-Loss Coulomb-Repulsion Perturbed-Stationary-State Relativistic (ECPSSR) theory, which was a great improvement to the PWBA model, and is closer in predicting the total cross section of an atom. The ECPSSR model addresses critical interaction factors such as the increase in binding energy caused by the fast ion, and the Coulomb deflection forces the ion experiences as it approaches the target nucleus. To exclude very low Z materials, the ECPSSR model K shell calculations reconcile within a few percent of the most reliable cross section ionization data. [16]

K shell ionization cross sections for protons in Barns

Element	Z	Proton energy/keV							
		1000	1500	2000	2500	3000	3500	4000	4500
Mg	12	28780	37880	42150	43800	44040	43510	42560	41310
Al	13	17000	23990	27870	29850	30690	30860	30610	30130
Si	14	10150	15340	18590	20510	21570	22070	22200	22100
P	15	6124	9887	12500	14200	15270	15900	16230	16345
S	16	3729	6420	8455	9892	10870	11520	11930	12160
Cl	17	2311	4227	5790	6967	7824	8432	8853	9130
K	19	905	1856	2744	3490	4088	4557	4919	5193
Ca	20	575	1244	1907	2490	2978	3375	3692	3942
Ti	22	243	577	946	1298	1614	1887	2119	2313
V	23	160	398	672	945	1197	1421	1616	1783
Cr	24	107	271	481	692	892	1075	1237	1380
Mn	25	72	193	346	509	667	815	950	1071
Fe	26	49	137	251	376	502	622	734	835
Co	27	34	97	183	280	379	477	568	653
Ni	28	24	69	134	209	288	366	441	512
Cu	29	17	50	99	157	220	283	344	403
Zn	30	12	36	73	118	168	218	269	318
Ga	31	8.2	26	54	89	128	169	210	251
Ge	32	5.9	19	41	68	99	131	165	199
As	33	4.2	14	30	51	76	102	130	158
Se	34	3.1	11	23	39	59	80	103	125
Br	35	2.2	7.9	17	30	46	63	81	100
Rb	37	1.2	4.4	10	18	28	39	51	64
Sr	38	0.9	3.4	7.8	14	22	31	41	51
Y	39	0.7	2.6	6.0	11	17	25	33	42
Zr	40	0.5	2.0	4.6	8.6	14	20	26	34
Nb	41	0.4	1.5	3.6	6.7	11	16	21	27
Mo	42	0.3	1.2	2.8	5.3	8.6	13	17	22
Ru	44	0.17	0.71	1.8	3.4	5.5	8.2	11	15
Rh	45	0.14	0.56	1.4	2.7	4.5	6.6	9.2	12
Pd	46	0.11	0.44	1.1	2.2	3.6	5.4	7.5	10
Ag	47	0.083	0.35	0.89	1.7	2.9	4.4	6.2	8.2
Cd	48	0.065	0.28	0.72	1.4	2.4	3.6	5.1	6.8
In	49	0.051	0.22	0.58	1.1	1.9	3.0	4.2	5.6
Sn	50	0.041	0.18	0.47	0.93	1.6	2.4	3.5	4.6
Sb	51	0.032	0.15	0.38	0.76	1.3	2.0	2.9	3.9
Tl	52	0.026	0.12	0.31	0.63	1.1	1.7	2.4	3.2
I	53	0.021	0.096	0.25	0.51	0.9	1.4	2.0	2.7
Cs	55	0.014	0.064	0.17	0.35	0.6	0.96	1.4	1.9
Ba	56	0.011	0.053	0.14	0.29	0.5	0.8	1.2	1.6

Table (3). K-shell cross sections

L_{α} subshell ionization cross sections for protons in Barns

Element	Z	Proton energy/keV							
		1000	1500	2000	2500	3000	3500	4000	4500
Cs	55	530	1127	1763	2374	2930	3422	3851	4218
Ba	56	442	954	1509	2050	2550	2996	3389	3730
La	57	370	812	1298	1779	2228	2634	2994	3309
Ce	58	311	692	1119	1546	1949	2318	2648	2939
Pr	59	263	593	967	1347	1710	2044	2347	2616
Nd	60	224	511	842	1181	1508	1813	2090	2339
Gd	64	117	283	484	698	913	1119	1314	1493
Dy	66	83	206	359	527	697	864	1024	1174
Yb	70	47	123	221	331	446	561	675	783
Lu	71	40	108	195	293	398	503	606	706
Hf	72	35	94	171	259	353	448	542	634
Ta	73	30	82	151	229	314	400	486	570
W	74	26	72	133	204	280	358	437	514
Ir	77	17	48	92	143	199	258	317	377
Pt	78	14	42	81	127	178	231	286	340
Au	79	12	37	72	113	159	208	258	307
Hg	80	11	33	64	101	143	187	232	278
Pb	82	8.1	25	50	80	114	151	188	227
Bi	83	7.0	22	44	72	103	136	170	205
Th	90	2.6	9.3	20	33	49	66	84	104
U	92	2.0	7.4	16	27	40	54	70	86

Table (4). L shell cross sections

1.3.6 Spectral Background

The Detection limit in x-ray spectroscopy is primarily governed by the continuous background found within PIXE spectra. Inbound fast ions interacting with material surrounding the sample, or other materials found within the chamber, can incite background rays. A halo effect from a poorly collimated beam can produce x-rays in the target holder or chamber walls. The graphite collimator and Faraday cup can also be a sources of background x-rays if the detector is within line of sight to these components. To detect background x-ray peaks, while the Faraday cup is in normal operating position, the proton beam should pass through an empty target holder during the performance of a data acquisition run. Close placement of the sample and collimator, and proper beam alignment ensures that no material, excluding sample targets, will be irradiated by fast ions; ECU's PIXE apparatus has an imperceptible amount of x-ray induced background during data acquisition.

It is important to note that the key promoters of background with PIXE are proton induced primary bremsstrahlung, electron bremsstrahlung, and γ -ray emission. Primary bremsstrahlung produced by a charged particle is proportional to the square of its deceleration [17]. The electron and proton experience the same Coulombic forces, but their masses have a ratio of 1836:1, so primary projectile bremsstrahlung associated with incoming protons is negligible compared to the radiation produced by secondary electrons [18]. Regarding PIXE, the main generator of x-ray background is bremsstrahlung associated with the electrons that are ejected from the atom because of inelastic collisions. As the Coulomb field of a target nucleus scatters, or accelerates, an

ejected electron then it returns to its original bound state in the ionized atom, secondary electron induced atomic bremsstrahlung emission occurs.

When a resting electron of mass m_e encounters a head-on-collision with a charged projectile of mass M_p having an energy of E_0 , the electron can receive no more energy than T_m ; the maximum amount of kinetic energy that can be transmitted to the electron is:

$$T_m = 4E_0 \left(\frac{m_e}{M_p} \right) \quad (9)$$

Where secondary electron energies have values of 2.2 keV for a 1MeV proton beam, 4.4 keV for 2 MeV protons, and 6.535 keV for 3 MeV protons. When an ionized atom receives an ejected electron back into its bound state, bremsstrahlung is produced, but If the electron's final state is unbound, and there are no discrete values of allowed energies, photon emission and ionization continually occur, and a radiative ionization process transpires [19].

Secondary electrons are ejected inelastically in the same forward direction as the proton beam. Bremsstrahlung peaks at 90° with respect to the direction of the ejected electrons and is at a minimum in the direction of the incoming beam. Ideally the detector would be perpendicular to the sample (as far away from 90° as possible), but the chamber geometry prevents this. ECU's SDD detector is located 135° degrees from the forward direction of the ion beam. Even though at photon energies beyond 6 keV atomic bremsstrahlung are the primary contributor to the continuous PIXE spectrum, the bremsstrahlung is practically unnoticeable in ECU's x-ray fluorescence spectra and was of not much consequence during detector calibration.

γ -rays are much less visible in the PIXE spectrum and are more difficult to detect than background x-rays. γ -rays have energies in the hundreds of keV, a flat background in the 1-30 keV range is usually recorded due to the Compton scattering of γ -rays in the detector. Figure (11) shows elements that will yield the highest amounts of γ -rays. If these elements (e.g. lithium, boron, or sodium) are sited within a sample, a substantial quantity of γ -rays will be created in the target itself. With organic compounds, at proton energies below 3 MeV, Johansson [20] demonstrated that Carbon-13 was the primary source of γ radiation. Fluorine, however, because of the element's large cross section for $(p, p\gamma)$ and $(p, \alpha\gamma)$ reactions, has the highest γ -ray yield; therefore, it is advisable to avoid Teflon sample holders when performing PIXE. When carrying out proton induced x-ray emission, the most common source of γ -ray production is brought about by the aluminum used to achieve collimation within the drift line. γ -ray production is drastically increased with elements that are $Z \geq 27$, thus causing a decrease in detection limits [21]

Element	E γ (keV)	γ ray yield (x 10 ⁶ counts/ μ C Sr)			Reaction
		1.7 MeV	2.4 MeV	3.1 MeV	
Li	429	-	-	9.2	⁷ Li(p,n γ) ⁷ Be
	478	8.6	26.0	56.0	⁷ Li(p,p γ) ⁷ Li
Be	3562	-	0.02	2.5	⁹ Be(p, α γ) ⁶ Be
B	429	0.9	3.5	7.2	¹⁰ B(p, α γ) ⁷ Be
	718	-	0.12	1.3	¹⁰ B(p,p γ) ¹⁰ B
	2125	-	-	4.8	¹¹ B(p,p γ) ¹¹ B
F	110	0.1	7.2	11.0	¹⁹ F(p,p γ) ¹⁹ F
	197	0.2	20.0	37.0	¹⁹ F(p,p γ) ¹⁹ F
	1236	-	3.0	5.4	¹⁹ F(p,p γ) ¹⁹ F
	1349	-	1.3	2.1	¹⁹ F(p,p γ) ¹⁹ F
	1357	-	1.4	4.2	¹⁹ F(p,p γ) ¹⁹ F
	1459	-	0.9	3.9	¹⁹ F(p,p γ) ¹⁹ F
	6129	2.6	67.0	95.0	¹⁹ F(p, α γ) ¹⁶ O
Na	440	0.8	9.6	16.0	²³ Na(p,p γ) ²³ Na
	1634	0.2	9.9	19.0	²³ Na(p, α γ) ²⁰ Ne
Mg	1369	0.1	0.9	5.1	²⁴ Mg(p,p γ) ²⁴ Mg
Al	844	-	0.1	2.3	²⁷ Al(p,p γ) ²⁷ Al
	1014	-	0.3	4.6	²⁷ Al(p,p γ) ²⁷ Al
Si	1779	-	-	1.2	²⁸ Si(p,p γ) ²⁸ Si
P	1266	-	1.6	5.2	³¹ P(p,p γ) ³¹ P
Cl	1219	-	0.2	1.5	³⁵ Cl(p,p γ) ³⁵ Cl

Table (5). Gamma Ray yields for select light element targets with 10⁶ counts/ μ C-Sr or higher [22].

Nuclear interactions brought about by impinging protons or x-rays within the Pelletron accelerator can be a contributor to γ -ray emissions. As electrons are stripped from the H^- ion they accelerate back to the positively charged accelerator terminal, in turn, bremsstrahlung arises. Fortunately, during the calibration of ECU's PIXE system, no significant sources of background x- or γ -rays were observed.

A smaller contributor to background is brought about by naturally occurring γ -rays. If this background becomes significant, lead shielding should be wrapped around the detector to attenuate the naturally occurring γ -rays before they reach the silicon diode. In fact, this is a good practice even when natural background is not prevalent.

Sample charging caused by high energy protons can also result in background. If a sample has no route to dispel accumulated charge, the target will spark as it gives up its charge to an object with the nearest conduction path. The small electrical discharges will therefore cause x and γ radiation. This is one of the reasons that, the sample wheel has a copper grounding brush that constantly contacts the electrically isolated target carousel; it provides a conduction path for accumulated charges. If the specimens are electrically isolated from the target carousel, it is suggested to apply a thin coating of conducting carbon spray onto both the sample and the carousel to create electrical continuity between them.

1.3.7 Mechanical, Electrical, and Thermal Noise

Mechanical noise can be brought about by vibrations and loud noises in and about the specimen chamber, and it can diminish the efficacy of the Silicon Diode Drift detector. While the sound of the accelerator is intense during operation it occurs at a

high frequency and there has been no evidence of a decrease in detector resolution because of it. A more notable source of vibration that may affect the detector stems from the turbomolecular pump located on the bottom of the chamber, but again, there was no real indicator that these vibrations influenced detector performance.

Ripple, and electrical noise, can come from several sources. The connectors attached to the detector hardware and digital pulse processor are shielded to minimize noise resulting from electromagnetic fields. However, with ECU's PIXE configuration the most drastic sources of EMF are located far from the detector. There are some unshielded wires within the chamber (motor control terminal blocks and wires), but these wires should never be in use during active data collection, i.e. these components should have no effect on the SDD detector.

The outer shielding of the cables also provides continuity between the component housings and ground. These instrument chassis (the target chamber, the SDD detector, the PX5 digital pulse processor, and data acquisition PC) are all grounded closely through the same point (the accelerator itself), and there has been no ground loop noise detected in the circuitry. If spectral data shows degraded energy resolution, an oscilloscope can be used to test for noise pickup when it is connected to the auxiliary output of the PX5.

Thermal noise is reduced with the cooling circuitry of the detector and becomes insignificant below 233K. ECU's SDD has been shown to operate between 196 and 210 K – there has been no witness to thermal noise during calibration runs.

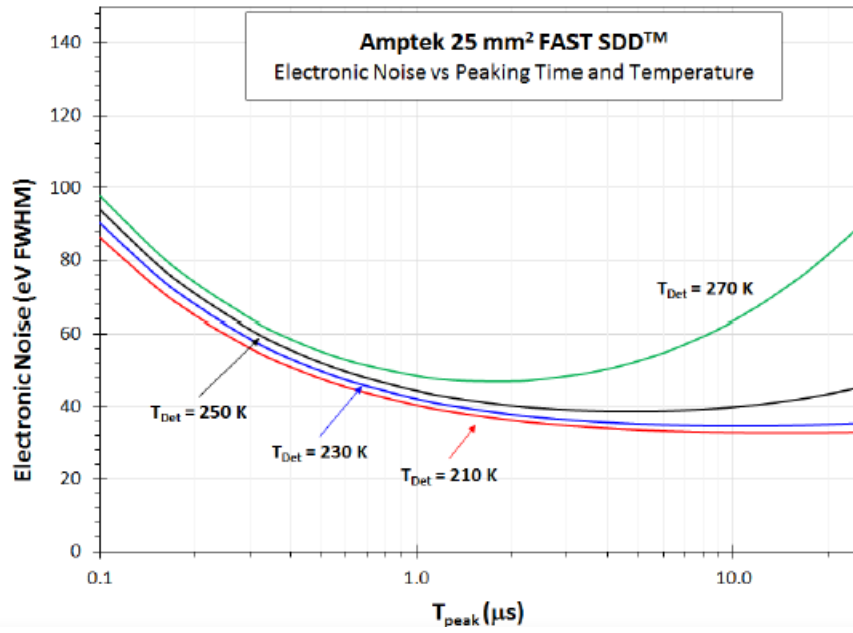


Figure (7). The Full width half max noise verses peaking time for the Fast SDD [23].

1.3.8 Sample Composition and Attenuation

The probability of x-ray production is not the only aspect in effective PIXE analysis. Target composition also influences x-ray attenuation and proton energy loss. The x-ray, or fluorescence, yield (Y_i) for an i^{th} element contained within a sample towards the direction of the detector is shown as:

$$Y_i = \frac{Q}{e} \int_0^d c(x) \sigma_i(E(x)) e^{-\mu \frac{x}{\cos \theta}} dx \quad (10)$$

While passing through the target material, the projectiles lose energy by:

$$E(x) = \int_0^x S(E) dx' \quad (11)$$

Where the particle stopping power, $S(E)$ is

$$S(E) = \frac{dE}{dx'} \quad (12)$$

If the concentration $c(x)$ of the i^{th} element does not change throughout the sample, the connection between elemental concentration and x-ray intensity is provided by

$$I_i = QC_i K_i \quad (13)$$

Where the calibration constant K_i is independent of the sample if both the target matrix and experimental geometry (θ, ϕ) remain constant.

$$K_i = \varepsilon \int_0^d \sigma_i(E(x)) e^{-\mu \frac{x}{\cos \theta}} dx \quad (14)$$

To quantify, a fundamental parameter approach can be applied by using the x-ray fluorescence cross sections (σ_i), x-ray attenuation (μ), and particle stopping power in calculating the calibration constant [25]

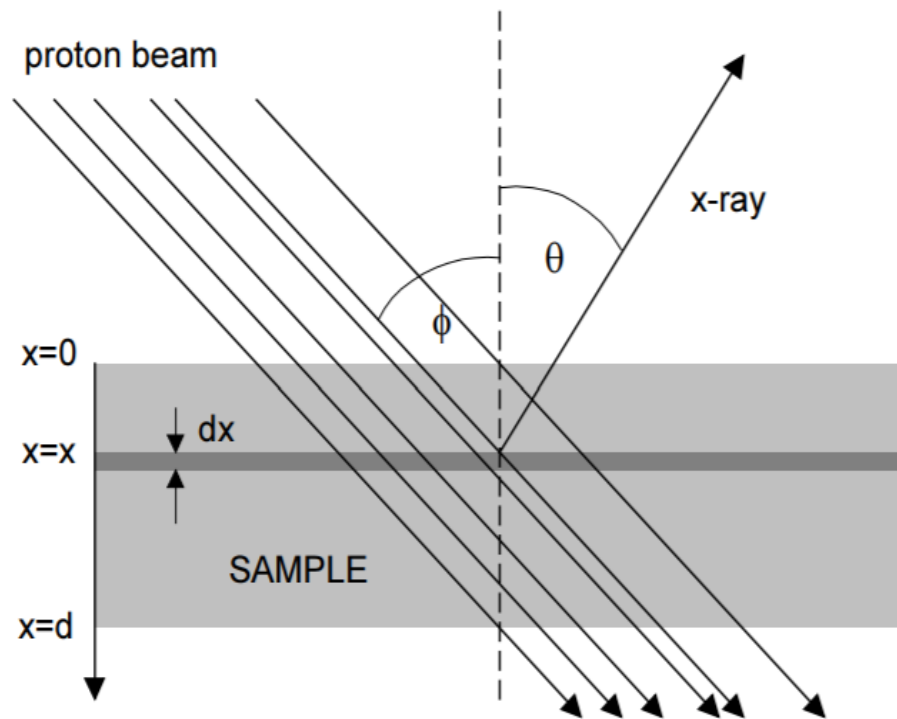


Fig (8) demonstrates a typical illustration for PIXE analysis. [24]

PIXE targets fall into two main categories: thin and thick specimens. Thin targets (usually films) are classified as such, because only a small portion of beam energy is lost while passing through the sample making analysis relatively simple [26]. In contrast, thick specimens (specimens that completely stop the beam) are typically easier to prepare for analysis, but other factors, such as a smooth and flat impact surface with a known thickness and matrix structure, along with a controllable and reproducible experimental environments, should be considered. As mentioned, the impact surfaces of thick targets should be as smooth and flat as possible while offering precise and duplicable angles to the particle beam; the sample should be perpendicular with respect to the beam, and at a 45° with respect to the direction of x-ray emission. An impeccably flat and polished surface will yield higher x-ray intensities in contrast to samples with substantial irregular rough patches in relation to the x-ray attenuation length of a target. The effects of curvature and coarseness of a sample have been meticulously calculated with considerable accuracy [27,28]. An unblemished surface allows the assumption of a uniform dispersion of elements within the sample during analysis. If the surface is irregular, uncertainties in the elemental distribution should be accounted for. But equations (10) and (11) make it evident that dependable PIXE relies on several more factors that determine a well-defined sample. Factors such as statistical uncertainty in the determination of peak area I_i , detector efficiency ϵ , particle energy E_0 , and the total exposure of the sample to the incoming proton beam are additional criteria for successful PIXE analysis [29]

Specimens can be heterogeneous in their original state and may need to be reduced and homogenized either physically or chemically before proton irradiation. Geological samples typically qualify for this treatment. It is noteworthy that homogenizing a sample will make the analysis of spatial variations within the target impossible. These specimens can be ground and mixed with a binding agent, carbon works well as a binding agent due to its conductive properties.

A colloidal suspension of powdered target material can be pipetted onto a substrate such as chemically treated Mylar® that will form a film for analysis after the liquid dries on the filter material. Solids can be dissolved through acid reduction and deposited on the filter to dry. This method offers impartial analysis by guaranteeing a standardized sample of a large portion of primary specimen material. This method also allows for the addition of known elements within the solution used to set internal standards within the sample. The drawback to this method is that the sample thickness is not always uniform. For example, when a bead of solution evaporates, the suspended particles become thicker in the last place evaporation occurred. However, with substances like dried blood, it tends to dry thicker on the outer ring of the droplet. An acceptable remedy is to pretreat the substrate to cause a hydrophilic inclination within the substrate [30]. A solution of nitric acid and polyvinylpyrrolidone (PVP) can be used to etch and create a hydrophilic surface on the polyethylene terephthalate film (Mylar®).

Particulate matter from the atmosphere can be collected with polycarbonate filters like a clean mylar film left in a desired environment for several hours.

Specimen heating caused by beam energy being lost within a sample can cause the vaporization of organic and trace element targets. It is recommended that for thin

specimens under vacuum, the proton beam current density should not surpass $5nA/mm^2$ [31]. Radiation damage to polycarbonate substrates is largely unnoticeable after proton irradiation, but after oxygen is reintroduced to the evacuated target chamber, it diffuses into the polycarbonate filter and reacts with free radicals caused by proton irradiation [32]. Radiation damage becomes evident, when holes form in the filter.

Between the elements of atomic number $20 \leq Z \leq 30$, detection limit for K x-rays is at its lowest, but L x-rays are prevalent between $70 \leq Z \leq 80$. These limits get slightly higher in atomic number as proton energy increases. PIXE analysis is an inadequate technique for many of the rare earth elements ($Z=57-69$), as they fall between the two windows of optimal detection [33].

2. Experimental Methods

2.1 Proton Beam Creation

Creating an ion beam capable of reaching energies of several MeV necessitates many phases of beam manipulation that begins at the ion source and ends at the experimental apparatus. Ions must be created, selected, focused, accelerated, and guided through a high vacuum environment before it ever reaches an experimental target chamber. To begin, it is appropriate to start with a consideration of how ions are created.

2.1.1 Cesium Sputter Source

Ions are created through a sputtering process involving cesium vapor. The sputter process ensues when a solid target material is bombarded by energetic particles. As this method occurs, atoms from the solid target are ejected due to the transfer of momentum between the energetic particles and the target's atoms causing collision cascades within the target material to occur. Upon recoil of these cascades, and when reaching the target surface, if the particle has an energy above the surface binding energy, atoms are liberated from the material. Since a great amount of momentum is needed for this reaction to occur, the heavy cesium ion is preferred over other elements. Additionally, cesium has an abundance of free electrons that are available to donate to the sputtered atoms. ECU uses a High Intensity General Ionics Corporation 860 A Cesium sputter ion source which was founded by Middleton in the early 80's [34]. This source can create ions from nearly all elements, excluding noble gasses, and can achieve currents in the range of hundreds of μ -amps. [35-37]. To

generate the proton (H^+) beam required for PIXE, it is necessary to create H^- ions with the source. To accomplish this, a small amount of TiH_2 powder is firmly packed into a copper target cathode. The sputtering process begins when solid cesium is heated in an oven set around 350 K. To ensure that no cesium condensation can clog the valve it is held at a higher temperature than oven itself. Consequently, cesium vapor is released into a chamber containing a cooled cathode held at a -7.5-kV bias [34] and an extremely hot (~ 1375 K) tantalum ionizing coil. These components are arranged opposite of the sputter chamber with respect to each other. The cathode is held at a lower temperature so that some of the cesium vapor will condense on it. On the other end of the chamber, through the process of thermal emission, cesium vapor is ionized as the tantalum coil boils off electrons from the cesium vapor through thermal ionization. As the cesium vapor is changed into positively charged Cs^+ ions, they are accelerated through a potential difference of ~ 2 kV where they are forced to bombard the cooled and negatively biased sputter cathode. This phenomenon occurs as per Coulomb's law

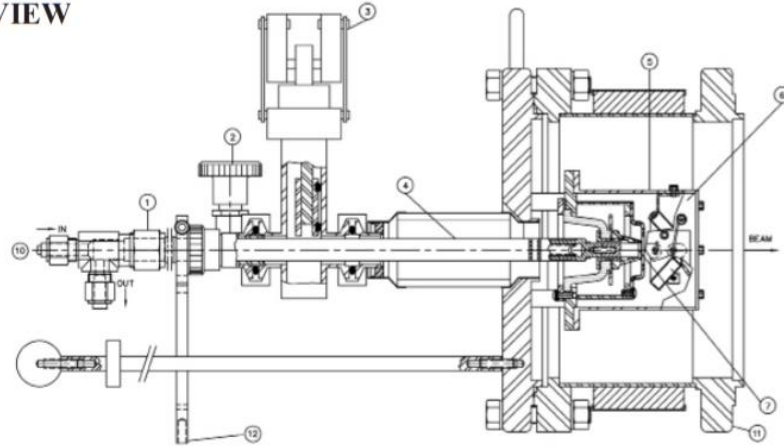
$$F_C = Eq' \quad (15)$$

where,

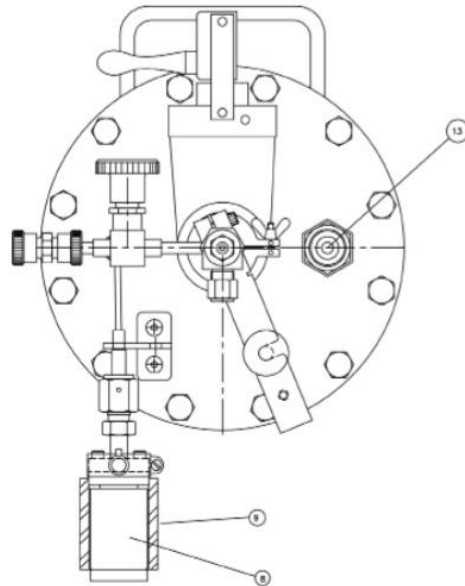
$$E = \frac{\Delta V}{d} \quad (16)$$

Where F_C represents Coulomb force, E denotes electric field, q' is a charge immersed in the electric field, ΔV denotes the voltage potential difference between two charged objects, and the distance between the charged objects is given by d .

SIDE VIEW



FRONT VIEW



1. Heat exchanger
2. Roughout port
3. Valve
4. Cathode holder
5. Ionizer chamber
6. Ionizer
7. Cathode
8. Cesium oven reservoir
9. Heater band
10. Cooling input/output
11. Source ground
12. Cathode voltage
13. Ionizer current

Figure (9). Diagram of Cesium Sputter Source [38]

After ionized cesium is accelerated through the potential difference, the positive cesium ions slam into the copper sputter cathode that contains titanium hydride; resultantly, a multitude of differing molecular species are sputtered from the TiH_2 and the copper housing [39]. Many of these sputtered particles are atoms that become negatively charged when they pick up electrons after collisions with cesium atoms previously condensed on the cooled surface of the cathode. Since the cathode is held at a negative potential, the newly created negatively charged ions accelerate away from the cathode and through extractor electrodes that are held at a higher voltage potential with respect to the cathode [40] the ions have an approximate energy of 6 keV at this stage. Following this, without altering beam energy, an electrostatic unipotential, or Einzel lens, is used to focus the ions prior to entering the 30-kV linear accelerator

After vertical guidance of the ion beam through use of a magnetic field, it is necessary that the ~36 keV H^- ions are isolated from the unwanted molecular species emitted from the previous sputtering process. The ions that emerge from the linear accelerator all have different momentums including the H^- ions. To capitalize on this, the beam line encounters a 25° bend selector magnet. The magnet ensures that only certain species of specific mass and velocity can negotiate the arc of the turn. The intensity of the magnetic field determines what ion passes the 25° deflection successfully. Essentially, the inflection magnet selects ions that have the same magnetic rigidity by:

$$Br = \sqrt{2mE/q^2} \quad (17)$$

Where mE indicates particle mass and energy, q is the ionic charge, r denotes radius of curvature, and B indicates the magnetic induction field.

The manipulation of the beam is brought about by Lorentz forces, and can be understood by the equation:

$$F_L = q[E + (v \times B)] \quad (18)$$

The Lorentz force F_L acts on a particle of electric charge q with a velocity v due to an external electric field E – in this case, 0 N/C – and magnetic field B [41].

With ECU's inflection magnet setup, the desired ions need to acquire a counterclockwise trajectory as they round the bend. Therefore, an adjustable upward oriented magnetic field is used to “filter” out the undesired particles, while allowing the sought after H^- ions to pass through the bend. The Lorentz force can be equated to a centripetal force in this instance by:

$$F_C = qvB \sin \theta = m \frac{v^2}{r} \quad (19)$$

Where m indicates the mass of the ion, r represents the radius of the ion's trajectory while in the magnetic field, and θ being the orientation of the magnetic field with respect to the velocity of the particle, namely 90° . Ion momentums are all different upon entrance into the selector magnet's field, and therefore the Lorentz force serves to isolate the proper ion species. This is exhibited with a rearrangement of the cyclotron formula:

$$B = \frac{mv}{qr} \quad (20)$$

To allow effective passage of H^- ions through the bend, the correct magnetic field is tuned using the inflection magnet. Other unwanted ions travel with too large of a radius and end their flight by striking the walls of the beam line; the nonessential ions are basically “filtered” out by the selector magnet. At this juncture, the H^- ions encounter a second low energy Einzel lens, and an electrostatic steerer to augment beam transmission into the tandem accelerator.

2.1.2 Pelletron Tandem Particle Accelerator

The Tandem NEC 6SDH-2 Pelletron model 2AA0&2310 Accelerator used in the calibration of East Carolina University’s PIXE apparatus, is capable of operating at a charged terminal voltage of 2 MV. The accelerator is made up of multiple systems including charging chains, high voltage plates, a high voltage terminal, vacuum pumps, water cooling components, a beam line, and a gas circulation system. All this, among other mechanisms that make up the accelerator, are contained in a large 4 m long cylindrical tank.

The Pelletron is very similar to a Van de Graaff accelerator in that it operates on the same physical principles. The difference between the Pelletron design and the Van de Graaff design is that the Pelletron has a pellet chain, or short conductive tubes joined by electrically insulated links, whereas the Van de Graaff generator uses a rubber belt. The Pelletron chain design is superior to a rubber belt, since it allows for a more uniform charge distribution, which allows for a higher stability of the terminal voltage, and, therefore, allows for a higher particle energy. The chain can also move at much higher

velocities than a belt; naturally, this leads to more accumulation of charge on the terminal [42].

The Pelletron chains are made up of links containing metal pellets coupled with nylon links that have electrically insulative properties. By means of an induction system that does not incorporate corona discharges or brushing contacts, the high voltage terminal of ECU's Pelletron is positively charged. The charging process begins when the negatively-charged inductor electrode forces electrons off the metal pellets while they have electrical continuity with the grounded drive pulley. Since they are still in the negative induction field, as the pellets lose contact with the pulley they continue to hold a net positive charge. Subsequently, the chain delivers the positive charge to the high-voltage terminal, as the chain arrives at the terminal, the chain once again passes through a negatively biased suppressor electrode to impede arcing as it becomes electrically common with the terminal pulley. While in the negatively biased suppressor region, the pellets efficiently deposit charge on the pulley, in turn, giving the terminal a net positive charge. [43-45]

To develop a consistent electric potential gradient within the accelerator's electric field, on either side of the central high voltage terminal, there are several high voltage plates that are sequentially located to progressively step the voltage down to 0 V on both ends of the accelerator tank.

The hollow terminal will accumulate positive charge until there is enough potential to overcome the breakdown voltage of the gas that it is immersed in. The breakdown voltage of air at STP is $\sim 2.38 \times 10^6$ V/m between two plane surfaces at 5

mm apart. In this type of electric field, air will ionize becoming conductive plasma, and accumulated charge will arc to the nearest object of lower potential. The breakdown voltage of gas is specific to the chemical makeup of the gas, and a charged terminal can be held at higher potentials depending on the insulative properties and pressure of the gas surrounding it. With the high voltages that the terminal can achieve, and in consideration of the proximity of the terminal relative to other conductive components of differing voltage potentials, at a pressure of about 550 kPa, the volume of space containing the accelerator's high voltage components and ground points is flooded with sulfur hexafluoride gas.

SF_6 is a gaseous dielectric that acts as a superior electrical insulator, it is also nontoxic and chemically stable. ECU's accelerator utilizes this gas to prevent corona discharges; arcing will give way to an unstable terminal voltage and will inevitably cause damage to internal components [46]. SF_6 has an electrically insulative property that allows for a very high breakdown voltage – approximately three times that of air at STP (2.95 @ 5 mm between charged surfaces). The breakdown voltage for SF_6 is increased even further by pressurizing the gas.

The pressure of the SF_6 gas is limited to the vacuum seals that are installed on the beamline; if the SF_6 pressure is too great this will create a high-pressure differential and the high vacuum environment in the beam line will be breached by the SF_6 . Consequently, the ion beam will become scattered and eventually stopped by collisions with the SF_6 molecules found in the beam line. SF_6 gets hot during normal operation, and a temperature increase of the insulating gas will lend itself to a degraded breakdown voltage, so a water cooling system is used to regulate the temperature of

the insulating gas. The SF_6 gas is also heavy, and, without agitation, will naturally settle at the bottom of the tank. The accelerator tank requires a homogeneous distribution of gas within the vessel, so a blower unit is incorporated into the system to uniformly distribute the gaseous sulfur hexafluoride.

The tandem accelerator is so named because it has two stages of acceleration. The negative ions are accelerated toward the MV positive terminal as they enter the tank. When the ions reach the geometric center of the tank, they enter a gas assembly and N_2 gas is used to strip of their electrons. Nitrogen gas is used because of its high electronegativity (affinity for electrons), and low-cost relative to oxygen or fluorine.

This electron stripping process occurs when an H^- ion beam enters the gas assembly, and after subjection to nitrogen gas, the negative ion beam becomes a positive ion, or proton (H^+), beam. The newly formed proton beam is subsequently accelerated away from the positive terminal in the second stage of the acceleration. This means that if the terminal was adjusted to have a potential of 2 MV the singly charged H^- ion would be given 2 MeV of energy during its first stage of acceleration. After the negatively charged ion is stripped of electrons it becomes a proton, and it is forced away from the positively charged terminal and moves downstream toward the grounded high-energy side of the accelerator. The second acceleration gives the proton an additional 2 MeV of energy, and this yields a total proton energy of 4 MeV upon emergence from the accelerator.

Since the protons are electrically charged particles, the beam, due to Coulomb forces, will naturally diverge as protons travel down the drift line, so, once again, the

beam is focused before it arrives downstream at the experimental apparatus. A quadrupole magnet acts much like a lens to a beam of light. Through a duplet configuration of quadrupole magnets, the beam is constrained both horizontally (width) and vertically (height) resulting in a highly focused proton beam. The focused protons will allow for a higher beam current that will cause more collisions with target material. Conversely, if the ion beam current is too high the quadrupole can be used to defocus the beam yielding fewer proton-target interactions. This may improve the count rate within the detector.

After leaving the field generated by the two quadrupole magnets, the beam undergoes a final vertical alignment through use of a vertical steering, or “up/down”, magnet. The vertical steering magnet ensures that the beam will be vertically aligned with the target.

Following the vertical alignment, the protons encounter a final magnetic field that is induced by a switching, or analyzing, magnet. This magnet essentially selects one of the seven experimental beam lines for the protons to travel down. The PIXE apparatus is located on ECU.’s “L-45” line; the switching magnet guides the ions in this direction. After clearing the magnet, the beam must pass through a manually operated gate valve used to isolate the PIXE apparatus from the tandem accelerator and other experimental beam lines. This valve protects the other experiments and the accelerator from vacuum failure within the PIXE chamber or anywhere beyond the switching manifold. If the valve is open, the beam travels down the last segment of drift tube and appears in the proton induced x-ray emission analysis chamber. Beam current can be measured at this point

with the Faraday cup located in the back of the chamber if the sample wheel is empty and in the correct position.

At several points between the source and experiment, the beam's physical shape and beam current can be monitored using quartz crystal scintillators and Faraday cups. Scintillators that can be moved in and out of the beam path fluoresce when irradiated with charged particles, this allows for the observation of the physical shape of the beam profile. Faraday cups are conductive metal cups that are used to count the number of charged particles contained in a packet of ions. This allows the measurement of beam current at the low energy side of the line (before the accelerator) and the high energy side of the line (after the accelerator), and inside the PIXE chamber. Like the quartz viewers, the Faraday cups can be positioned in or out of the path of the ion beam. The transmission rate has been observed at an approximate maximum of 80% between H^- ions and protons collected in ECU's low and high energy Faraday cups.

By utilizing several turbomolecular pumps situated at different points along the drift line. High energy ions can be transported from the source to the experimental chamber via high vacuum conduit. To minimize collision probability between protons and gas molecules in the beam line, a vacuum is maintained at pressures around 10^{-7} Torr (10^{-5} Pa) inside the chamber. At 10^{-1} to 10^{-2} Pa, energy loss for protons is insignificant. However, in efforts to increase the mean free path of fast ions, the beam lines, starting from sputter source and ending at the target, are held under high vacuum, typically on the order of 10^{-8} Torr (10^{-6} Pa).

To prevent collisions with residual gas, ECU's PIXE chamber vacuum is maintained between 10^{-6} and 10^{-7} Torr ($\approx 10^{-4}$ Pa). Beam halo brought about by

scattering inside of the target chamber will distort the beam profile and may increase the intensity of background peaks in the spectra [47].

The experimental chamber and drift tube are made from rigid materials that can withstand high pressure differentials all while maintaining low outgassing rates and vapor pressures; specifically, stainless steel, aluminum, and plexiglass [48].

To bring the chamber down to 10^{-4} Pa, a mechanical pump is used for rough and exhaust pumping, while a turbomolecular pump brings the PIXE apparatus to its operational pressure. The Turbomolecular pump is a good option as it does not risk chamber/sample contamination like a diffusion pump, and it can bring the chamber to vacuum relatively quickly – this is important if many samples are expected to be analyzed quickly. A disadvantage to the turbomolecular pump: while under operation, the mechanical bearings of the turbomolecular pump cause vibrations throughout the PIXE chamber, and this can potentially affect the energy resolution of the Silicon Drift Diode detector [49].

Ion/energy	Range in air (mm)	ΔE (keV/ μm) in air, or ΔE (eV/m) in vacuum 10^{-4} Pa
p, 1 MeV	23.25	0.0273
p, 2 MeV	71.25	0.0169
p, 3 MeV	140.52	0.0126

Fig (10). Proton energy attenuation in air and vacuum

2.1.3 PIXE Beam Requirements

Protons with energies between 1-3 MeV are typically used in PIXE analysis. The beam current correlates directly with count rate. Less than 1 μA of beam current is needed for successful PIXE analysis [50]. Some specimens, such as those prepared from powder or solution, have irregular thicknesses and nonhomogeneous surfaces, so it is important to attain a uniform intensity distribution across the beam [51]. This can be achieved by defocusing the beam with the magnetic quadrupole, and then collimating its gaussian intensity distribution in such a way that the charge flux will be nearly uniform within the cross-sectional area of the proton beam. This technique causes a diminished beam current at the sample, so the accelerator needs to supply several hundred nanoamperes on the high energy side [52].

2.2 Target Chamber

2.2.1 Chamber Specifications

The chamber and metal flanges are all made from aluminum and held together with stainless steel hex head bolts. Flanges including nine blanks, five portholes, five adapters, two valves, and a drift tube are all attached directly to the chamber and maintain vacuum with Viton O-rings. The base and lid are also outfitted with Viton O-rings. The ion gauge, Faraday cup, and all Electrical feedthroughs rely on KF vacuum fittings. Only one Conflat fitting is located between the gate valve and the L-45 PIXE drift line. All the components within the chamber are bolted down to the aluminum base of the chamber. The PIXE apparatus uses a Kurt J. Lesker G075K Ion Gauge that is

controlled with a Varian BA2 SENTORR gauge controller to monitor pressure within the chamber.

The chamber has an Agilent Technologies DS 302 Roughing pump to evacuate the fore-line. The chamber is brought to high vacuum with a Leibold and Harris TURBOVAC 360 turbomolecular pump that is controlled with a Turbotronic NT 150/360 turbomolecular pump controller. The turbomolecular pump is located at the base of the chamber with the intake facing up. Only a very coarse screen separates the volume of the chamber from the blades of the pump, so care should be taken in preventing debris from falling into the pump.

There are four valves associated with the PIXE chamber. Attached between the selector magnet manifold and the drift tube attached to the PIXE chamber is a manually operated gate valve. The gate valve serves to isolate the accelerator and other experiments from the PIXE beam line. In a situation where vacuum is lost in the PIXE chamber during a period of non-use, other experimental lines and the accelerator itself would be protected. The second is a pneumatic valve located on the turbomolecular pump's exhaust port. This valve isolates the fore-line from the turbomolecular pump and is of convenient configuration when performing maintenance to the fore-line while desiring to keep vacuum in the chamber. The toggle switch to control this valve is located on the east side of the PIXE chamber. An additional valve is located under the CCD camera on the northeast side of the chamber. This should be open during initial evacuation of the chamber. This allows gas to travel from the drift line directly to the chamber in lieu of evacuating gas through the small hole of the collimator. Leaving this valve open will reduce evacuation time. Finally, the relief valve used to bring the

chamber back up to atmospheric pressure is located on the south side of the chamber. This valve should be opened gradually when bringing the chamber back up to atmosphere as the velocity of air entering the chamber can disturb and fleck off pieces of delicate samples into the blades of the precision turbomolecular pump.

In the interests of economic analysis, most chambers have multi-specimen capability. ECU uses a carousel arrangement which allows for the analysis of up to 24 specimens in sequence.

The target chamber houses an automated target wheel that is driven by stepper motors connected to LabView Software installed on the data acquisition computer. The wheel is always positioned orthogonal to the incoming ion beam, and the geometry inside the chamber is held constant. The cross section of the collimated beam is significantly smaller than the cross section of the sample holder frame, this serves to minimize background. The sample wheel contains 24 individual sample positions and can be moved translationally (it can move the sample laterally with respect to the beam) and rotationally (clockwise and counterclockwise) to select the desired target. The graphite beam collimator is approximately 0.25" in diameter and is located approximately 1.125" away from the sample wheel. The wheel is secured with a thumbscrew and can be easily removed after the filter wheel is taken off its mount. There are 24 small holes in the outer circumference of the wheel. These holes allow the optical interrupter switch (H21B1) to detect target positioning. The samples are held with an outer steel ring. Before samples are loaded into the wheel this ring must be removed.

The original construction of the sample wheel isolates it from earth ground. If steps are not taken to provide continuous discharge of the specimens then they will undergo cyclic buildup of positive potential, each cycle ending in a spark. The positive potential attracts electrons, whose interaction results in an intense additional bremsstrahlung background contribution in the x-ray spectrum. To remedy this, a copper grounding brush was attached to the base of the chamber. Without impeding sample wheel operation, the brush slides along the wheel as it rotates all while maintaining continuity with the sample wheel in any position. It may be beneficial to coat specimens with a thin conducting layer of carbon if they do not achieve electrical continuity with the sample wheel, and thus, earth ground [53]

With specimens thick enough to stop the beam entirely, the specimen holder must be insulated from the chamber and the specimen should be connected directly to a charge integrator [54].

Provision is necessary for the insertion of a suite of x-ray absorbing filters between specimen and detector. By filtering intense x-ray peaks, other trace elements can be identified, and pile up can also be reduced. The use of such filters acts to emphasize certain spectral energy regions at the expense of other regions of low information content [55].

The filter wheel has similar features to the sample wheel. The filter holder has six positions and can be rotated counter and clockwise. Like the sample wheel, position alignment for the filter wheel is detected with an optical interrupter switch.

The sample and filter wheels are rotated by means of a Mercury stepping motor, and the translational movement of the sample wheel is controlled by a Vexta PK245-03AA, 12V, 0.4 A motor. Motor speed and direction can be controlled remotely by means of the Lab View 2017, Version 17.0.1F1 (64-bit) interface. Lab View communicates with optical sensors mounted on the sample and filter wheels to indicate if the sample or filter is in its correct position. A green indicator light turns on when the target is lined up, and a green alarm light flashes if the translational motor reaches its boundary limits. Going beyond the sample wheel's translational constraints can damage the translational motor, the filter, or sample wheel. To operate the motors, the National Instruments USB X-series USB-6341 USB hub must be turned on first, and then the motor driver module must be switched on. The Lab View software should be initiated last.

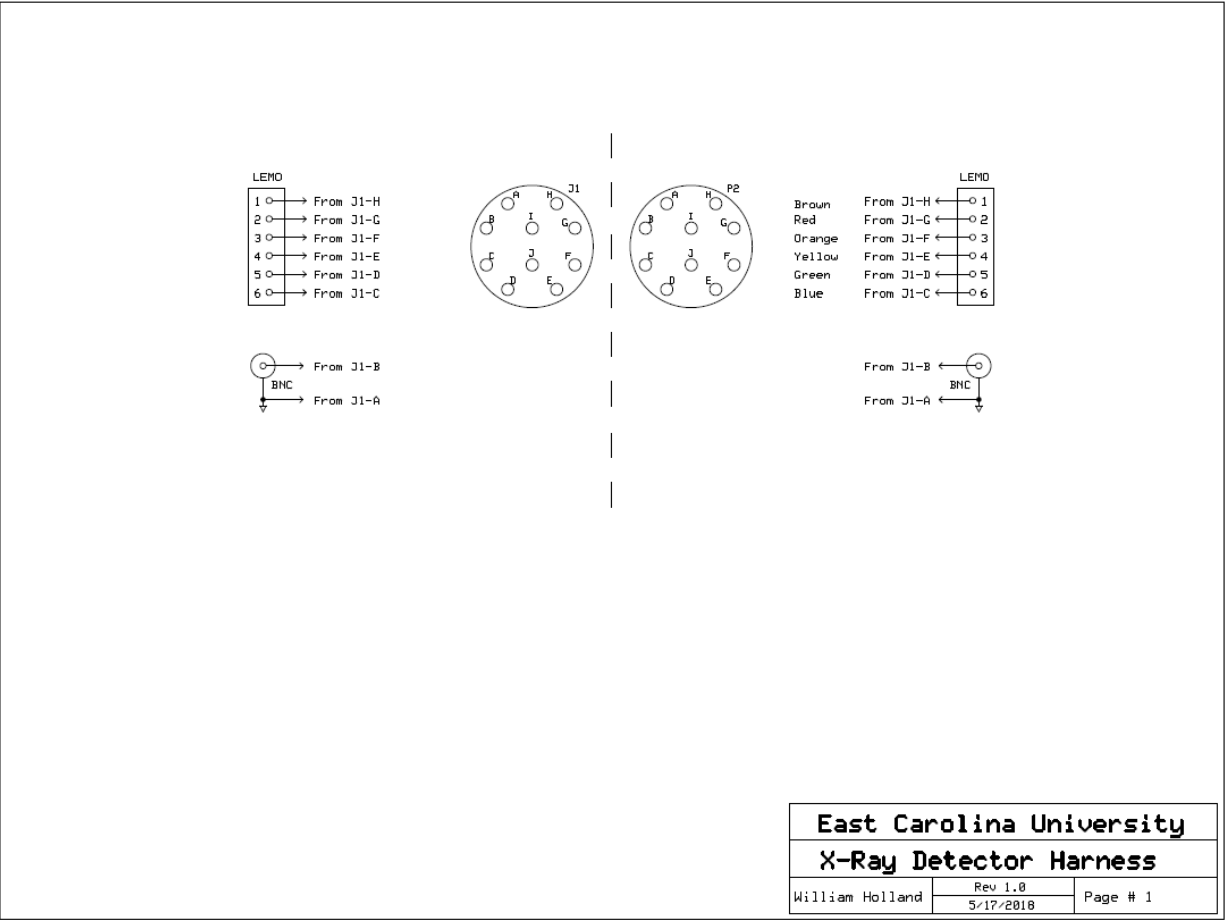


Figure (12). Lemo connector to electrical feedthrough diagram

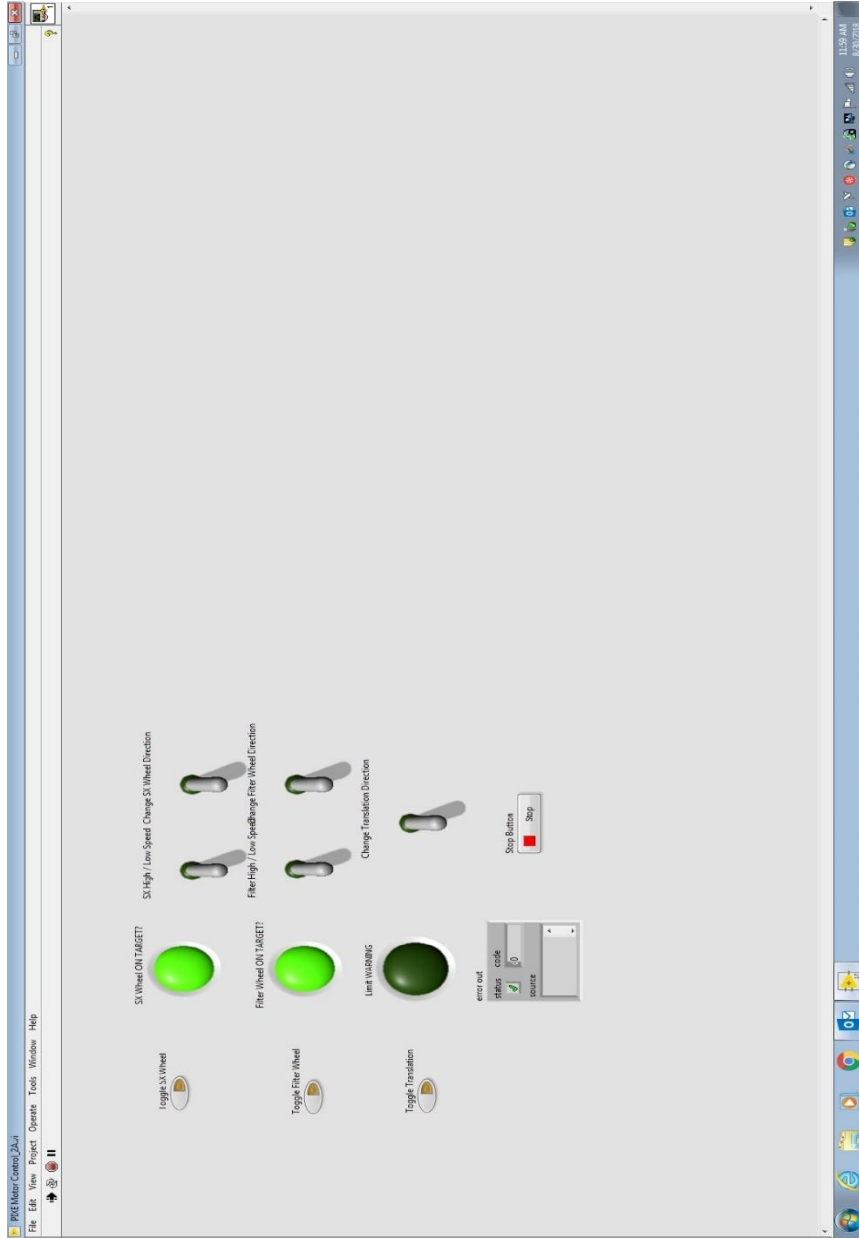


Figure (13). Lab VIEW motor control interface

2.2.2 Chamber Monitoring

Five portholes are strategically mounted on the chamber walls to allow for direct visual inspection of the chamber environment. To attain precise sample positioning with respect to the beam, a CCD camera is positioned to view the sample surface. With EZ Grabber V3.0 software and a Panasonic GP-MF552 B/W CCD camera attached to the center porthole on the northeast side of the chamber, the operator is allowed remote viewing at the data acquisition PC. The black and white camera is focused at the point where the proton beam meets the target. The sample wheel, sample number, filter wheel, collimator and beryllium detector window can all be viewed from this vantage point. This camera configuration allows for efficient and safe viewing of the sample while under analysis and between runs; this arrangement lets the operator see the beam, aids in selecting the target, and helps in adjusting the physical position of the target.

To monitor beam current, a Faraday cup is located on the west side, or back of the chamber. The cup itself is made from carbon, and it is operated with a pneumatic valve that allows motion into or out of the beam path. The Faraday cup can be controlled, and the beam current data can be viewed, remotely with the accelerator interface software. A quartz viewer is located directly downstream of the faraday cup. The cup must be moved out of the beam path to view the beam spot at the back of the chamber.

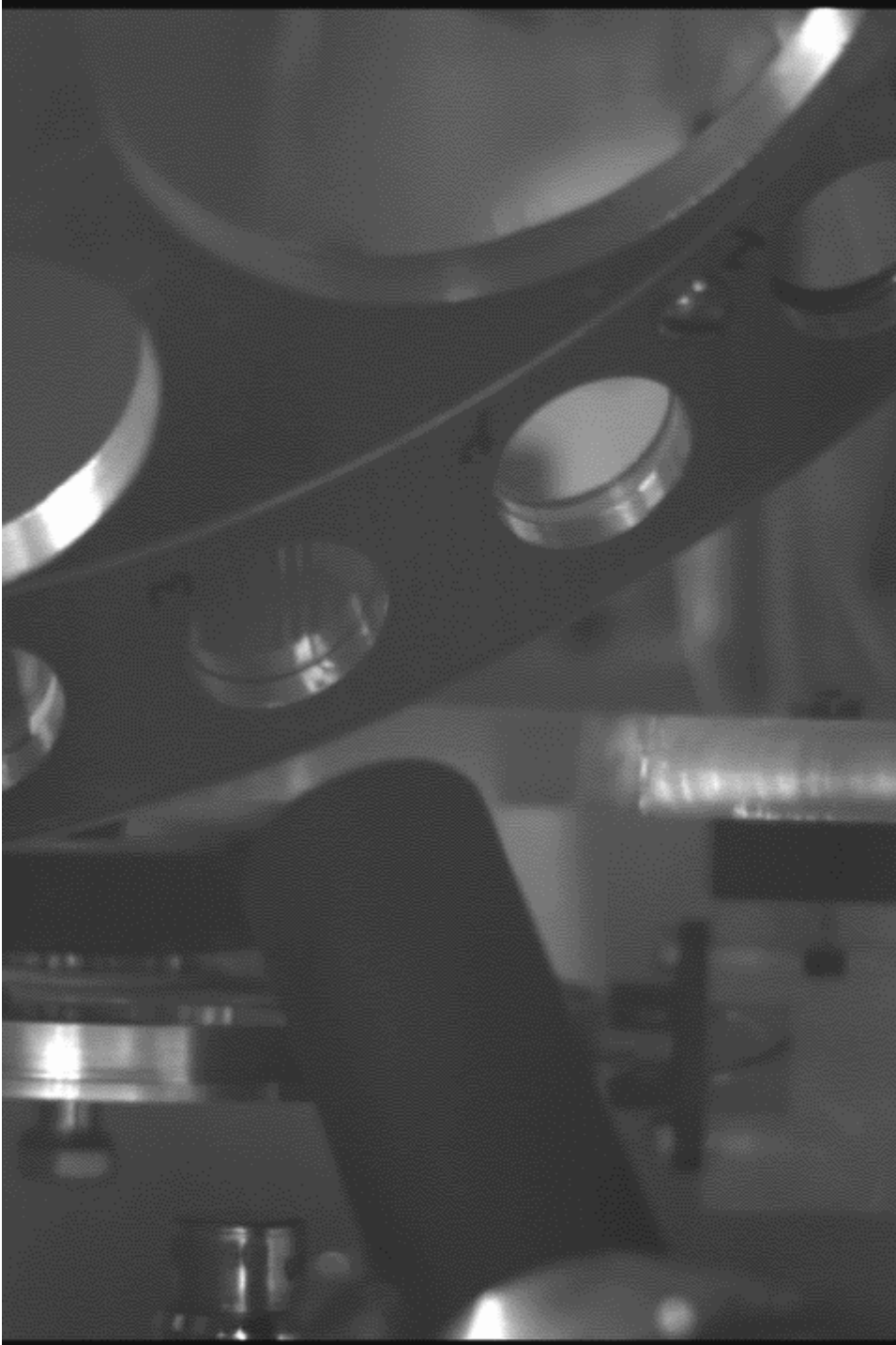


Figure (14). View from ECU's PIXE CCD camera

2.2.3 Collimators

To create an appropriate beam spot in probing the target composition it is necessary to focus and collimate the beam. The profile of the ion beam should ideally have a Gaussian distribution upon emergence into the chamber, but it is collimated to achieve a uniform current distribution along the cross section of the beam. A series of collimators dictate the shape of the beam's cross section. In ECU's PIXE apparatus, the first collimator located inside the incoming beam tube and it adjusts the shape of the beam. The second collimator acts as an anti-scattering collimator that will shear off disbanding protons. Failing to collimate a second time will result in x-rays being emitted from chamber materials that are in line-of-sight to the beryllium window of the detector, this can negatively affect spectra. Since much of the beam is collimated before hitting the sample, it is important to generate a much higher current from the low energy side of the accelerator

Collimators are preferably fabricated from elements that do not give rise to unwanted x- or γ -rays via the (p, γ) reaction, as x- and γ -rays will increase the continuous background in the x-ray detector [56].

Near the detector, carbon (graphite), which emits no detectable x-rays, is the general choice for beam collimation. Even though proton energies above 3.236 MeV are out of the typical range for PIXE, protons at these energies will cause neutron production in the carbon collimator.

2.2.4 Detector Positioning

The geometrical arrangement of components located within the PIXE chamber will greatly affect x-ray attenuation, beam energy loss, and bremsstrahlung emissions brought about by secondary electrons. Maximum beam penetration into the sample occurs when the beam is perpendicular to the target. Ideally, the detector would be placed at the same position as the collimator, but this is physically impossible.

Therefore, the next preferred location for the detector is at 135° to the beam direction because here the intensity of bremsstrahlung background is significantly less than it would be at 90° relative to the direction of the beam [55].

2.3 XR-100 Fast Silicon Drift Diode Detector

A Silicon Drift Diode is a type of photodiode that operates much like a SiPin photodiode. The difference is the SDD's special electrode arrangement. The electrodes induce an electric field that optimizes charge collection with a minimal input capacitance. A planar detector has a significantly higher capacitance than the SDD, and therefore suffers greatly from electronic noise at short shaping times. Electronic noise caused by short shaping times has a direct relationship with capacitance, so the SDD is capable of a better resolution, specifically for low energy x-ray spectra. This also applies to SDDs with large surface areas.

2.3.1 SDD Detector Theory and Operation

The prevalent noise in silicon x-ray Spectroscopy is pink ($1/f$) noise. This noise increases with input capacitance and high frequency shaping times, but the low capacitance silicon drift detector offers lower noise at very fast shaping times. The

Silicon Drift Detector has cylindrical symmetry. The design is like a planar, or Silicon-PIN, detector in that the SDD has a negatively biased (-50 V) front implanted P+ cathode (region that intercepts incident x-rays), but what differs is the anode. The anode is just a small plate just microns in diameter; this offers a phenomenally low capacitance. With this very small anode much of the SDD would not be used, and the collection efficiency would be greatly reduced. This problem is overcome by placing several concentric annular drift electrodes around the anode. This increases the active volume of the diode while maintaining an extremely low capacitance. Essentially, the rings ensure that the useful area of the detector diode is independent of the input capacitance.

The p+ implanted electrode rings are negatively biased with resistive dividers in between. The outer ring is held at -100 V, and the voltage progressively steps down by increments of 10 V ending at the inner ring which is held at virtual ground. This creates an electric field that sweeps charge carriers radially toward the anode. Electrons drift for several microseconds, and for the total drift time a current is induced within the diode. As the holes and electrons move from locations of higher to lower concentrations, a diffusion current occurs causing the charge cloud to grow. This increases the collection time for interactions occurring at the outer edge of the active volume of the drift diode which causes the risetime in the preamplifier to fluctuate. The preamplifier risetime remains very fast though, because the virtual ground electrode acts as a shield to the anode; only drift motion occurring after the final electrode will serve to deliver the signal current to the anode. Operationally, the SDD has the same resolution as a Si-pin detector but at 10 to 20 times higher peaking frequency. This allows for the processing

of 10 to 20 times the count rate while maintaining quality data acquisition; statistics can be obtained very quickly.

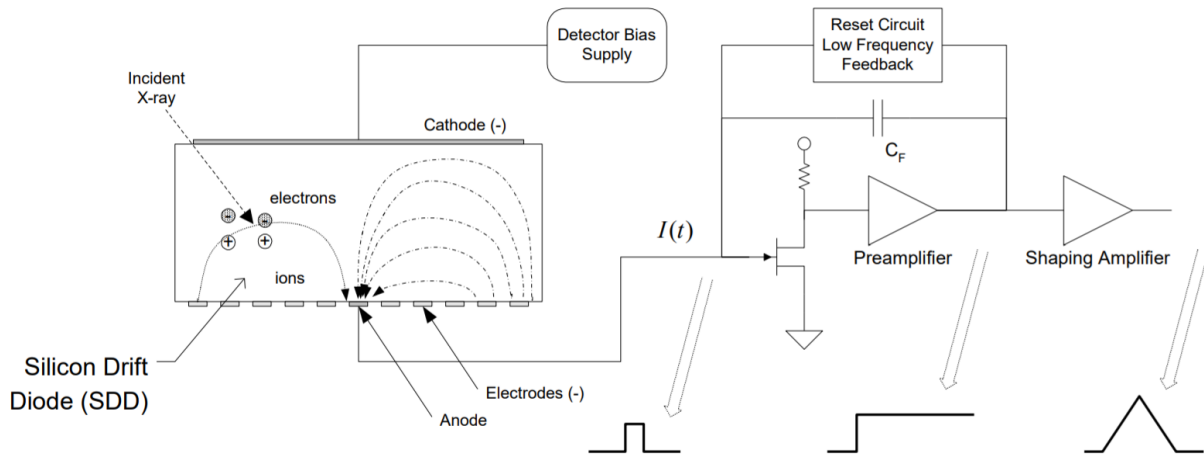


Figure (15). Illustration of the operation of a silicon drift diode (SDD) [66]

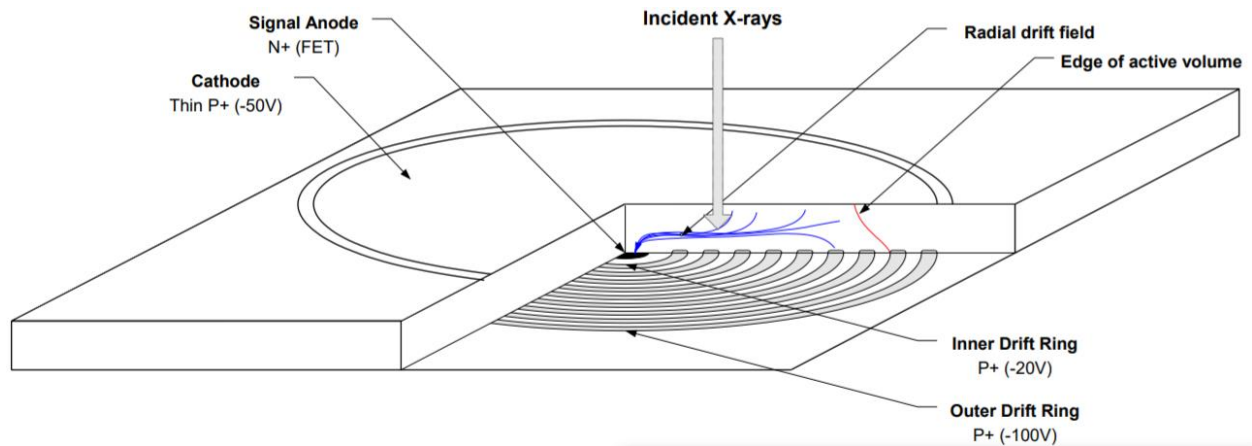


Figure (16). Illustration of the operation and construction of the XR-100 Fast Silicon Drift Diode [57]

2.3.2 Temperature Control

The XR-100 FAST SDD's temperature is controlled by a closed loop temperature control and does not require LN₂. Temperatures between 210 and 230 K can be reached at maximum cooling. The FAST SDD dissipates about 1 Watt during operation. To adapt the detector to the evacuated environment, and lower the detector's operational temperature, a large portion of the detector's casing surface area was placed in contact with, and conducts heat to, an aluminum mount located inside the target chamber. The detector stabilizes after getting below 233 K, small temperature fluctuations below this point will not hinder detector performance. Decreasing detector temperature will increase energy resolution. An increase in the operating temperature of the detector causes an increase in leakage current; as a result, degraded energy resolution [58].

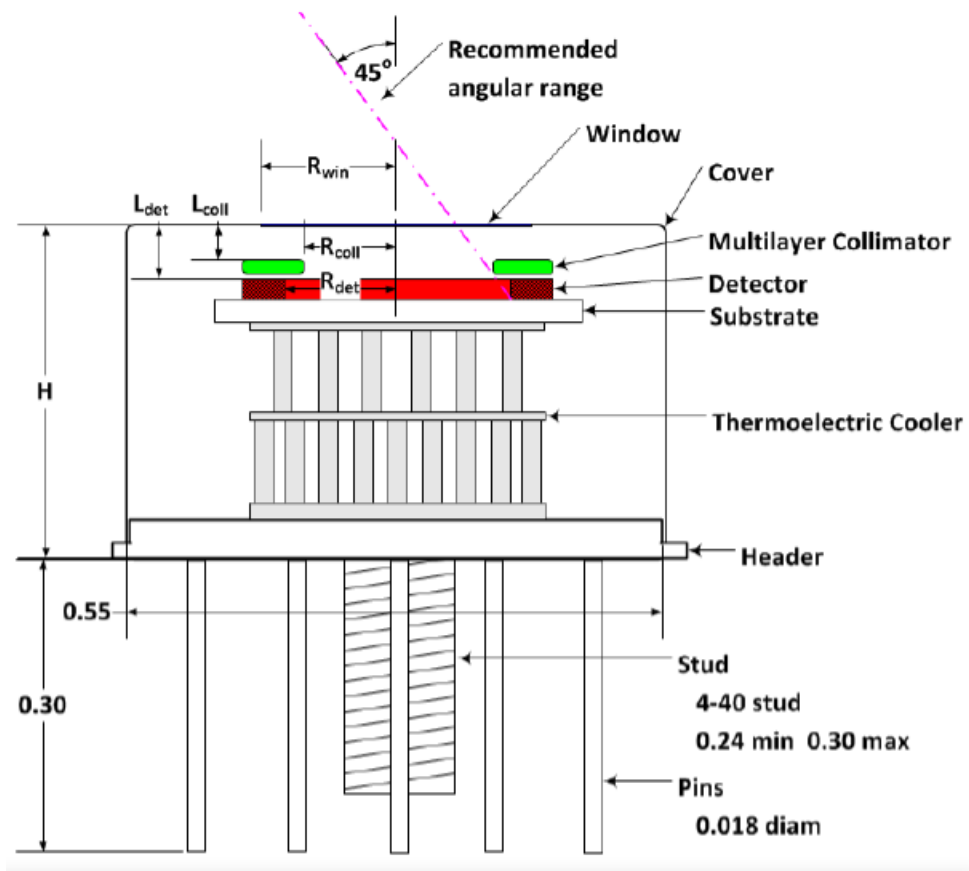


Figure (17). Diagram of the SDD detector core [59]

2.3.3 Resolution

High resolution for spectra with well-spaced peaks is not a priority, but it becomes more important when separating closely spaced peaks, or in distinguishing peaks from background. At short shaping times the SDD has a very low electronic noise. The area of the SDD is not much of a factor in terms of resolution; the SDD provides high resolution with a large surface area. Lower noise at a high-count rate gives way to better resolution, this is especially true at energies below 5 keV.

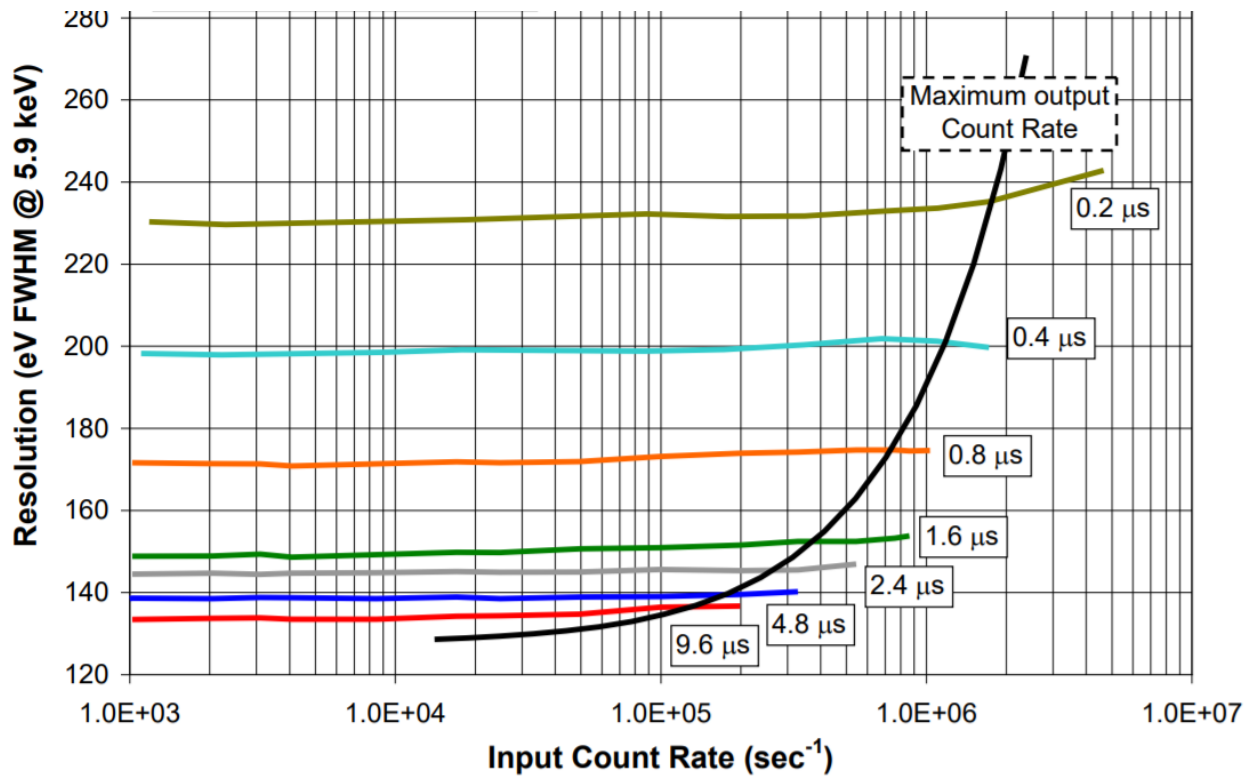


Figure (18). Full Width Half-Max resolution in eV vs. Input Count Rate Frequency

At standardized settings, ECU's XR-100 FAST SDD was factory tested using $Fe - 55$. With a $4 \mu s$ peaking time the Mn 5.9 keV K_{α} line had a resolution of 131.8 eV FWHM. Temperature, flat top width, and peaking time all affect the detector's energy resolution. If there is a high-count rate the peaking time can be shortened to provide narrow peaks. This will allow more events to be counted, but the spectra will be noisier. If the count rate is low, the peaking time can be increased, in turn, improving resolution (less noise), but venturing out of the noise corner will be costly to resolution. Short peaking times decrease dead time, offer high throughput, and deal well with high count rates, the tradeoff is the electronic noise associated with fast peaking times. Peaking times that are too long with respect to the incoming counts will cause pulse pile-up. A certain peaking time where electronic noise is at its least is called the "noise corner". As peaking times move away from the noise corner resolution becomes inferior in quality. Ideally, the detector should be operated at the peaking time that corresponds with the noise corner, or a little bit faster to resolve higher count rates. The proper peaking time depends largely on the exact detector and preamplifier.

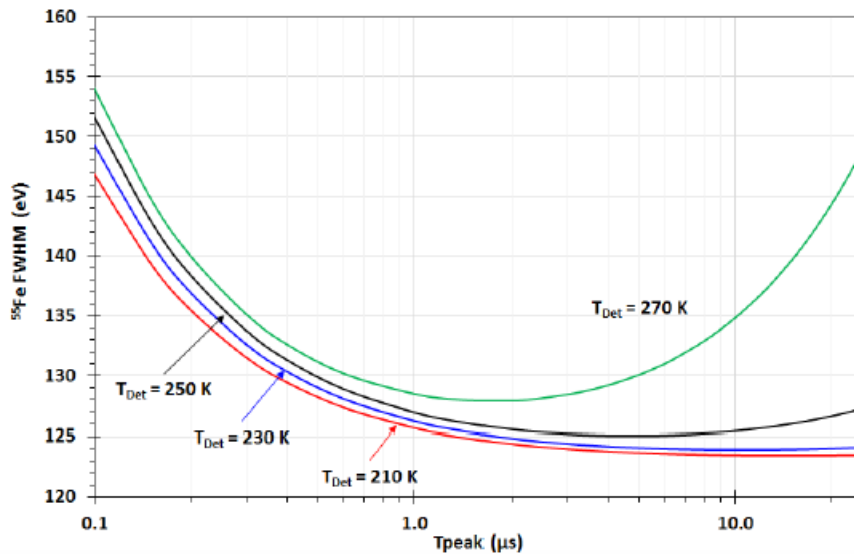


Figure (19). Iron-55 FWHM resolution vs. Peaking Time and Temperature of the XR-100 Fast SDD [61].

2.3.4 Efficiency

Low energy x-ray detection is mostly limited by the depth of the $12.5 \mu\text{m}$ beryllium window. At low energies, air molecules, the beryllium window, contact material at the front of the detector, and the dead layer can interact with the photons, so they will not be detected. The dead layer is a thin layer of oxide about 400 \AA thick and a subsequent layer about 200 \AA thick where the E-field is weak. This leaves a total dead layer of 600 \AA , which is relatively shallow, and is not a major factor in x-ray attenuation. High energy x-ray detection is subjugated by the depth of the silicon detector. High energy x-rays pass through the detector without interacting if the active volume is not thick enough to attenuate them.

With a 0.5 mil ($12.5 \mu\text{s}$) beryllium window, about 90% of incident x-rays with energies between 2-3 keV enter the detector. The efficiency starts to drop off at 10-12 keV where an approximate 90% are detected. Efficiency drops off below 10% after 30 keV where they are Compton scattered, or simply pass through the detector. To view spectra above 80 keV it is probable that the data acquisition will take a very long time.

Regarding figure (22), the beryllium window makes up the first layer of the detector, while the second layer is made up by a dead layer, active volume of the detector comes next, then the final layer is comprised by the inactive volume of the detector. There are several scenarios that may transpire as an x-ray encounters the detector. Incoming x-rays may interact with the beryllium window, the contact material, or the dead layer, and will never reach the detector (Blue arrows), which causes efficiency loss at low energies. The red arrow depicts a photon interacting with the

active volume of the detector which will cause an output signal. When this occurs, the x-ray energy may be entirely absorbed by the active volume and will be counted as a full energy peak. When an x-ray is attenuated by the active volume, the total energy of the event may be reduced if the x-ray scatters out of the active volume, or if the x-ray Compton scatters another particle out of the active volume. If the x-ray is not attenuated by the active volume (green arrows) the event is never counted, this causes a loss of efficiency at high energies [62]. Elemental analysis of light elements such as Na and Mg call for a very thin beryllium window with no other absorbers present. At 3 MeV, protons will backscatter into the detector; therefore, light-element analysis can be performed using protons with energies around 0.5 to 1 MeV. Backscattered ions will be absorbed by an 8-12 μm thick beryllium window.

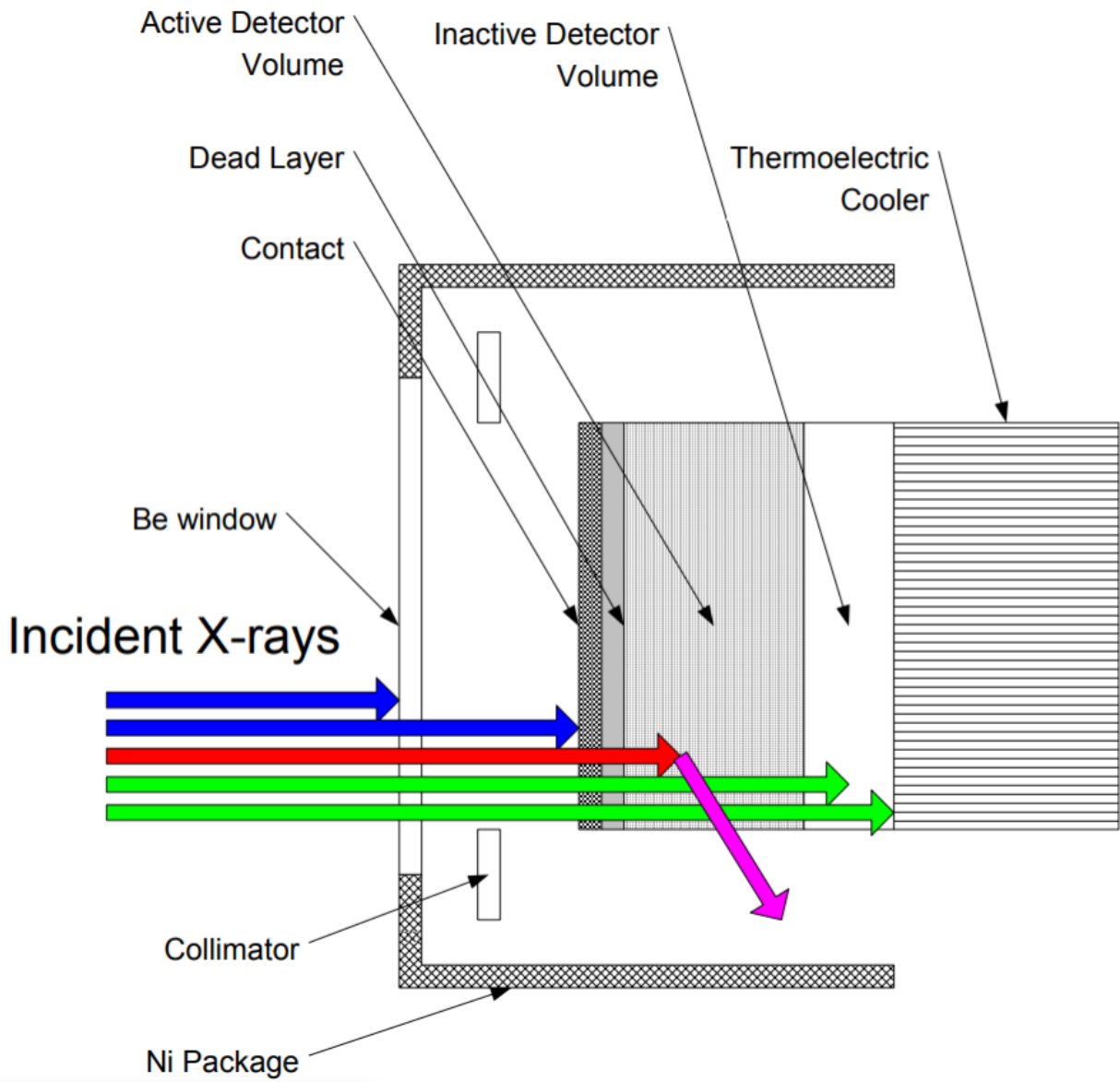


Figure (20) Model of detector efficiency [63].

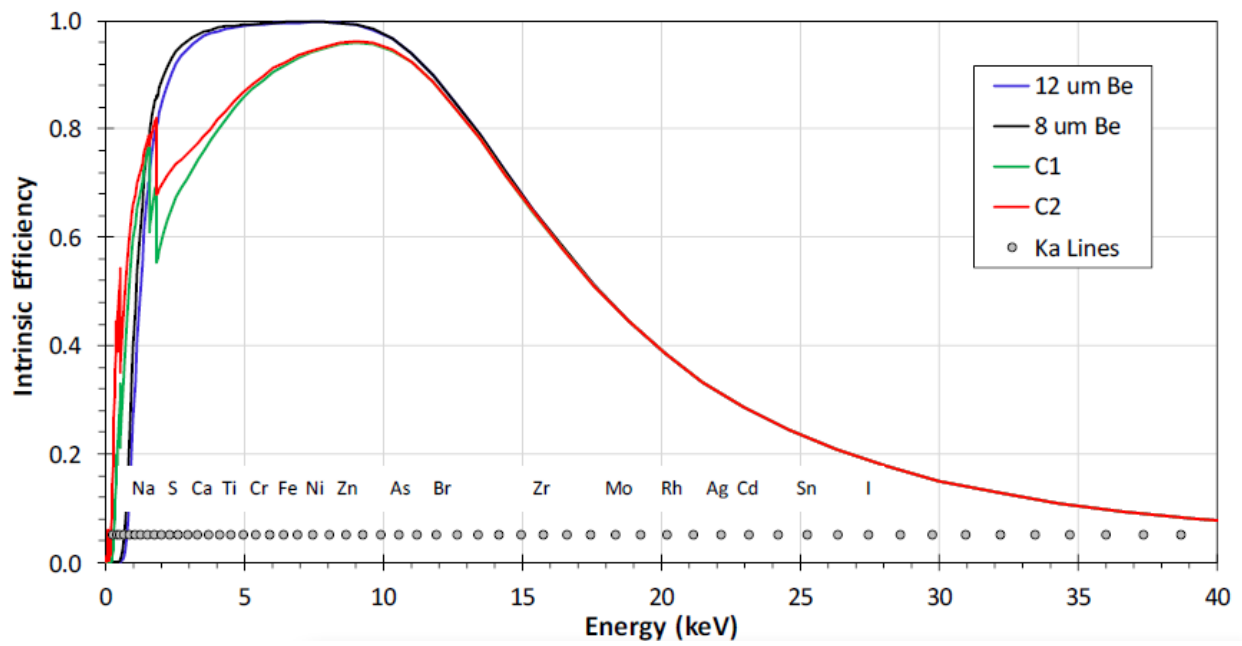


Fig (21) Efficiency vs. Energy Fast SDD (ECU detector: 12 μ m Be window) [64]

2.3.5 Multi-Layer Collimator

To reduce aberrations in the spectra, a 17 mm^2 multi-layer collimator is located behind the beryllium window of the XR-100 FAST SDD. The collimator shields edges of the SDD to limit, or completely stop, potential interactions from occurring outside the active volume. The collimator is layered in order of descending Z materials: tungsten, chromium, titanium, and aluminum. The fluorescence peaks of previous layers are absorbed by the succeeding layers. After passing through the lowest Z material the undesired x-rays are far below the detection limit. The same materials used for multi-layer collimation are also good materials for attenuation and collimation filters.

2.3.6 PX5 Digital Pulse Processor

The PX5 offers superior resolution under higher count rates. The multichannel analyzer and shaping amplifier found in analog detection electronics are replaced by the PX5 digital pulse processor. The DPP digitizes preamplifier output, tracks peak amplitude, and bins data to send to the user interface. PX5 settings are all configured through the DPPMCA software.

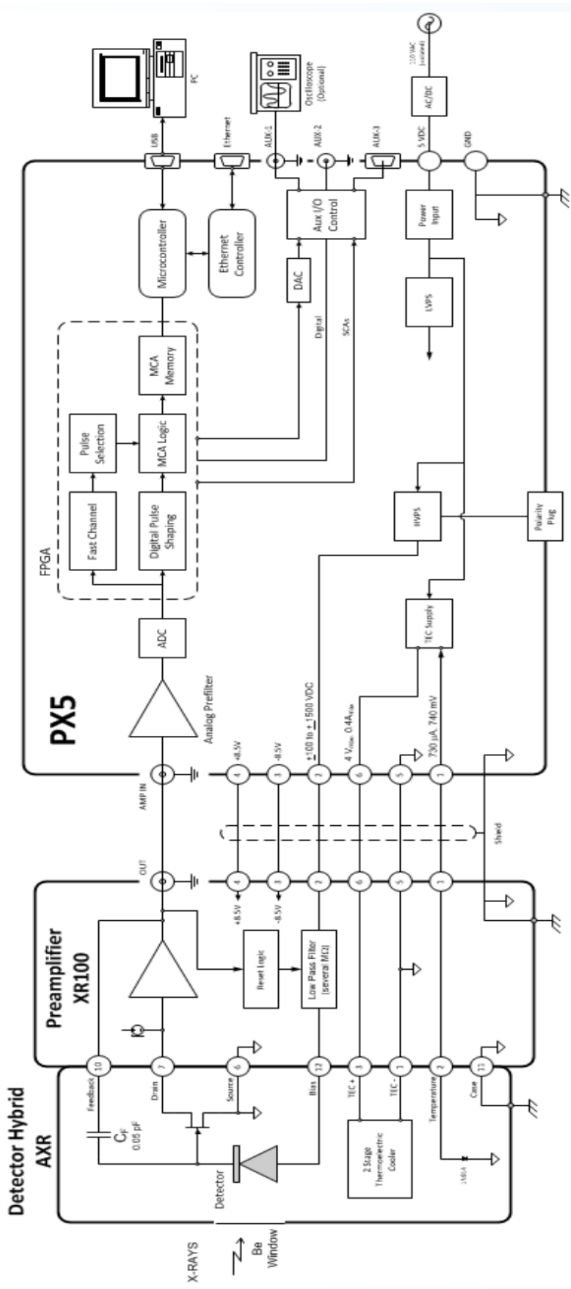
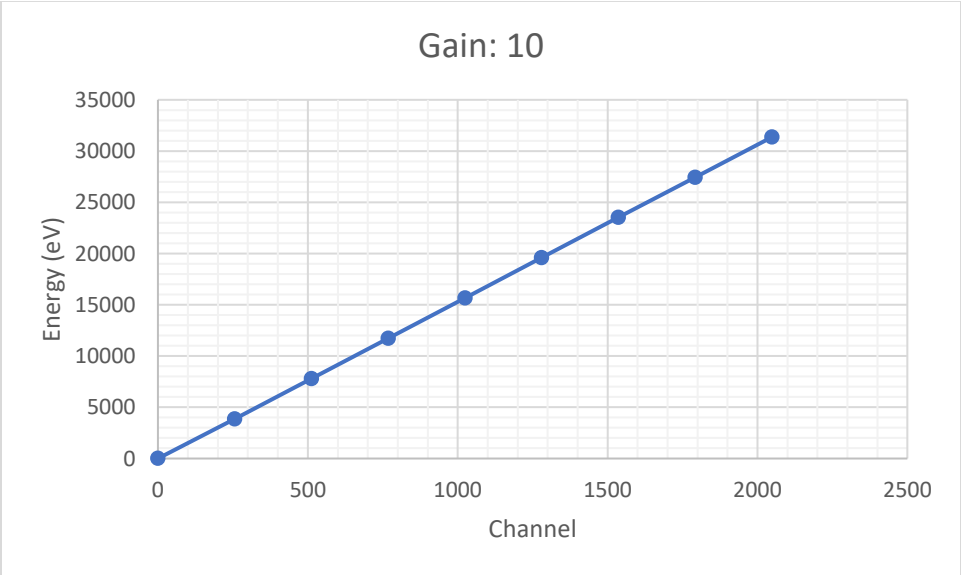
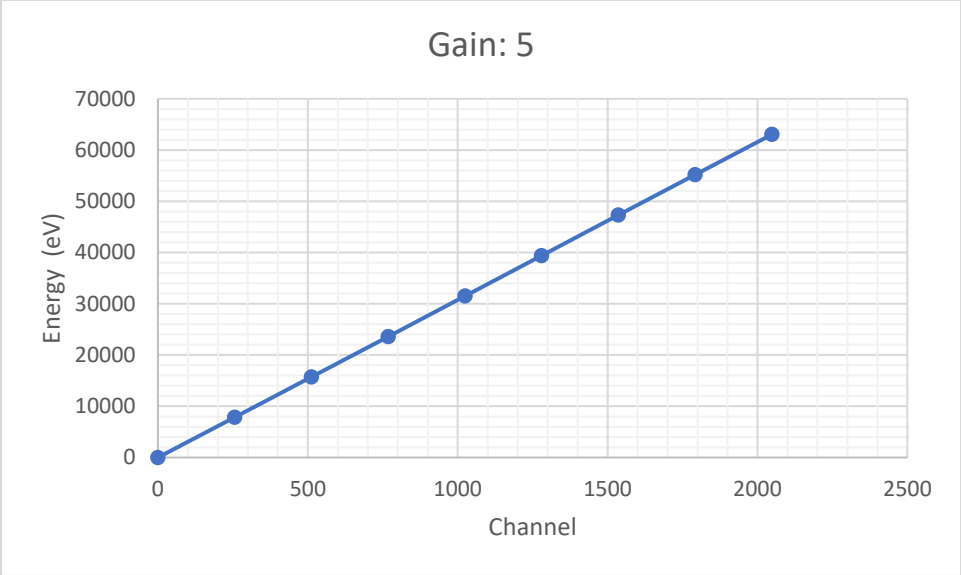


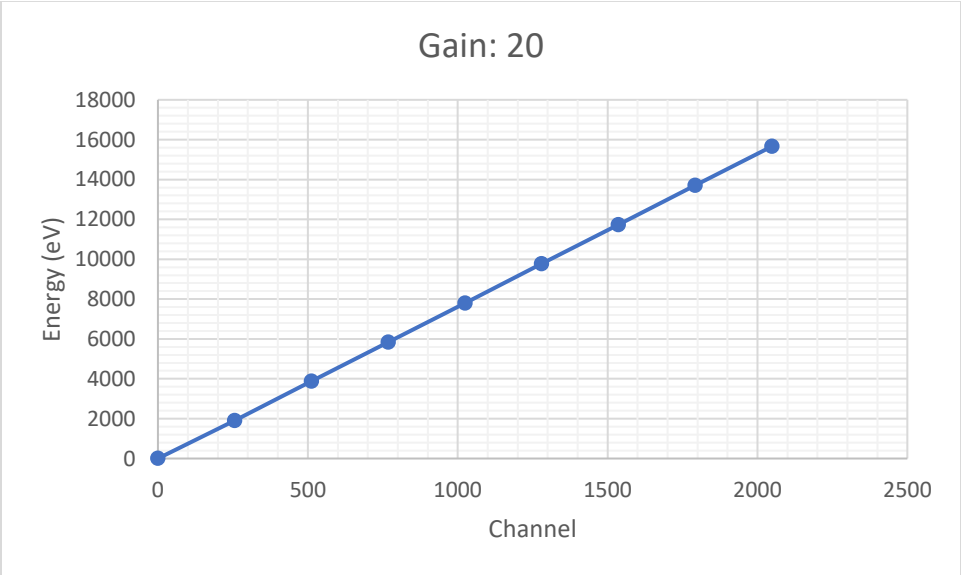
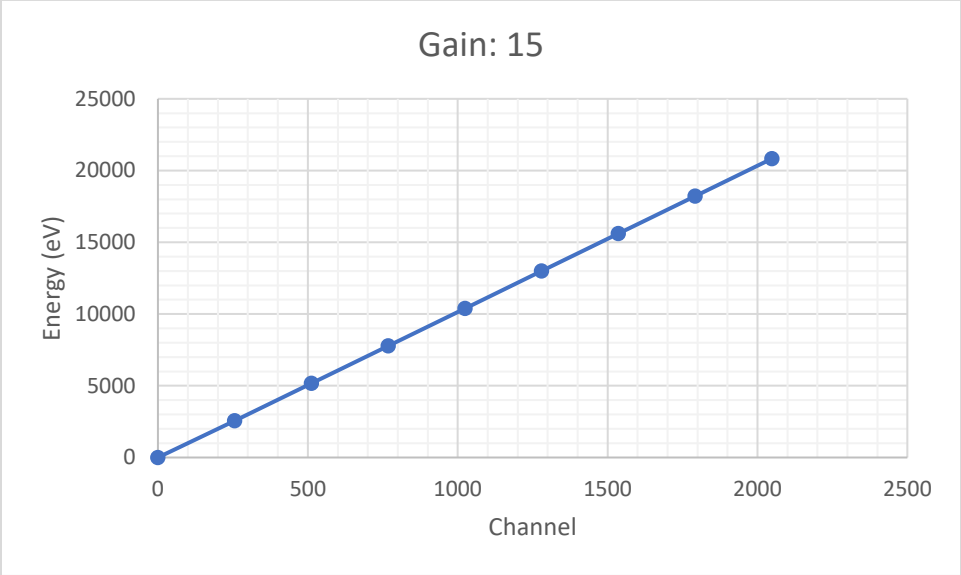
Figure (22) Block Diagram of the detector the preamplifier and the digital pulse processor [65].

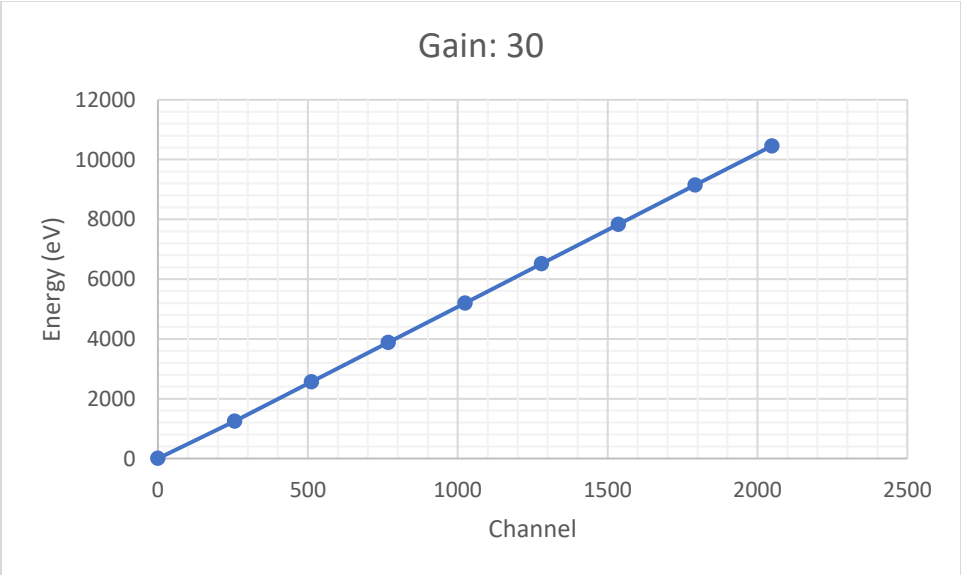
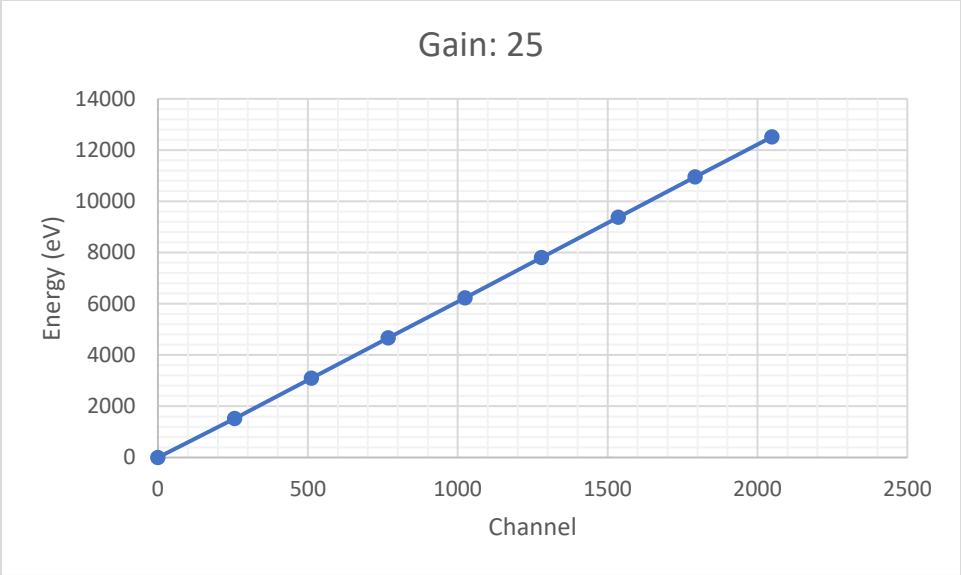
2.3.7. Energy Calibration

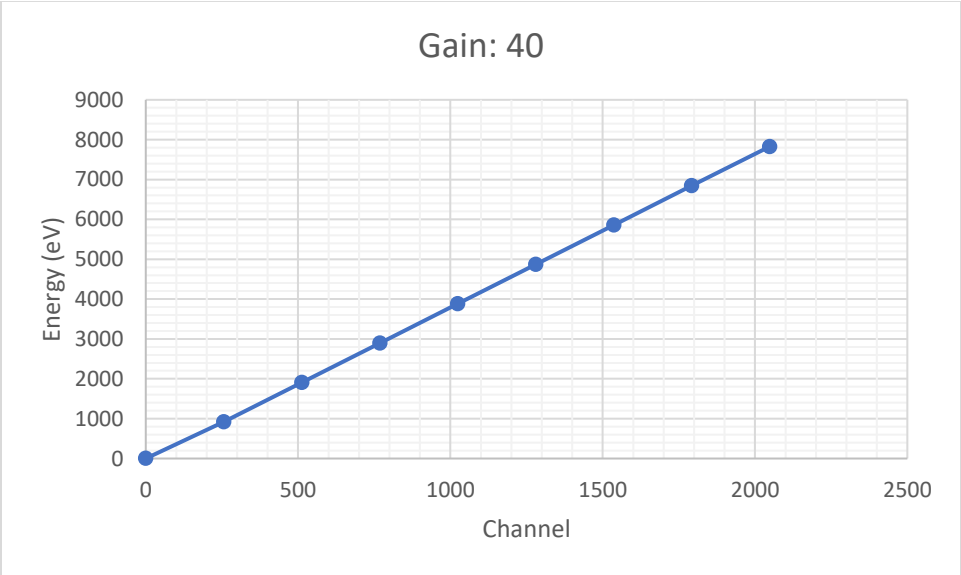
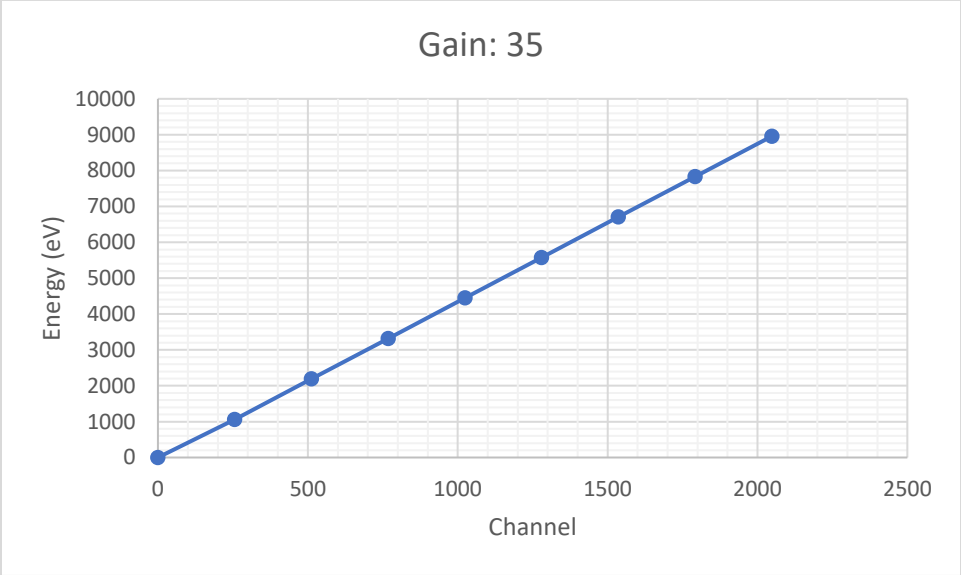
Energy calibration is the most common task when readying the PX5 for data acquisition. Energy calibration involves changing the gain with the DPPMCA software. Gain settings determine the full-scale energy range of the spectra. Even though most high energy x-rays will not be caught by the thin SDD, and it is rare to see them in the statistics, the gain should be set to include all possible x-ray peaks in the energy spectrum; failing to do so can negatively affect dead time. For high energy x-rays to appear in the spectra, longer run times are required, as the probability for attenuation inside the SDD increases with time.

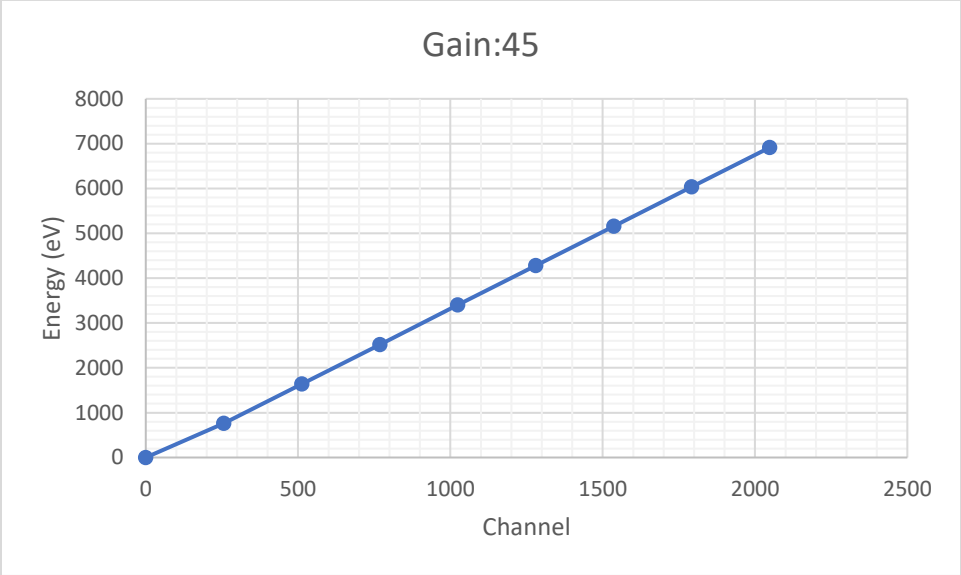
The energy range can be determined by taking an initial spectrum of a known substance, assign certain peaks their known energies, then use the software to calibrate. This will determine the energy range and will provide information that can aid in making gain adjustments. After tuning the gain for the desired energy scale the thresholds should be adjusted – it is advisable to update thresholds any time a parameter is altered. The following is the gain energy per channel data taken with ECU's Fast SDD.











2.3.5.2. Pulse Shaping

The Digital Pulse Processor identifies pulses by using thresholds. The DPP has parallel signal processing paths known as “slow” and “fast” channels, they both gather inbound pulse train data. The independent thresholds can be set for both the slow and fast channels. Optimal performance for the DPP depends greatly on proper slow and fast threshold settings. Thresholds should be set just above the noise in each channel. The fast channel will encounter more noise, so both thresholds should be different. The DPPMCA software provides an “Auto Tune” function to automatically set slow and fast thresholds. Thresholds should only be tuned when no x-rays are being emitted by a source; only background should be “seen” by the detector when setting thresholds. Thresholds should be reset any time a setting in DPPMCA software is changed. [66]

The pulse shaper’s main output is the peak values for each pulse permitted by the slow channel threshold. The slow channel threshold is used to distinguish pulses that should be included in the spectrum. The Digital Pulse Processor’s slow channel, with its relatively long time constant, acts as a low-level discriminator. All the events that are recorded in the spectrum are totaled with the slow channel counter. The channel determines accurate pulse heights; pulses having amplitudes below the slow channel threshold do not appear in the spectrum. In contrast to analog shapers, the DPP’s slow channel relies on trapezoidal pulse shaping. Trapezoidal shaping reduces pulse pile-up and electronic noise.

If the peaking time is short compared to the slow channel risetime (too long for a full charge collection), the accuracy of outgoing pulses will be adversely affected by

ballistic deficit. Pulses can also be totally dismissed if the threshold is set to high on the slow channel. [66]

Like the slow channel, the fast channel uses trapezoidal shaping, but the peaking time is much faster – approximately 0.1 to 0.4 μs . This means that the fast channel noise is typically higher. One of the fast channel's functions is to act as the "fast channel counter". The fast channel counter records and increments every incident where an x-ray exceeding the threshold is detected and increments the event in the input count. Another primary function of the fast channel is to activate pile-up rejection logic. Events in the slow channel that occur in a very short separation of time, or "pile-up", are indistinguishable by the slow channel. The fast channel identifies these peaks and serves to reject the pulses that pile-up. If pile-up rejection (PUR) logic is activated, and the threshold is set too low on the fast channel, every event will be rejected – no signal will appear.

The pile-up rejection and rise time discrimination logic serves to reject events that do not clear certain thresholds. If no pulses are being recorded, it is possible that the thresholds are improperly configured. The Rise Time Discrimination circuit should always be disabled for the purposes of ECU's PIXE system, but the Pile-up Rejection circuit should be enabled *after* all other system configurations have been set. PUR logic should always be activated while taking data with the PIXE system. [66]

The purpose of PUR circuitry is to identify events that occur faster than the pulse pair resolving time. This means pulses that occur so closely together in time that they appear as a single pulse with an invalid amplitude. If the electronics fail to see pulses

separated by less than the peaking time as two discrete events, pile-up logic will trigger. The symmetric trapezoidal pulse causes the pile-up interval, and the dead time, to be considerably faster relative to analog systems. The DPP calculates dead time and pile up rejection time intervals by summing the risetime and flat-top duration of the shaped pulse. X-rays that pile-up are not placed in the total count. [66]

Dead Time refers to the time interval that a series of pulses cannot be detected, and, therefore, are not included in the output count data. A higher count rate leads to a greater amount of dead time. Random pulses inevitably occur during the period of dead time, so the input count rate is always higher than the output count rate. Unlike analog multi-channel analyzers, The DPP encounters no dead time during peak acquisition, in addition to a significantly diminished dead time per pulse. Real time and accumulated time are both based on dead time. For example, if the real time reads 60 seconds, but the accumulated time reads 50 seconds, this means that 10 seconds worth of pulses were not counted; this would equate to a dead time value of approximately 17%. For good spectral data the dead time should be maintained below 50%. [66]

2.3.5.3. PX5 Electronics

The SDD's charge sensitive preamplifier has an output voltage signal that is proportional to the time integral of current – input charge. The output of the charge sensitive preamplifier provides input to the PX5. The PX5 input signal is prepared for digitization with the filtering and pulse shaping functions implemented by the prefilter. The prefilter uses a 3.2 μ s high pass filter to prevent pulse “ride up”, and it applies appropriate gain and DC offset to optimize the analog to digital converter resolution.

The output of the analog prefilter is digitized at 80 MHz by the 12-bit ADC, and then sent to the digital pulse shaper where the signal encounters the fast and slow parallel processing channels.

The multichannel analyzer (MCA) receives the digital input and detects the peak amplitude of the shaped pulses; If the pulse selection logic recognizes the pulse as legitimate the data is incremented in a memory location (channel) that corresponds with the peak amplitude. The MCA creates a histogram that contains the number events per channel (energy range). This is the energy spectra. The MCA accommodates 256-8192 channels. ECU's MCA is configured at 2048 channels.[67]

2.3.6 Detector Specifications and Construction

Amptek SDD detectors require negative HV (-135 V by default). The FAST SDD has a very high peak to background ratio – 26000/1. Set at a peaking time of 4 μ s the XR-100 FAST SDD housed in ECU's PIXE apparatus was benchmark tested with *Fe* – 55 to have a 131.8 eV full width half max (FWHM) resolution at the *Mn* 5.895 keV K_{α} line.

The detector was manufactured with a 12.5 μ m beryllium window, behind it is a 25 mm^2 active Silicon Drift Detector diode that has a thickness of 500 μ m. A multilayer collimator that uses a base metal of 100 μ m of tungsten (W). The subsequent layers of collimators consist of 35 μ m of chromium (Cr), 15 μ m of titanium (Ti), and 75 μ m of aluminum (Al), that collimate the active diode area to 17 mm^2 . The FAST SDD is

sensitive to magnetic fields, but the detector is far away from significant magnetic fields while housed in the target chamber. [67]

The XR-100 FAST SDD is fastened with two mounting holes onto an aluminum stand within the PIXE chamber. This not only allows for a correct positioning of the detector but securing the detector with the mounting holes increases the contact area of the FAST SDD, this creates a better heat sync for the detector while under vacuum. This allows the detector to run approximately 4-6 degrees cooler.

The PX5 is used to set the temperature control point of the 2-stage cooler. In calibration, it is suggested to set the cooler to maximum cooling, let it stabilize then set it two degrees above the minimum observed temperature, so no temperature variations occur during data acquisition.

The PX5 includes a digital pulse shaping amplifier and multichannel analyzer. It can sustain high count rates while maintaining outstanding baseline stability, throughput, and pile-up rejection. Peaking times can be selected from 0.05 to 102 μm . The multichannel analyzer can accommodate 256 to 8192 channels at 3 bytes, or 16.7 M counts, per channel. Acquisition time is adjustable from 10 ms to 466 days. The unit can be preset to measure time, total counts, counts in a region of interest (ROI), or counts in a channel. The PX5 uses a Silicon Labs 8051F340 8051 microprocessor with 512 kb SRAM external memory, the unit is controlled by Amptek DPPMCA display and acquisition software. This software fully configures, controls, downloads, and displays spectral data [68].

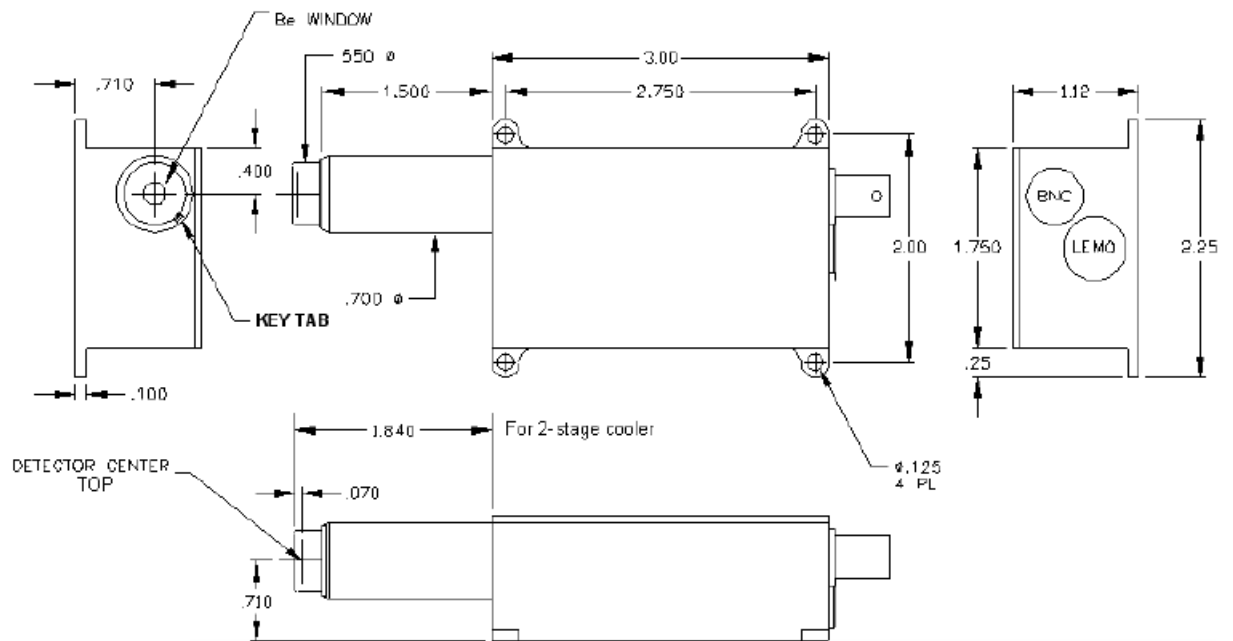


Figure (23). Fast SDD Dimensions (units in inches)



Figure (24). Photograph of the XR-100 Fast SDD detector

2.3.7 Data Display and Analysis

The spectrum, counts, and accumulation time are automatically displayed as data are acquired. If a region of interest is defined and selected, its net area and other properties are also shown. To zoom in on a portion of the spectrum, use the arrows at lower right. To return to the full screen view, use the full range arrows on the toolbar.

To toggle between a linear and logarithmic vertical scale click on the spectrum and press “L” on the keyboard or select the scale from the Display menu. The primary data from the SDD are the spectrum and the count rates. To toggle between channel number and energy press F7.

A region of interest, or ROI, is an area marked as a potential peak in a spectrum. To select a ROI. Place the cursor at the left edge (lowest channel) of desired region and then press and hold the “U” key until the peak is highlighted and the upper edge is reached. You can also select the right side of the peak and select to the left by pressing the “Y” key.

For each ROI, DPPMCA computes the total counts (gross area), subtracts the background, and with the difference computes the net area, centroid, peak width, and FWHM resolution.

2.3.8 Electrical and Software Interfaces

There are three main elements to the electrical interface: communications, power, and auxiliary. The communications interfaces are the primary means to control the PX5 and to acquire the data. The PX5 supports a USB interface. With all three interfaces, commands are issued to set the many configuration parameters. The unit sends three classes of data packets back to the computer: status packets (which include the counter outputs), Spectral data packets (which contain the MCA output array), and oscilloscope packets.

DPPMCA software provides the quickest way to control and readout the PX5. It provides access to all the configuration parameters in the DPP, lets one start and stop data acquisition, reads and displays the data, performs very simple analysis, and saves the data in an ASCII format. The files saved by DPPMCA can be read by many spectral processing software packages including GUPIX.

2.3.9 System Gain

The system gain is used to assign channel numbers certain energy designations. The gain is stated in units of channels/keV, and it gives the MCA channel number a designation for certain energy peaks. The gain consists of the product of the conversion gain of the MCA (*channels/mV*), the total gain of the voltage amplifier, and the conversion gain of charge sensitive preamplifier (*mV/keV*). The preamp conversion gain is approximately 1 mV/keV , while the MCA's conversion gain is the number of channels (say, 2048) divided by the corresponding peak channel voltage ($\sim 950 \text{ mV}$), while the

digital pulse processor gain is the product of the coarse and fine gains. However, these values are simply estimates and the actual gain can fluctuate by a few percent. These approximations are good for find a starting point for initial calibration, but every detector will have a different energy scale per gain as they are dominated by the engineering tolerances of the individual electrical components found within the system. Therefore, every detector should be calibrated by the operator [69].

Gain	eV/channel	Full Scale Energy (eV)
5	30.77944336	63036.3
7.5	20.39575195	41770.5
10	15.31064453	31356.2
15	10.16967773	20827.5
20	7.646972656	15661
25	6.108642578	12510.5
30	5.10546875	10456
35	4.3734375	8956.8
40	3.821972656	7827.4
45	3.375952148	6913.95
46.5	3.266918945	6690.65

Table (6). Gain adjusted parameters

2.3.10 Standard Operating Procedure

The following section highlights methods used for gathering spectral data with ECU's PIXE system.

PIXE samples are prepared and mounted inside the 24-position sample carousel. One space is left open, so accurate current readings may be taken by the Faraday cup

located at the back of the target chamber. A blank position in the filter wheel allows for unattenuated x-ray collection. After the steel retaining rings for both the sample and filter wheels are replaced, they are mounted inside the chamber.

The chamber pressure is optimal for PIXE analysis at 10^{-6} Torr ($10^{-3} - 10^{-4}$ Pa), so the seal associated with the chamber lid is thoroughly cleaned. The track running around the top of the chamber is cleaned with alcohol to rid rough spots left from vacuum grease and particulates that may allow air to pass through into the evacuated chamber. The O-ring for the lid is cleaned with alcohol then lightly lubricated with high vacuum grease. After the O-ring is laid in the track, the lid is cleaned with alcohol and placed on top of the chamber.

The pressure valve on the side of the chamber is closed, and the collimator and fore-line valves are opened, the roughing pump is activated. Pumping the chamber down to 10^{-3} Torr takes ~ 10 min. The turbomolecular pump is turned on after the chamber is down to rough vacuum. After the chamber is at the desired vacuum, beam is placed in the Faraday cup at the back of the PIXE chamber.

The CCD Camera is used by the “EZ Grabber software” and is useful when controlling motors and lining up samples. To initiate the Lab View motor control software the following steps are taken in sequence: the USB X-Series Multifunction DAC is turned on, the motor control module is turned on, then the Lab View software is opened. The motors will not operate if initiated out of sequence. Once control of the motors is established, the filter and sample wheels are adjusted to their blank positions. After opening the gate valve to PIXE line (L45). Ion beam can enter the Faraday cup in the

back of the chamber. After adjusting source and accelerator parameters for the desired experimental current, the PX5 Digital Pulse Processor is turned on.

If the PX5 power button is pressed quickly, a single chirp will be heard, and the detection parameters will go to the factory default settings. If the power button is held in, a multiple chirp will be heard, and the PX5 will be adjusted to the settings of its last use. The DPPMCA software is opened and connected to the PX5 Digital Pulse Processor. If the software is opened before the PX5 is turned on, there will be no connection established with the PX5 or XR-100 Fast SDD detector.

Acquisition parameters are chosen with the MCA tab or the acquisition setup button. This is where acquisition time, preset count, and number of channels can be set. The PX5 can be set to stop acquisition after a fixed time, after a fixed number of counts are collected, or both. It is recommended to keep the channels set to 2048 or 1024, as GUPIX can only accommodate 2048 channels. Under the shaping tab, peaking time can be adjusted (the noise corner for ECU's detector is $4.0 \mu\text{s}$). Pile-up Rejection (PUR) should be turned off until all adjustments are made. The baseline reduction (BLR) mode is set at 1, with 3 down and 1 up, or with 3 down 0 up (the latter is factory recommended). Clock speed is set to 80 MHz. The desired gain and cooler temperature ($\sim 210 \text{ K}$) is adjusted along with the high voltage bias (-135 V).

To start background adjustments, data acquisition ("traffic-light" button) begins with the beam only striking the Faraday cup. If there is an X ray source it is removed. After a few seconds the "tune slow/fast thresholds" button is clicked, and the system is

ready for data acquisition. After power is applied, or after a configuration change, it can take minutes for an Amptek detector to stabilize.

If the spectrum looks odd, clear the data and restart. You can tell that data are being acquired if (a) the spectrum appears in the window, (b) the input and total counts are increasing (c) the accumulation time is increasing, and (d) the “status” in the right-hand info panel reads “acquiring.”

2.3.10.1 Energy/Channel Calibration

After data acquisition of a known material, the cursor is placed to the leftmost edge of a known peak and the ROI is marked. An ROI is made with another known energy peak, and a third if applicable. The “calibrate” button is selected, and the cursor is placed on the first energy peak. The “centroid” button in the calibration dialogue box is selected and the centroid number appears in the channel box. A known energy associated with the peak is entered in the value box to the right of the channel box then added to the list of ROIs. This process is repeated with at least one other peak, for a minimum of two ROIs. Click “Ok”. The gain specific energy range is calibrated, and the system is ready for materials analysis.

3. Results

3.1 Target Chamber Results

The target chamber is made of materials that interfere very little, if at all, with the PIXE analysis process. It is also constructed to withstand high pressure differentials. The chamber typically reaches a vacuum of magnitude of 10^{-6} Torr within 12 hours of beginning evacuation with the turbomolecular pump. Successful PIXE analysis can be performed at this pressure. A magnitude of 10^{-7} Torr is usually reached within six days. Failure to reach these pressures in these times, may indicate an air leak in the chamber.

The sample and filter wheels are operationally functional. The sample wheel moves in both directions of rotation like the sample wheel, and the translational motion of the sample wheel allows for the beam to be placed anywhere on a given target position on the sample wheel. All the motors housed within the chamber are successfully operational with the use of the customized Lab View PIXE motor control software. Additionally, the pneumatic valves that control the faraday cup and fore-line valve are both operational,

The drift lines and chamber are in very good alignment, and proton beam with currents as high as 160 nA have been measured with the Faraday cup located in the back of the PIXE chamber. Successful PIXE analysis only requires 1 nA of beam current.

Accurate materials analysis has been performed with East Carolina University's Particle Induced X-Ray Emission system.

3.2 Fe 55 data

For initial energy calibration, a Fe-55 x-ray source was used to generate control data. The x-ray energies produced from $Mn_{K\alpha 1}$ (5.985 keV), $Mn_{K\alpha 2}$ (6.49 keV) transitions were known and the energy spectrum was calibrated expecting that the visible peaks were those manganese peaks. The gain was set to allow for a larger energy range, and the Fe-55 energy calibration was verified with a Cs-137 source that emitted (31.81 Ba Ka2 and 36.38 Ba Kb1).

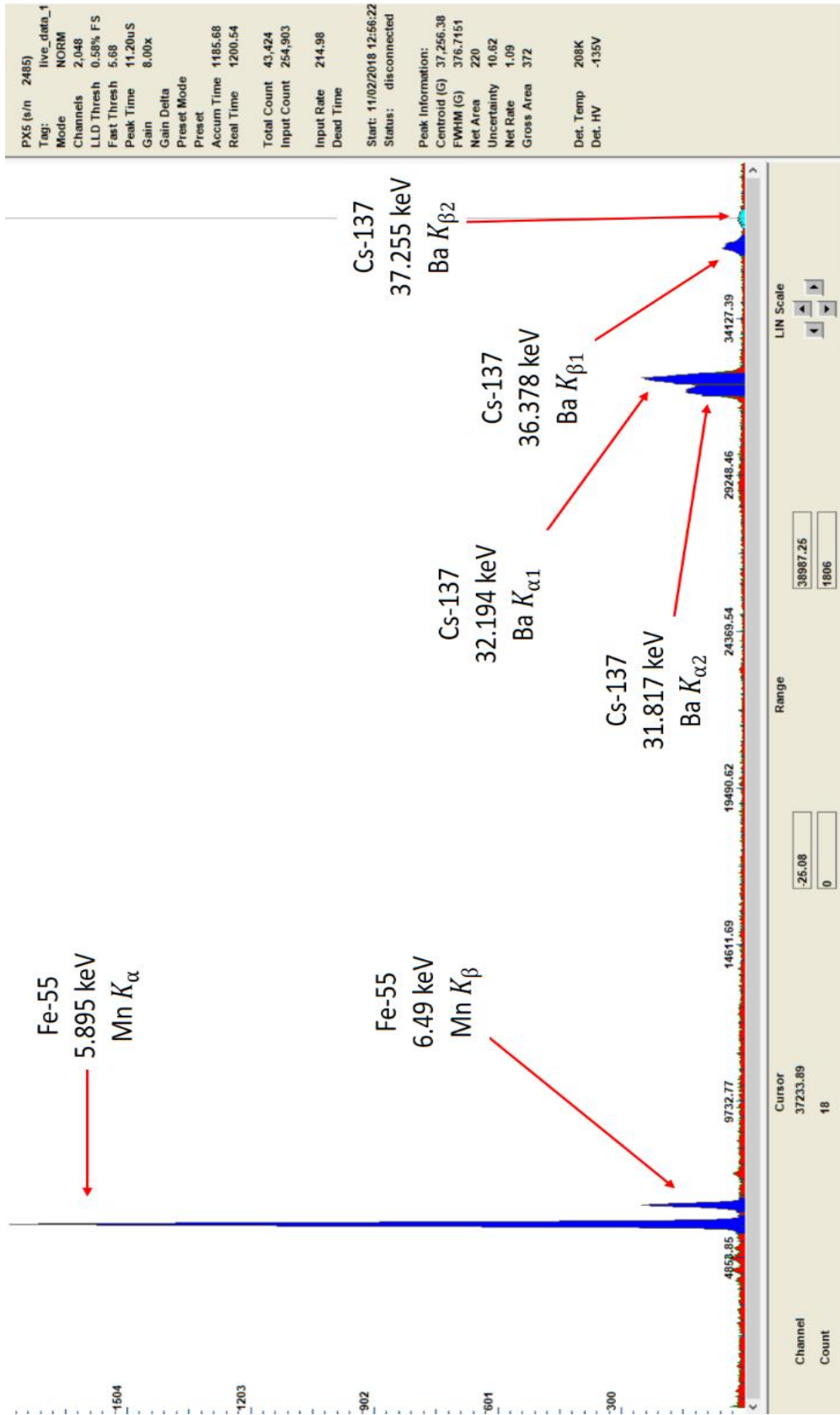


Figure (25). Iron-55 and Cesium-137 Energy Calibration Data

Gain settings change the spectral energy scale. Using Fe-55, the full-scale energy range was compared to gain settings. Although it is not probable that a high energy x-ray will be completely attenuated in the Silicon diode, it has been suggested to set the energy scale to accommodate those energies; neglecting to do so may increase dead time.

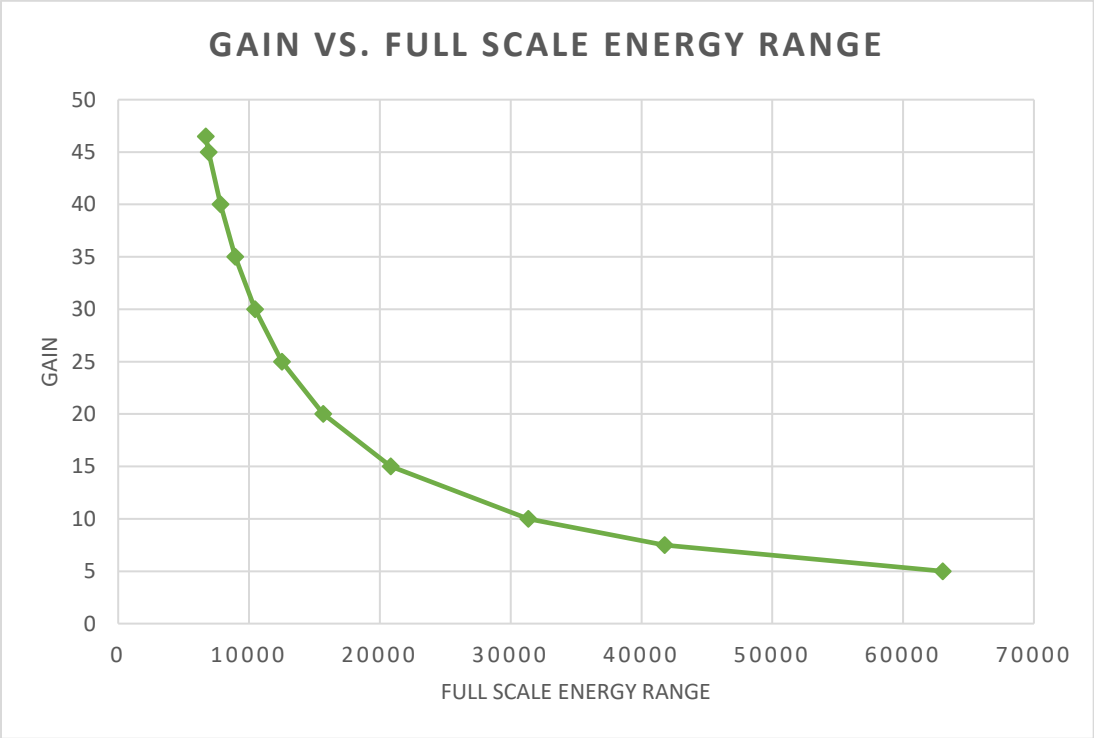


Figure (26). Gain vs. Full Scale energy range

Figure (27). Fe-55, Gain 5 (top). Figure (28). Fe-55, Gain 10 (bottom).

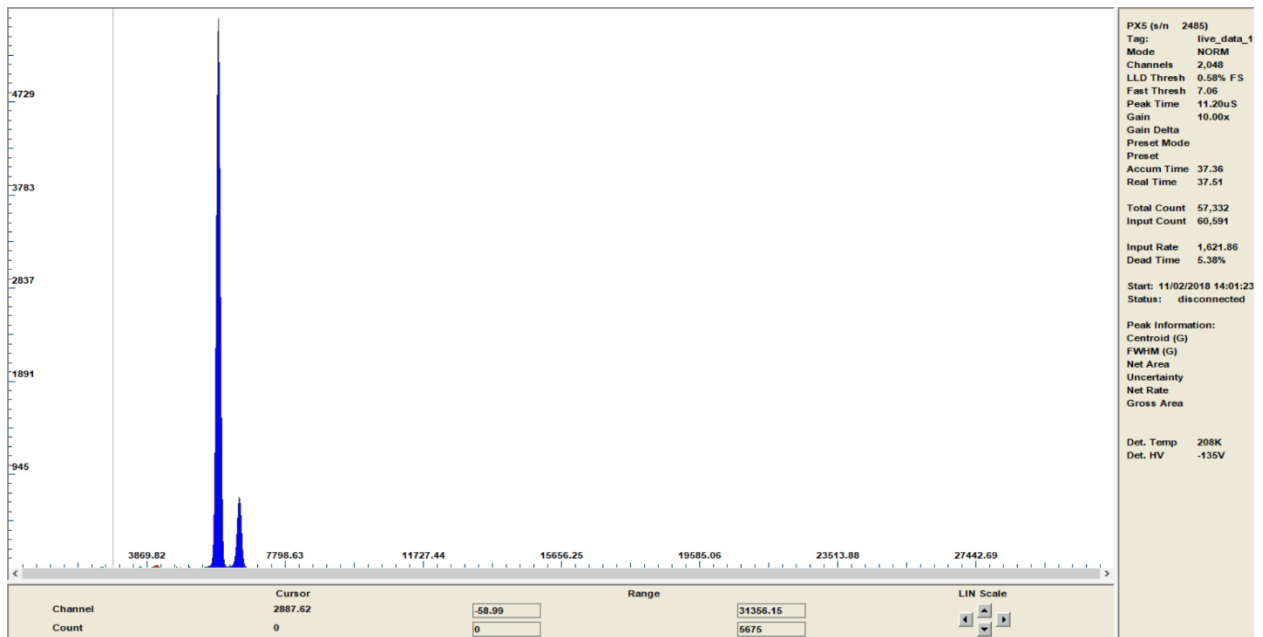
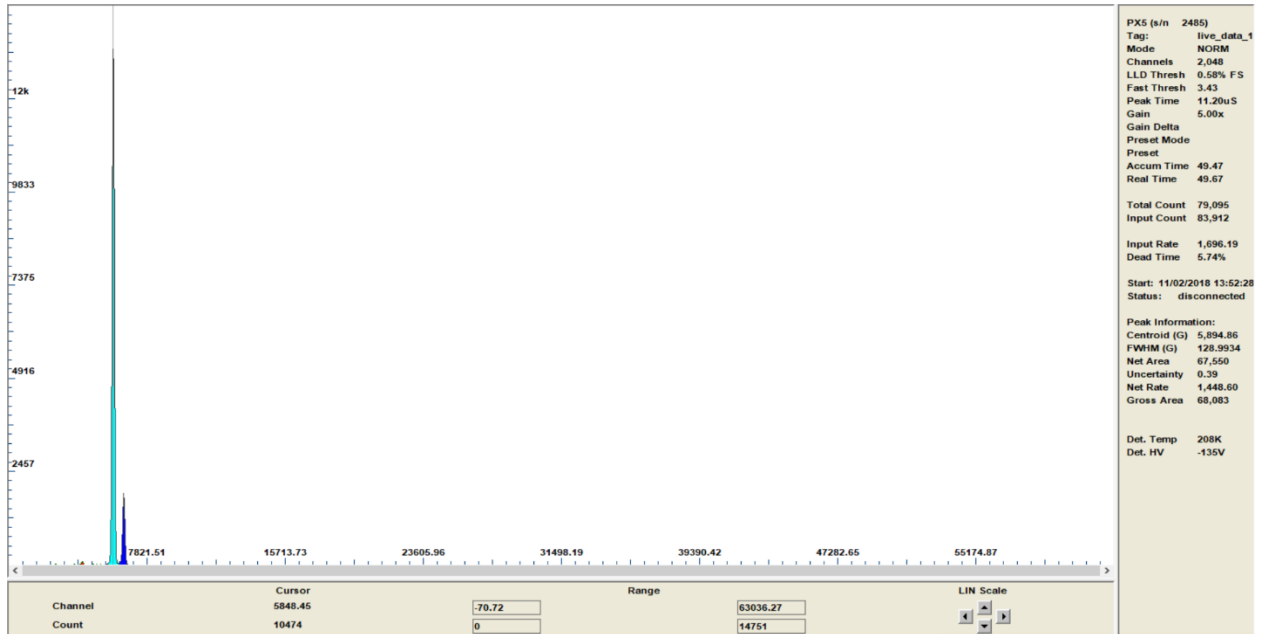


Figure (29). Fe-55, Gain 15 (top). Figure (30). Fe-55, Gain 20 (bottom).

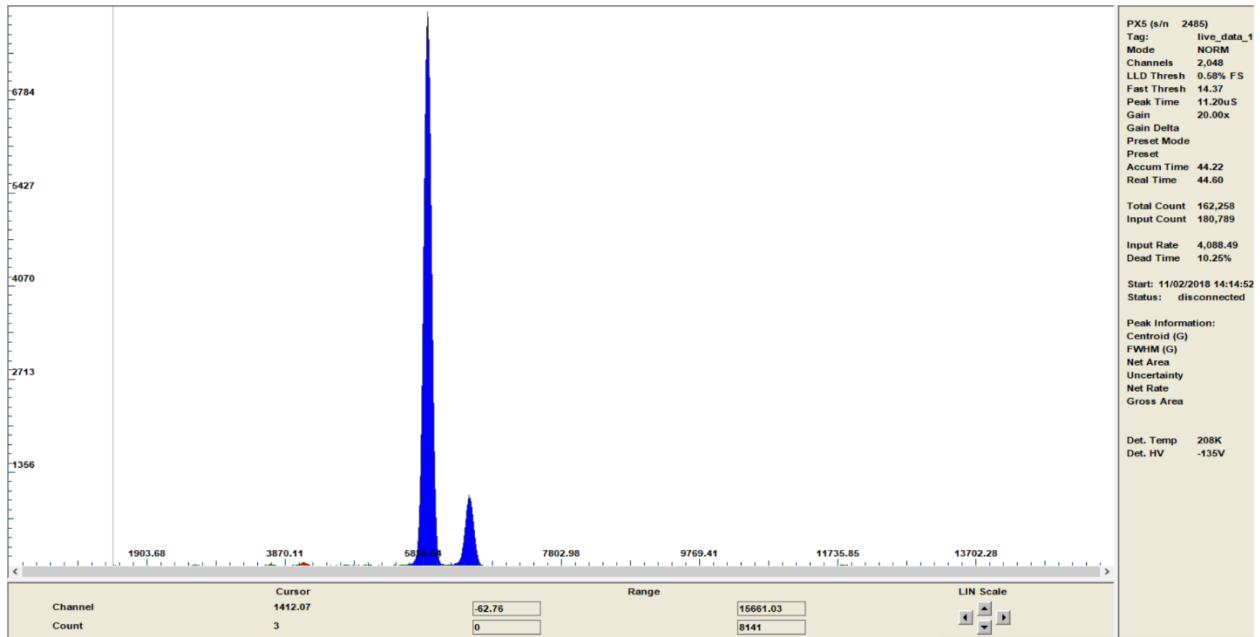
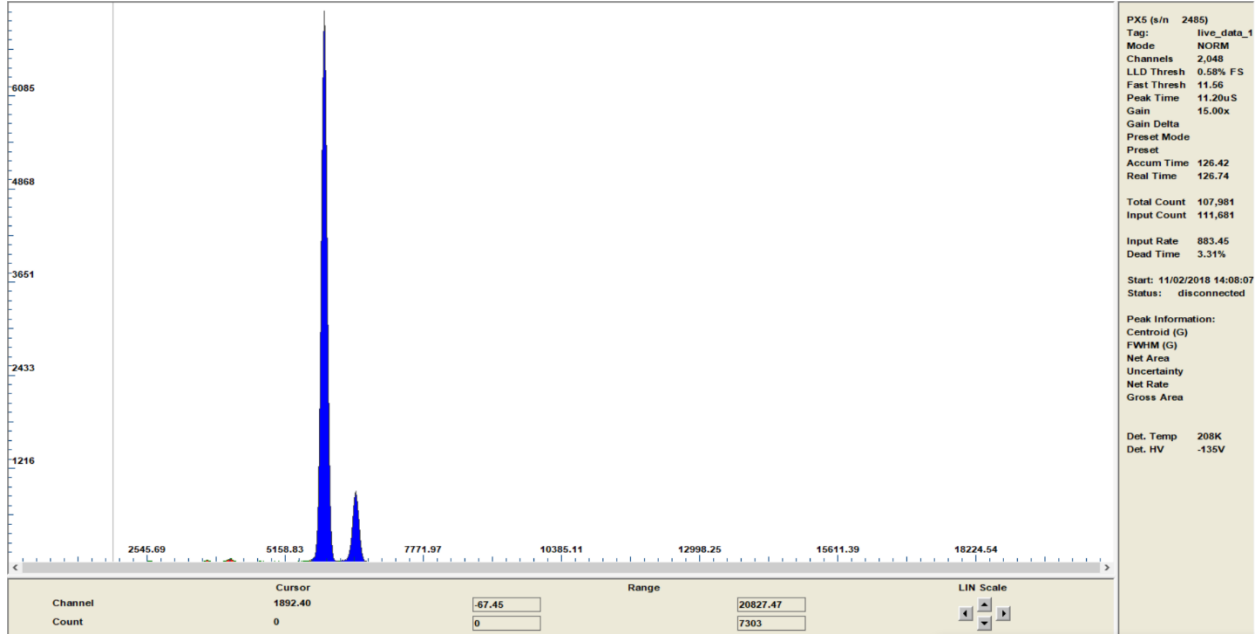


Figure (31). Fe-55, Gain 25 (top). Figure (32). Fe-55, Gain 30 (bottom).

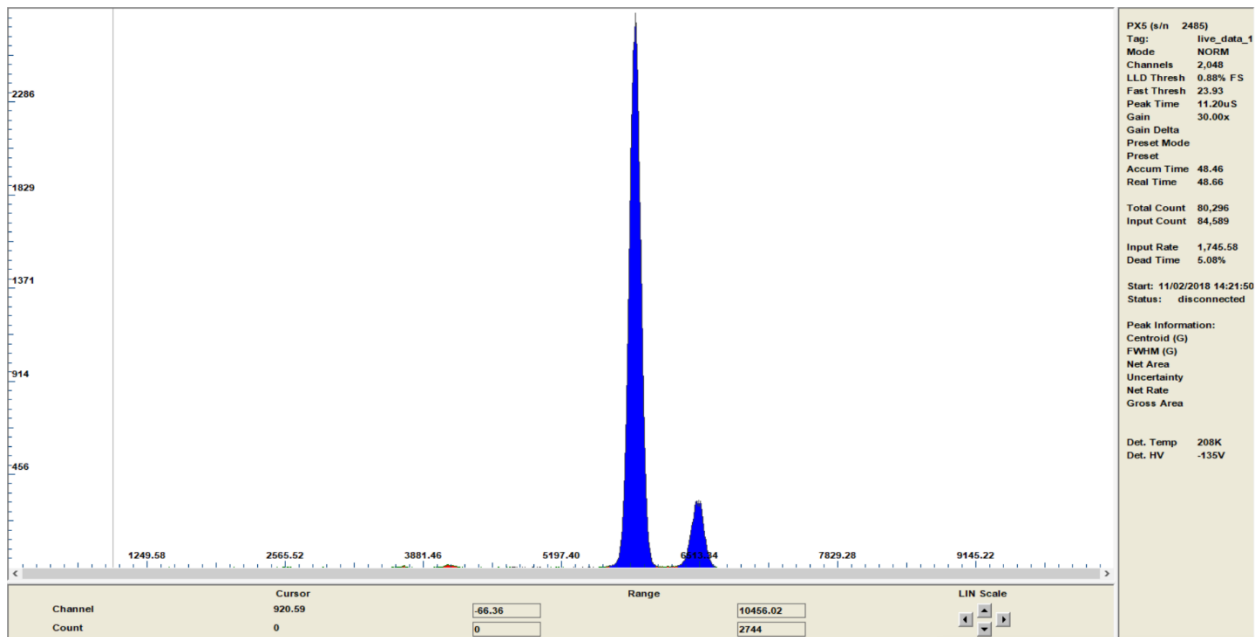
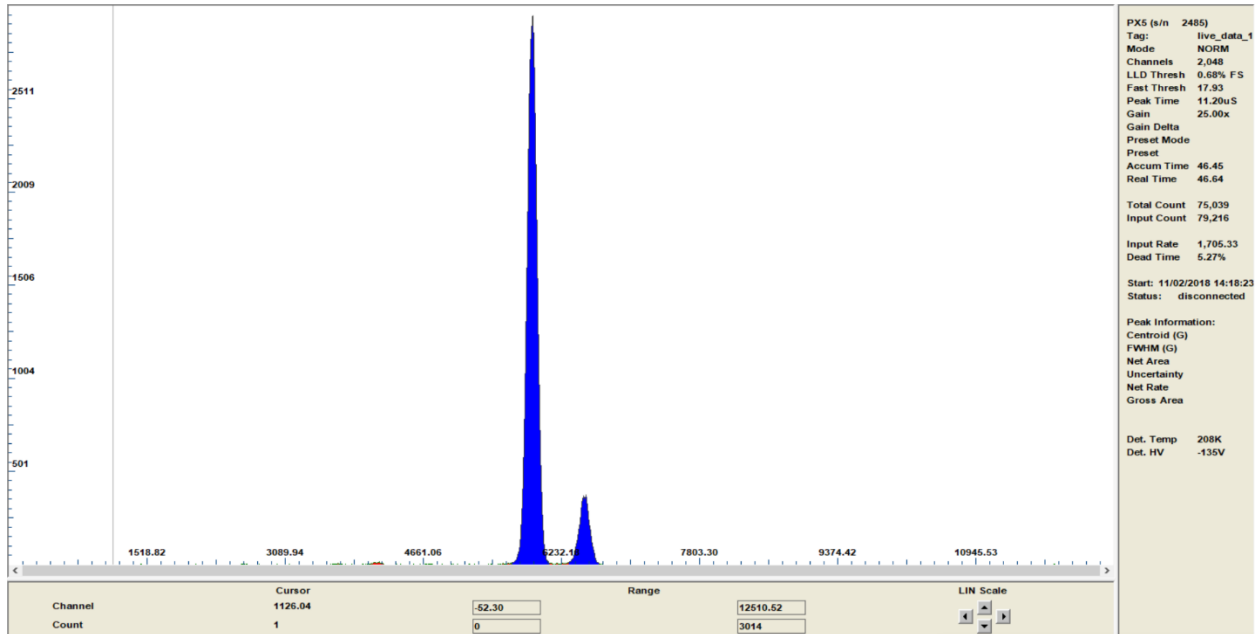


Figure (33). Fe-55, Gain 35 (top). Figure (34). Fe-55, Gain 45 (bottom).

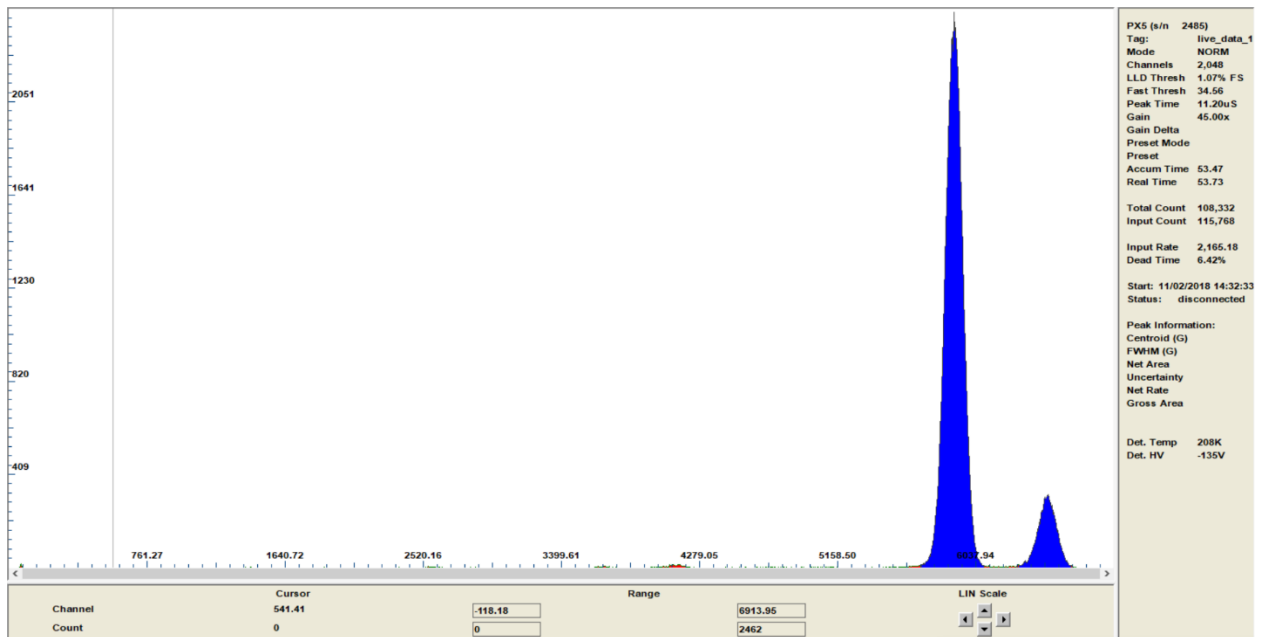
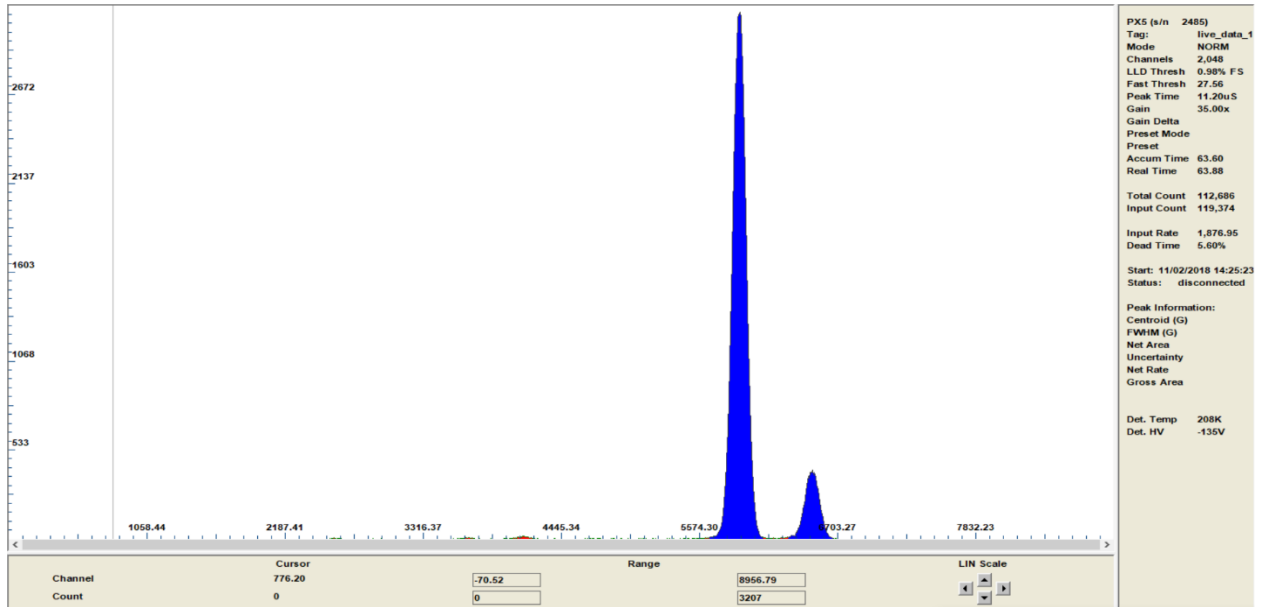
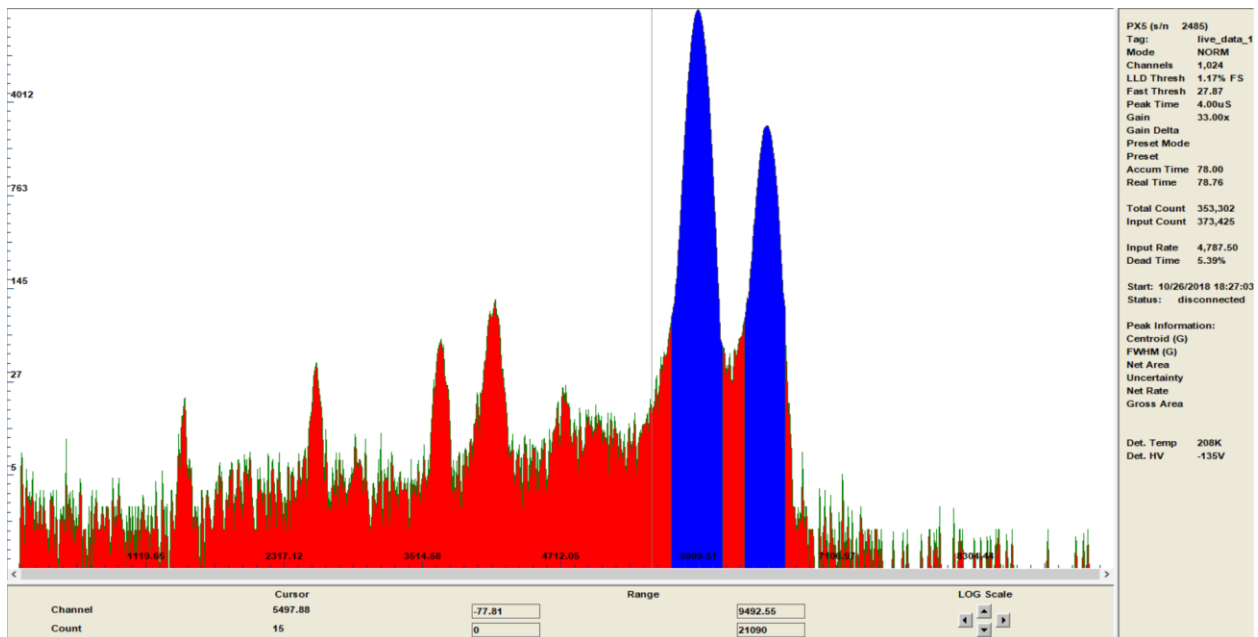
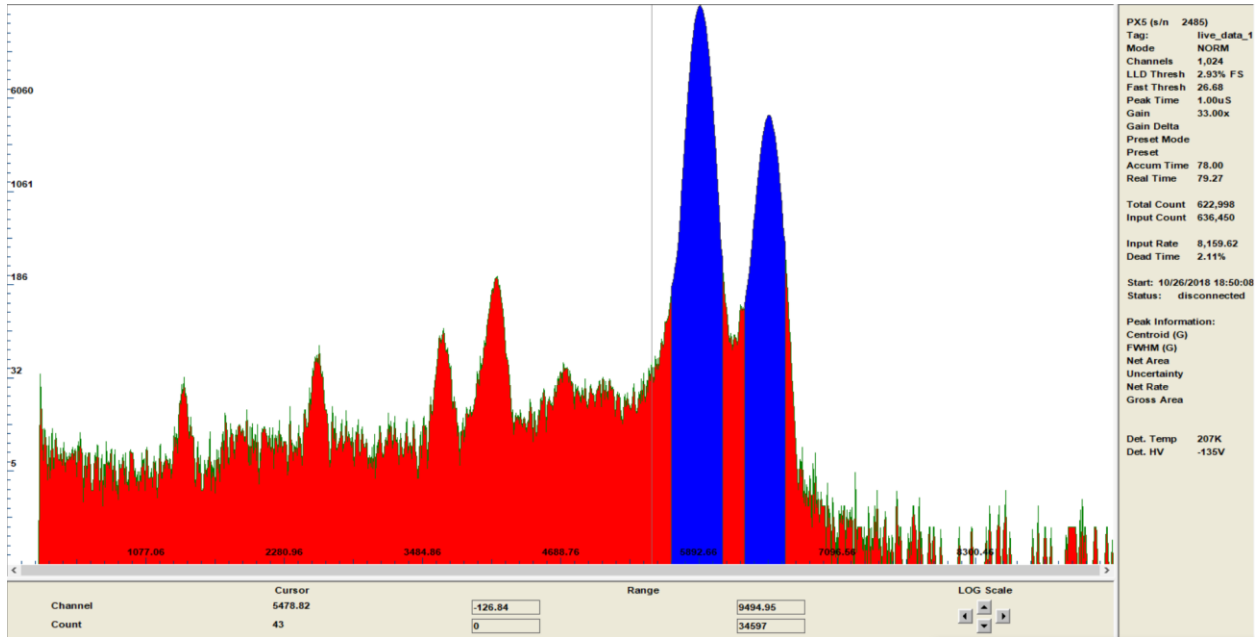


Table (7). Gain – eV/channel.

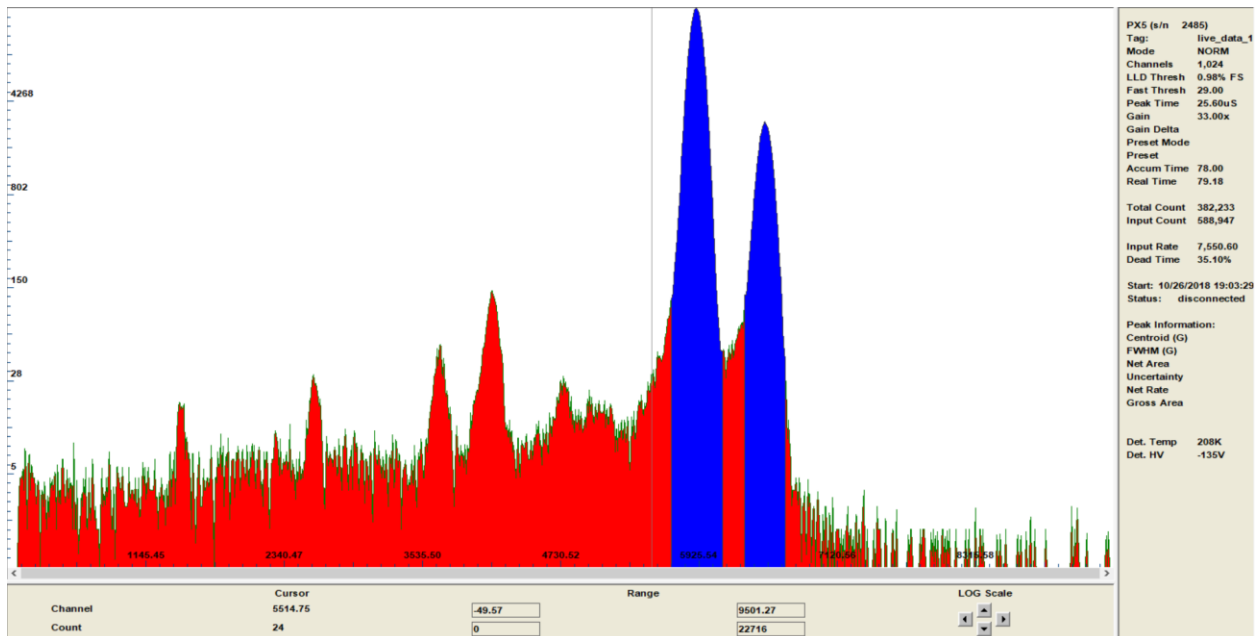
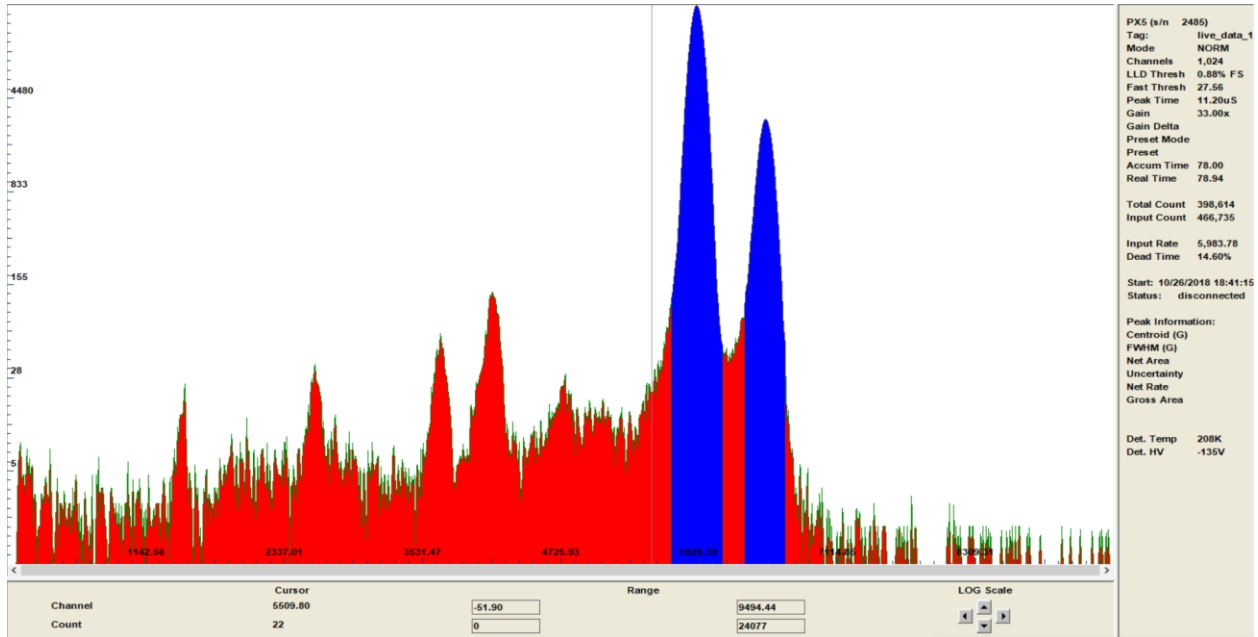
Gain	eV/channel	Full Scale Energy (eV)
5	30.77944336	63036.3
7.5	20.39575195	41770.5
10	15.31064453	31356.2
15	10.16967773	20827.5
20	7.646972656	15661
25	6.108642578	12510.5
30	5.10546875	10456
35	4.3734375	8956.8
40	3.821972656	7827.4
45	3.375952148	6913.95
46.5	3.266918945	6690.65

An increase in peaking time causes an increase in parallel noise, but a decrease in series noise. Pink, or $\frac{1}{f}$, noise is independent of peaking time. This means that there is a time where noise is at its least – the noise corner. The data was taken with peaking times ranging from 1 – 25.6 μs , and it showed that the least amount of noise was found at 4 μs when taking Fe-55 data.

The following Fe-55 spectrum is peaking time to noise data, the figures are (36) top and (37) bottom.



The following Fe-55 spectrum is peaking time to noise data, the figures are (38) top and (39) bottom.



The last Fe-55 data was taken to relate count rate to the dead time of the detector, this data was taken with a peaking time of 11.2 μs and at 78s of acquisition time. The data shows that the highest resolution can be obtained with lower count rates and lower dead times. To get defined peaks, however, the data accumulation time should to be longer. The Fe-55 source was weak and as close as possible to the detector, so a higher count rate could not be achieved, but the data shows that a count rate below 10000 cps keeps the resolution below 2.2%.

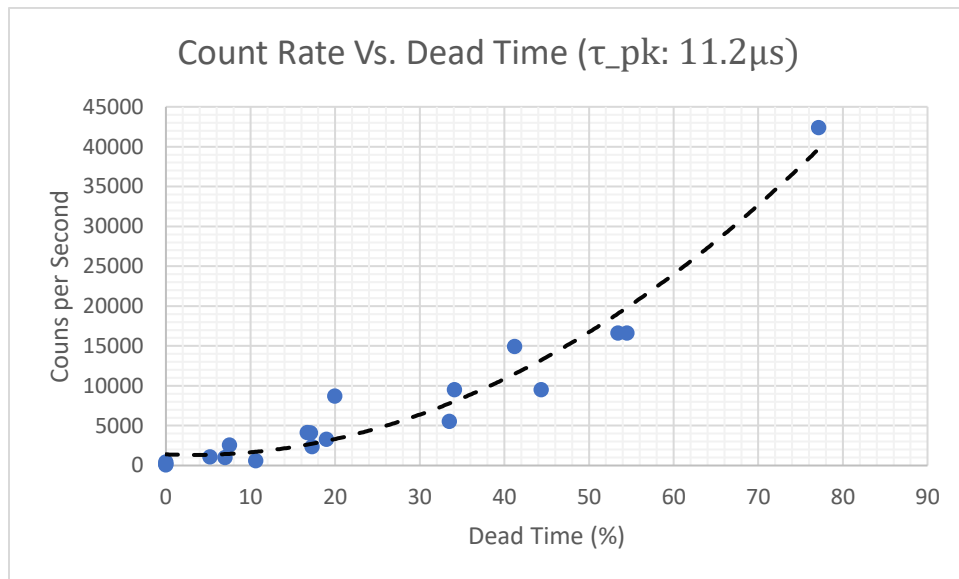


Figure (40). Count Rate Vs. Dead Time (peak time 11.2 μs).

3.3 PIXE Spectral Data

During this calibration, Au ($Z=79$) was used as the standard at which all other spectral data was taken. The gold that was used was a thin foil and was 99.9% pure. All the data was run at 2-2.6 $n\text{A}$ and 12 $n\text{A}$ at 2 MeV, and at 3 MeV with 1nA of current.

During test runs, the gain was set to 10 (~31 keV full scale) to accommodate the x-ray energies emitted by the other target elements used in the trial.

Figure (41) Gold x-ray spectra at 2 MeV with a current of 2.5 nA

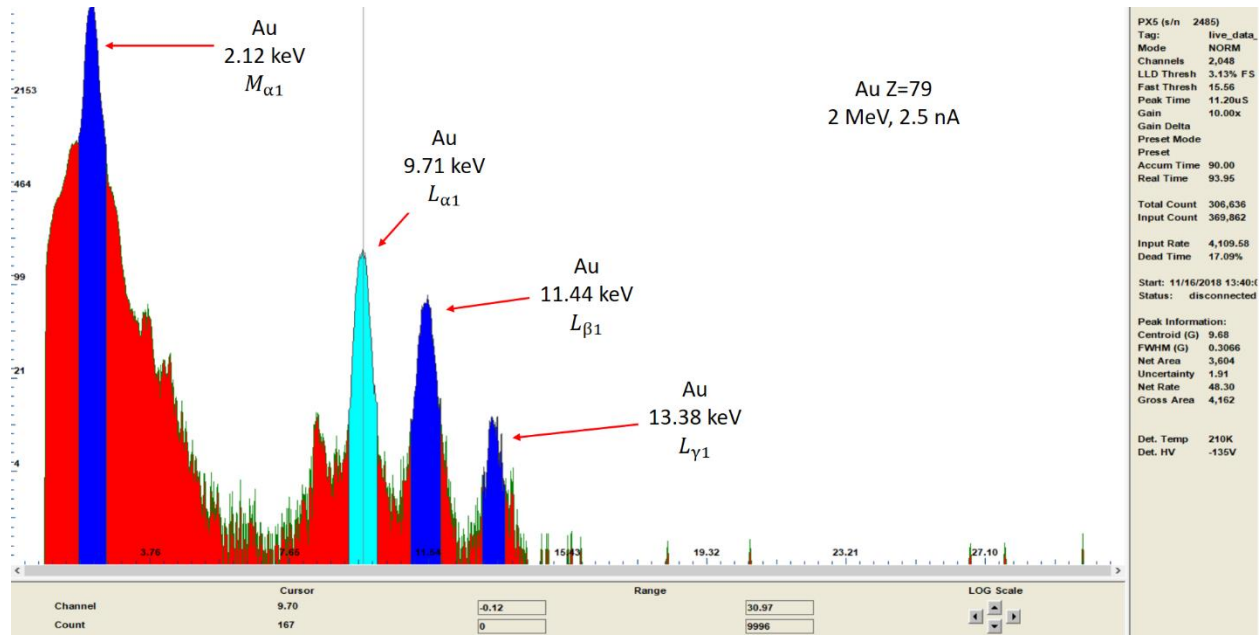
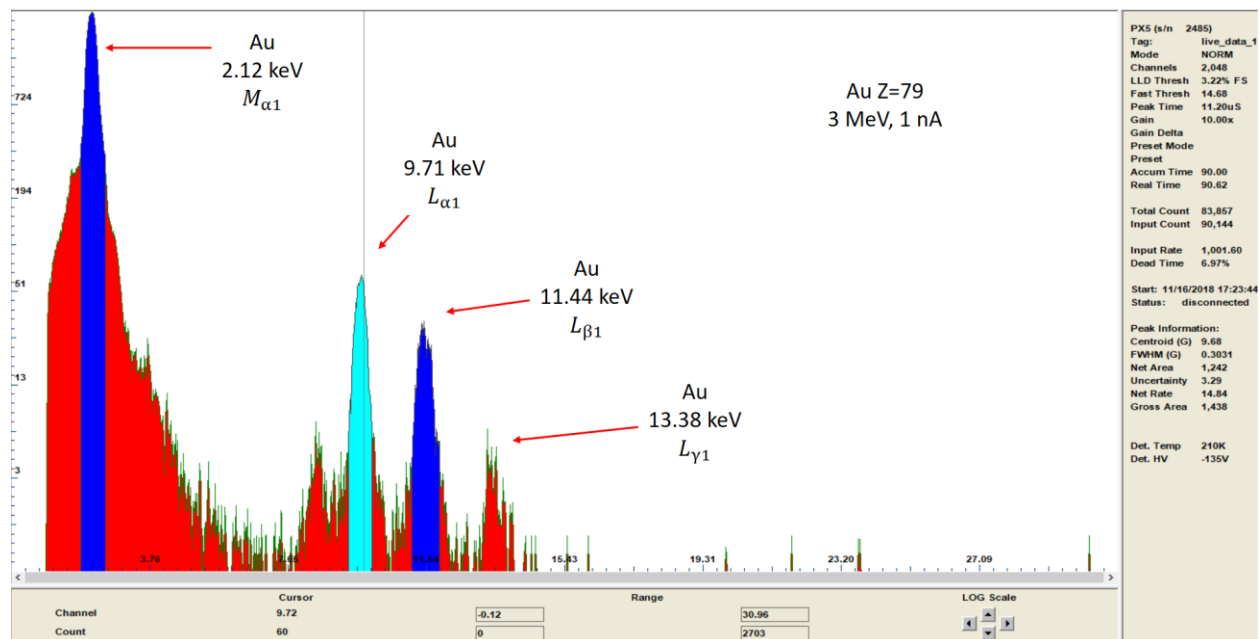
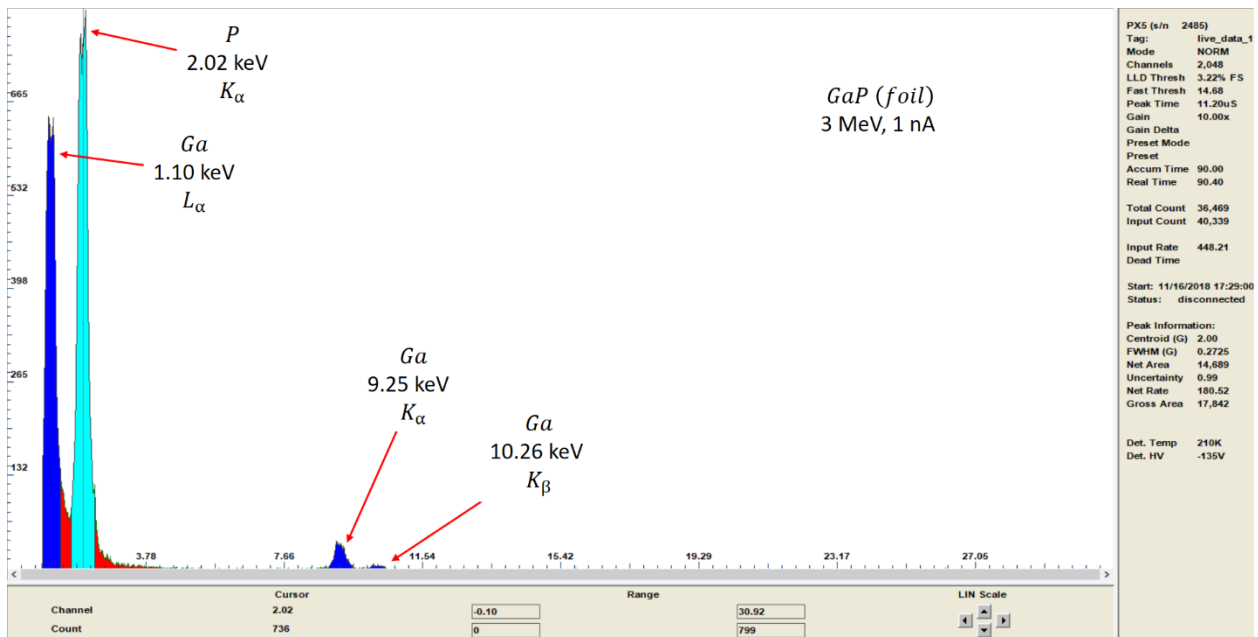
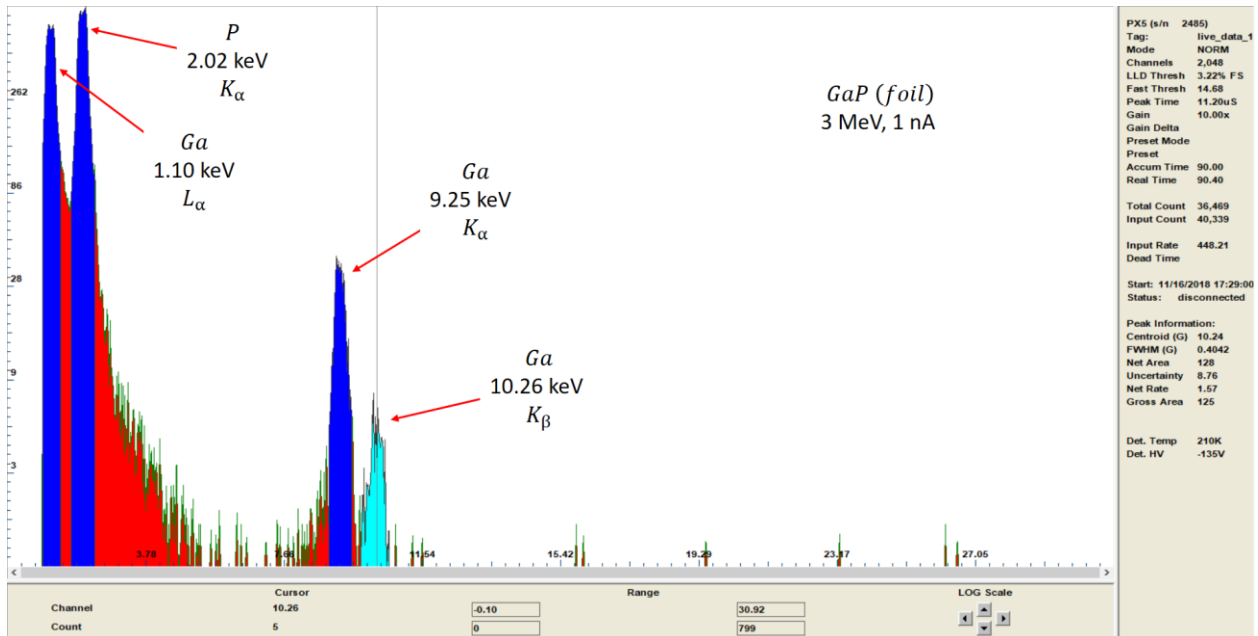


Figure (42). Gold x-ray spectra at 3 MeV with a current of 1 nA



With all three beam settings, specific test elements were accurately identified based on their x-ray spectral lines. Additionally, the energy scale provided with the gold calibration agreed with the peaks produced by all the test elements. Through all three run parameters, simultaneous multi-elemental analysis was verified using a *GaP* (Gallium Phosphide) foil and a thick disk of $YBa_2Cu_2O_7$.

Figures (43) and (44) Gallium Phosphide x-ray spectra at 3 MeV with a current of 1 nA



Figures (45) and (46) superconductor x-ray spectra at 2 MeV with a current of 2.1 nA

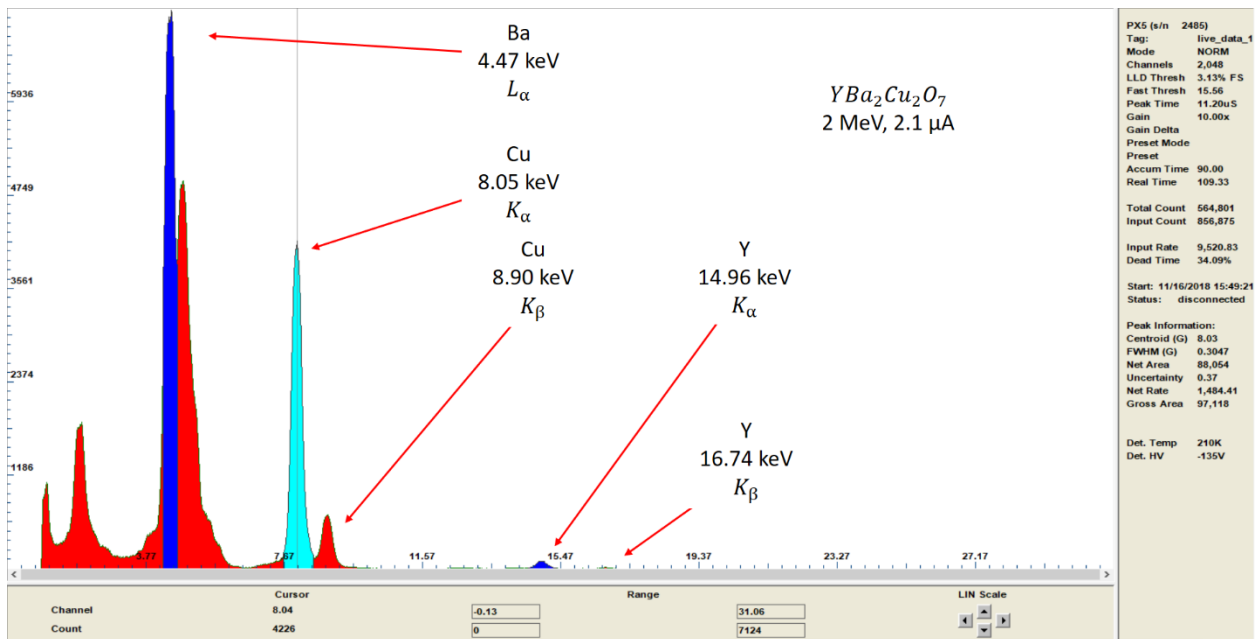
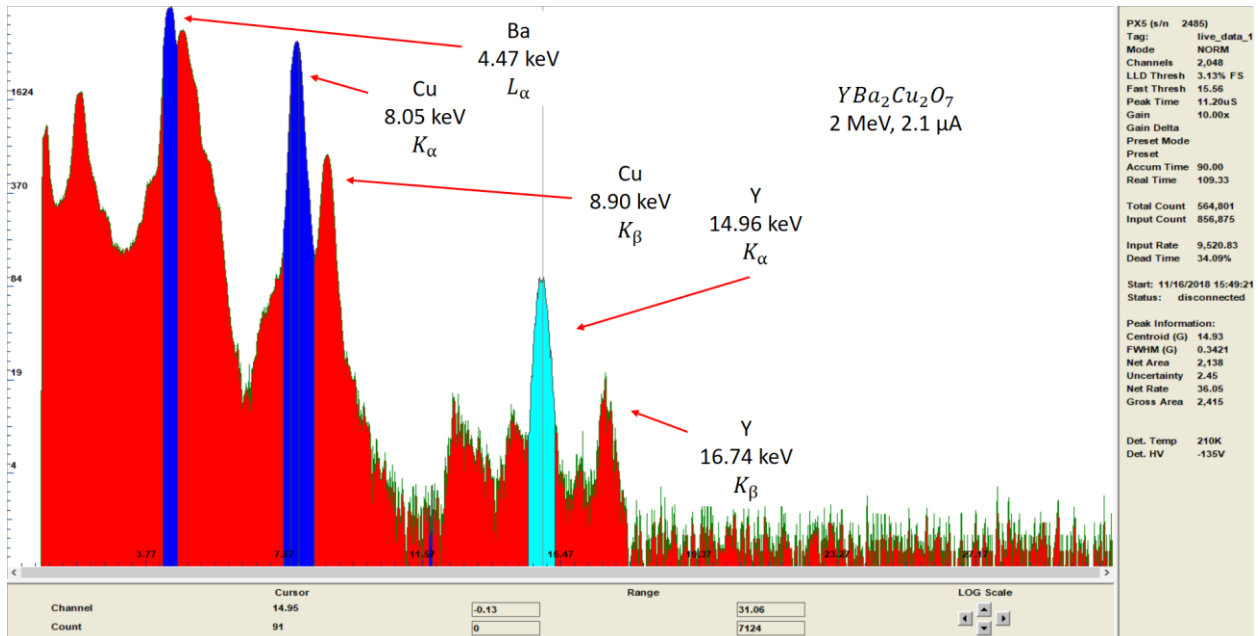
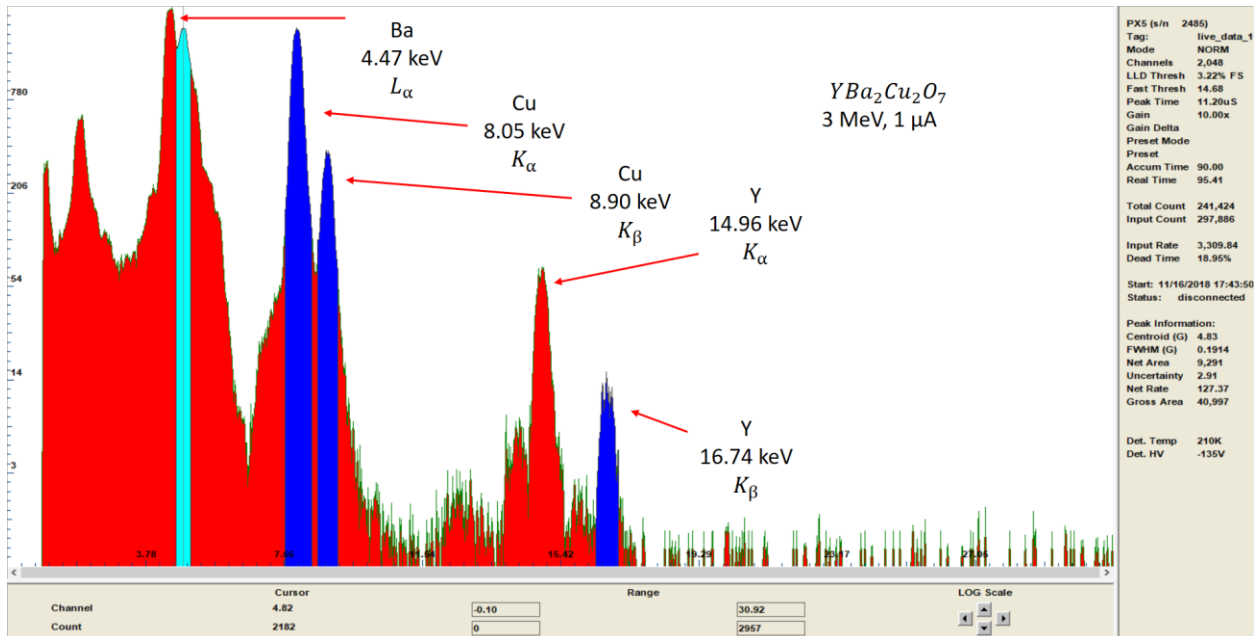
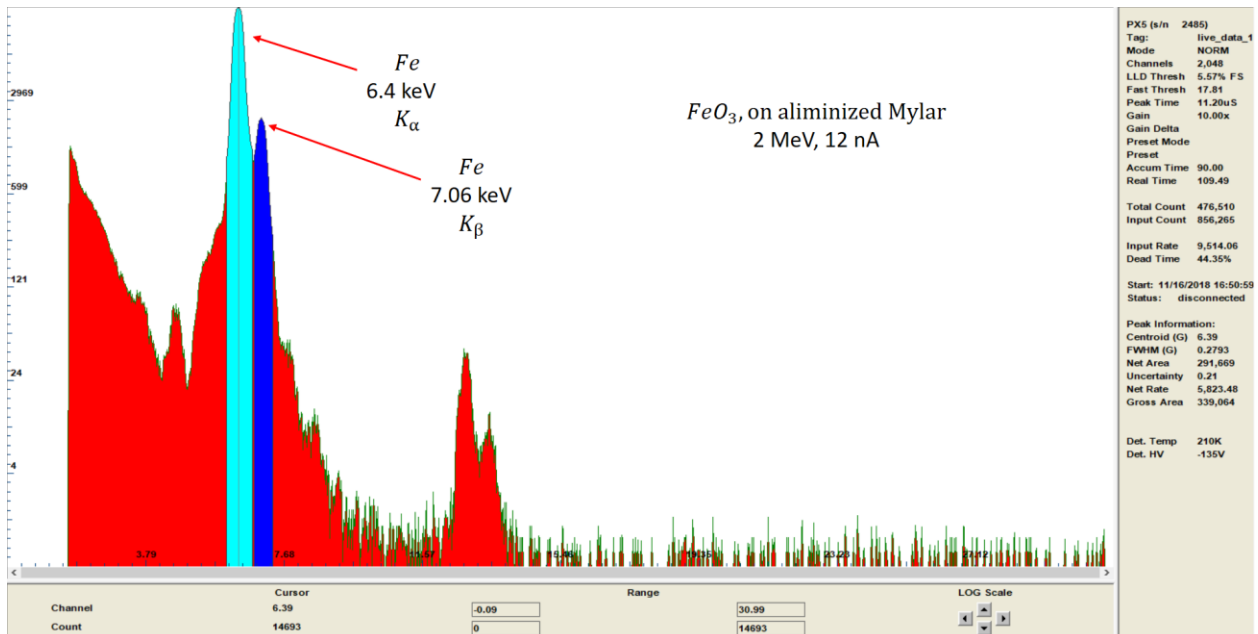
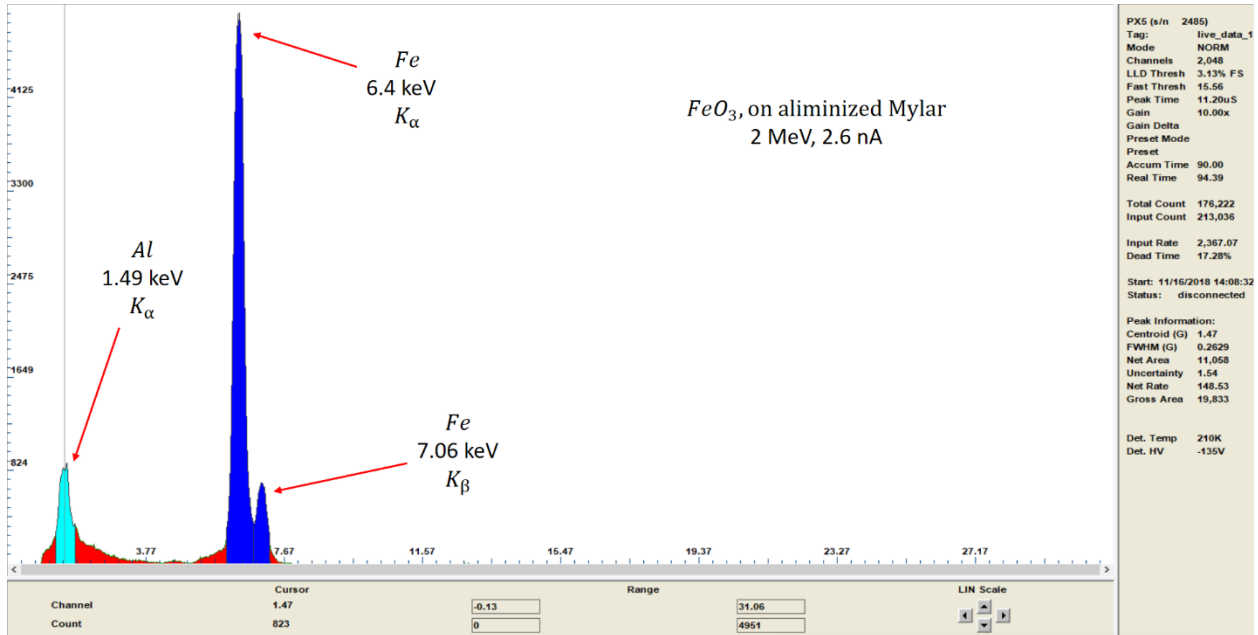


Figure (47) superconductor x-ray spectra at 3 MeV with a current of 1 nA



Figures (48) and (49) By comparing the iron oxide data, it is clear that dead time is directly related to beam current, but with the XR-100 Fast SDD detector the results are still acceptable at maximum of 50% dead time.



4. Conclusion

East Carolina University's Particle Induced X-ray Emission system was redesigned to gather and analyze x-ray spectra generated by the proton irradiation of multielement targets. The x-ray fluorescence spectroscopy system uses a state-of-the-art Amptek XR-100 Fast Silicon Drift Diode detector in conjunction with a digital pulse processor and multi-channel analyzing software. The target analysis chamber can be evacuated below 10^{-6} Torr within a day's time, and it houses a remotely automated 24 position sample changer that can be operated while under vacuum.

ECU's PIXE system was operations checked, calibrated, tested, and operationally verified using known spectral data and reconciling them with known x-ray sources or targets. After this work the PIXE system is to be augmented with GUPIX spectral analysis software.